

FOURIER TRANSFORM INFRARED STUDIES OF GUEST-HOST
INTERACTIONS IN ICE

by

George Kumi

A Dissertation Presented to the
FACULTY OF THE GRADUATE SCHOOL
UNIVERSITY OF SOUTHERN CALIFORNIA
In Partial Fulfillment of the
Requirements for the Degree
DOCTOR OF PHILOSOPHY
(CHEMISTRY)

August 2007

Copyright 2007

George Kumi

Dedication

To the Gardiner and Kumi clans

Acknowledgements

The doctoral degree is inherently an individual honor, and yet it is oftentimes a culmination of efforts and commitments by many to one person. It has taken a village to guide, support, and inspire me in my academic endeavors, and in life. It is a village of people too numerous to name, and no measure of thanks is commensurate with the gratitude I will always feel for their help. That said, it is nothing short of an honor to single out a few who have been instrumental in helping me at USC.

I am grateful to my advisors, Hanna Reisler and Curt Wittig. It has been a pleasure to interact with such insightful and ebullient mentors, and I will continue to seek their counsel for as long as they will permit it. In particular, I am indebted to them for taking a chance on me when all I had to offer was enthusiasm and a promise to work diligently.

A postdoc, Wousik Kim, and a senior graduate student, Minda Suchan, welcomed me to the project and made me feel useful. Indeed, for a while I was Minda's shadow, learning from someone who embraced readily the responsibilities of teaching a novice. Samantha Hawkins (a.k.a. Karate Sam) and Sergey Malyk were delightful partners who ensured laboratory discussions were always engaging and not always about science. I consider myself fortunate to have met all these individuals. I would like to express my thanks to Oscar Rebolledo-Mayoral who joined the project just as I was leaving it and willingly helped to prepare this

dissertation. I am grateful also to Sun Lee, my first office mate and now 'adopted' sister, who tolerated my various eccentricities with a smile and contentiously tried to ensure that I did not skip lunch.

My time at the Seaver Science Center was spent in an atmosphere that engendered friendships and collaborations among the numerous chemistry groups situated at this center. Thus, I must extend my sincere thanks to Professors Bradforth, Koel, Krylov, Mak, Reisler, Villesov and Wittig for fostering this environment. I have enjoyed getting to know many of the individuals who were members of their groups during my graduate studies, and I appreciate the support and assistance these individuals provided. Thanks also to all the support staff at the Chemistry department, especially to Valerie Childress, Michele Dea, Robert Martin, Heather Meunier-Connor, Jennifer Torres and Yuki Yabuta.

Last, but not least, I thank my family for their unwavering encouragement and support during this venture; I am privileged to have had such support throughout all my undertakings.

Table of Contents

Dedication	ii
Acknowledgements	iii
List of Figures	vii
Abstract	xiii
Chapter 1: Introduction	1
1.1 Wading Through Water	1
1.2 The Low Temperature Ice Phases: ASW, CI and HI	3
1.3 Icy Mixtures	10
1.4 Thesis Overview	16
1.5 Chapter 1 References	18
Chapter 2: Fourier Transform Infrared Spectroscopy and Temperature Programmed Desorption	23
2.1 Absorption Spectroscopy	23
2.2 Fourier Transform Infrared Spectroscopy	26
2.3 The Michelson Interferometer	27
2.4 The Fourier Transform	32
2.5 Practical Aspects of FTIR Spectroscopy	33
2.6 Temperature Programmed Desorption	42
2.7 Chapter 2 References	46
Chapter 3: Experimental Apparatus	48
3.1 Introduction	48
3.2 The UHV System	48
3.3 The Top Tier: the FTIR Chamber	51
3.4 FTIR Optics and Set-up	52
3.5 The Surface Manipulator	56
3.6 The Substrate	57
3.7 The Sample Holder	59
3.8 The Sample Holder: the Second Design	62
3.9 Sample Preparation	65
3.10 Chapter 3 References	67

Chapter 4: Transport and Guest-Host Interactions in Ice	68
4.1 Introduction	68
4.2 Experimental Details	71
4.3 Results: Interactions of CO ₂ with ASW	74
4.4 Results: N ₂ O Interactions with ASW	82
4.5 Discussion	90
4.6 Summary	98
4.7 Chapter 4 References	101
Chapter 5: The Nature of Trapping Sites in Ice	103
5.1 Introduction	103
5.2 Experimental	106
5.3 Results	107
5.4 Discussion	111
5.5 Epilogue	113
5.6 Chapter 5 References	115
Chapter 6: Future Experiments	117
6.1 Amorphous Materials	117
6.2 ASW: Transport and the Amorphous-Crystalline Interface	118
6.3 Experimental Strategy	122
6.4 Experimental Details: the Current Configuration	127
6.5 Experimental Details: the Modifications	129
6.6 Summary	131
6.7 Chapter 6 References	133
Bibliography	135

List of Figures

- Figure 2.1** Radiation (shown in blue) from a broadband IR source is split by a beamsplitter (red) and directed toward two mirrors. The radiation reflected from these mirrors recombines at the beam splitter. The radiation reflected back to the source during this recombination has been omitted for clarity. The moving mirror is used to change the path difference between the two beams. 27
- Figure 2.2** The intensity at the detector oscillates as a result of interference. This is shown in plots of $1 + \cos(2\pi\bar{\nu}\Delta x)$ versus phase difference for plane waves of light with (a) one wavelength, 2000 cm^{-1} , (b) two wavelengths, 2000 and 2200 cm^{-1} , with the same irradiance, and (c) two wavelengths, 2000 and 2200 cm^{-1} , of different irradiance (the 2000 cm^{-1} wave has 0.6 the irradiance of the 2200 cm^{-1} wave). 30
- Figure 2.3** The Fourier transform of a boxcar function (shown in (a)) is the sinc function (shown in (b)), and this function has several side lobes adjacent to its main feature. (c) The spectrum of a monochromatic line takes on a *sinc*(*x*) lineshape as a result of the inability to measure the interference signal over $-\infty \leq \Delta x \leq \infty$. The width of the feature obtained is shown. 35
- Figure 2.4** A triangular apodization function (shown in (a)) Fourier transforms to yield a *sinc*² function (shown in (b)), which has side lobes that are small compared to the main feature. Although there is significant overlap when two *sinc*² functions are separated by the distance shown in (c), these two functions (blue) are still distinguishable in the combined trace (red). At this separation, two *sinc* functions would display no overlap in their main feature. 37
- Figure 3.1** A schematic of the UHV Chamber. The numerous ports on tiers 1 and 2 have been omitted for clarity. The entire UHV system is evacuated by a turbomolecular pump located on the second tier. 50
- Figure 3.2** A schematic of the FTIR chamber. The axis system shown relates the orientation of this view to the view depicted in Figure 1. 52

Figure 3.3	A schematic showing the IR beam path from the source to the detector. All pertinent components outside the UHV chamber and the spectrometer are placed in purge boxes (shown in green).	53
Figure 3.4	The peak-to-peak absorbance routinely obtained in the $\sim 2700\text{ cm}^{-1}$ region with the experimental configuration described in this chapter.	56
Figure 3.5	The surface manipulator that is attached to the UHV system. The stainless steel tube of the manipulator and the copper piece attached to this tube are shown explicitly in the inset.	58
Figure 3.6	A drawing of the surface holder used to attach the surface to the manipulator. The two main copper parts of the holder are labeled A and B. One of the two copper plates that are used to sandwich the surface is shown.	60
Figure 3.7	A drawing of sample holder 2; the copper foil is attached to the two main parts of the holder (A and B) using a screw (inserted into the tapped hole labeled C).	63
Figure 3.8	The homemade heater is a wire coil with alumina sleeves. The sleeves insulate the wire and ensure current travels throughout the entire length of the wire.	65
Figure 4.1	(a) Varying amounts of CO_2 deposited at 90 K onto ASW films of approximately constant thickness (~ 65 layers). CO_2 exposure times (in minutes) at constant pressure (4×10^{-8} Torr) were: (i) 1.5 (ii) 3 (iii) 6. The broad water feature at $\sim 3250\text{ cm}^{-1}$ provides estimates of relative film thickness. The horizontal scale is expanded to emphasize (b) the CO_2 and (c) $^{13}\text{CO}_2\text{ } \nu_3$ region.	75
Figure 4.2	The same amount of CO_2 was deposited at 90 K onto ASW films of varying thickness. The films were exposed to 4×10^{-8} Torr CO_2 for 3 min. H_2O exposure times at 5×10^{-8} Torr were: (i) 2 (ii) 4 (iii) 8 and (iv) 16 min, corresponding to 10, 20, 40 and 80 layers, respectively. Entries (a) and (b) show spectral regions for CO_2 and H_2O , respectively.	76

- Figure 4.3** Spectra of the CO₂ that remained after depositing at 90 K equal amounts of CO₂ (3 min at 4×10^{-8} Torr) onto ASW films of varying thickness followed by raising the temperature. The temperature was raised to 105 K where it was held for 15-20 minutes before each trace was obtained. Entries (i) – (iii) correspond to ASW films of thickness 20, 40, and 80 layers, respectively. Panels (a) and (b) show the same traces on different horizontal scales. 78
- Figure 4.4** Spectra of the CO₂ that remained after depositing different amounts of CO₂ onto ASW films of constant thickness (~65 layers) and then increasing the temperature to 105 K. The spectra were recorded at 105 K, 15-20 min after the reaching this temperature. The CO₂ exposure times at 4×10^{-8} Torr were (i) 1.5 (ii) 3 and (iii) 6 min. See Figure 4.1 for the spectra recorded following CO₂ deposition at 90 K. 79
- Figure 4.5** CO₂ (4×10^{-8} Torr, 4 min) was deposited onto a 90 K ASW film of 40 layers. The temperature was then raised to 105 K for 15 min, at which time a spectrum was recorded. The figure depicts the evolution of the 105 K spectra as the temperature was increased in steps to the temperatures shown and held at these temperatures for the duration of a scan (~8 min). The spectra were recorded immediately after each temperature increase and at the temperatures indicated. Entries (a) and (b) show the spectral region for CO₂ and H₂O, respectively. The broad H₂O feature (~3250 cm⁻¹) changes upon annealing past 165 K because of the ASW-to-cubic phase transition. 80
- Figure 4.6** Different amounts of CO₂ on an ASW film (~1000 layers). The amount of CO₂ was varied via the sequence: (i) no deposition (ii) 4×10^{-8} Torr for 2 min and (iii) 1×10^{-7} Torr for 16 min. Spectra shown were recorded immediately after each deposition. The inset shows the *d*-OH feature is red shifted as a consequence of CO₂ deposition; namely the feature at ~3700 cm⁻¹ moves to ~3650 cm⁻¹. 82
- Figure 4.7** (a) Varying amounts of N₂O were deposited onto 90 K ASW films. The broad H₂O feature (~3250 cm⁻¹) provides an estimate of relative film thickness, which were approximately equal to 70 layers. The N₂O exposure times at 4×10^{-8} Torr were: (i) 2 (ii) 4 and (iii) 8 min. (b) The horizontal scale is expanded to emphasize the N₂O ν_3 region. 83

- Figure 4.8** (a) ASW films of different thicknesses were prepared at 90 K by vapor depositing H₂O at 4×10^{-8} Torr. (a) H₂O spectra (i)–(iv) were recorded with deposition times of (i) 4, (ii) 8, and (iii) 16 min, corresponding roughly to 15, 35, and 70 layers. (b) Each film was exposed to 4×10^{-8} Torr N₂O for 4 min, and the corresponding N₂O spectra are labelled (i)–(iv). 84
- Figure 4.9** ASW films at 90 K were exposed to 4×10^{-8} Torr N₂O for 4 min. The temperature was then raised to 105 K and held there for 15–20 min before a spectrum was recorded. Approximate ASW thicknesses for (i)–(iv) were 15, 35, 70, and 150 layers, respectively. Entries (a) and (b) show H₂O and N₂O features, respectively. 85
- Figure 4.10** Spectra of the N₂O that remained after depositing different amounts of N₂O onto ASW films of same thickness (70 layers) and then increasing the temperature to 105 K. The temperature was then raised to 105 K and held there for 15–20 min before a spectrum was recorded. N₂O exposure times at 4×10^{-8} Torr for (i)–(iii) were 2, 4, and 8 min, respectively. 86
- Figure 4.11** N₂O (4×10^{-8} Torr for 4 min) was deposited onto a 90 K ASW film of 40 layers. The temperature was then raised to 105 K for 15 min, at which time a spectrum was recorded. The figure depicts the evolution of the 105 K spectra as the temperature was increased in steps to the temperatures shown and held at these temperatures for the duration of a scan (~8 min). The spectra were recorded immediately after each temperature increase and at the temperatures indicated. Three scans (~5 min in duration) were recorded at 165 K; the time interval between reaching 165 K and commencing each of these scans is specified for three relevant spectra. 87
- Figure 4.12** Spectra were recorded after sandwiching N₂O between two ASW films at 90 K, then raising the temperature to 105 K, and keeping it there for 15 min. The amount of deposited N₂O and the total number of water layers (~80) is the same for all spectra. The ratios of bottom layer to top layer thickness are: (i) 80:0, (ii) 60:20, (iii) 40:40, and (iv) 20:60. 88

- Figure 4.13** Spectra were recorded for different amounts of N₂O deposited onto an ASW film of ~1000 layers at 90 K. The amount of N₂O was increased via the sequence: (i) no deposition, (ii) 4×10^{-8} Torr for 4 min, (iii) 1×10^{-7} Torr for 3 min, and (iv) 2×10^{-7} Torr for 7 min. Spectra were recorded immediately following each deposition. The inset shows the *d*-OH feature is red shifted as a consequence of N₂O deposition. 89
- Figure 4.14** 90 K ASW films of approximately the same thickness were exposed to 4×10^{-8} Torr of CO₂ for the same duration (3 min). After CO₂ deposition, the temperature was increased to 105 K and held there while a spectrum was recorded. Traces are the spectra recorded for: (i) a film that was not annealed prior to CO₂ exposure and (ii) a film that was annealed for 15–20 min at 120 K and then re-cooled to 90 K prior to CO₂ exposure. The inset shows these spectra on an expanded horizontal scale with the corresponding absorbance magnification. 97
- Figure 5.1** A TPD trace of a CO₂ film prepared at 90 K on MgO(100). The TPD experiment was performed by heating the surface at ~1 K/s and monitoring a mass-to-charge ratio (*m/e*) of 44. MgO exposure to CO₂ was carried out at a pressure 4×10^{-8} Torr for 3 min. 107
- Figure 5.2** CO₂ was deposited (4×10^{-8} Torr for 3 min) onto an ASW film (5×10^{-8} Torr for 7 min) ~80 layers thick. The H₂O desorption was monitored by measuring *m/e* 18. Panels (a) and (b) show the TPD traces of CO₂ and H₂O respectively. The TPD trace of H₂O was scaled for clarity. 109
- Figure 5.3** TPD traces of CO₂ (4×10^{-8} Torr for 3 min) deposited onto ASW films (~80 layers). The temperature to which each sample was annealed prior to recording FTIR spectrum is indicated. As the traces show, the CO₂ TPD feature at 185 K was not affected by the annealing to 105 K. 110
- Figure 5.4** Spectra (*p*-polarized) of ASW films (~80 layers) exposed to CO₂ (4×10^{-8} Torr for 3 min). Each sample was annealed to the temperature indicated and then re-cooled to 90 K. The broad H₂O feature (~3250 cm⁻¹) changes upon annealing past 165 K because of the ASW-to-cubic phase transition. The inset shows the expanded scale of the CO₂ *v*₃ band absorbance region with the corresponding magnification factor. 110

- Figure 6.1** An ASW film with domains of crystalline ice (shown in red) may possess cracks or voids (shown in blue) at the amorphous-crystalline interface. 119
- Figure 6.2** The slabs (shown in blue) represent isolated regions of ASW on a supporting substrate. As these isolated regions approach the phase transition temperature, there may be a significant increase in lateral mobility (indicated by the black arrows) and material may be transported to the surrounding regions. 121
- Figure 6.3** (a) An ASW film is formed on a supporting substrate. (b) A mesh (shown in black) is placed in front of the film, and the film is irradiated. (c) All the ASW in the exposed areas desorb, leaving the structure depicted in blue. To form isolated rows of ASW with the axes of the rows parallel to the y-axis shown, the mesh can be translated in small increments along the x-axis. At each increment the substrate is irradiated to desorb any exposed ASW. To form isolated areas of ASW (the black squares), this process has to be done along both axes of the mesh (shown as x and y). 123

Abstract

Guest-host interactions in amorphous solid water (ASW) films doped with CO₂ or N₂O were examined experimentally. Investigations focused on exploring molecular transport and morphology in ASW. The main diagnostics were Fourier transform infrared (FTIR) spectroscopy and temperature programmed desorption (TPD).

ASW films were prepared at 90 K. Dopants exposed to these films saturate all the favorable sites within the film interior. The subsequent accumulation of dopants occurs atop the ASW films, and results in a polycrystalline film. Infrared signatures permit a distinction for these two cases; vibrational modes of the crystalline overlayer, and an easily discernible peak for dopants residing within the ASW film.

Desorption experiments show ASW traps some of the dopants residing within its bulk. As anticipated, some of these trapped species are released during the ASW-to-cubic ice transition at ~160 K. Annealing the 90 K ASW films to 120 K prior to dopant exposure lowers the film's capacity to include dopants within its bulk. No substantial differences were observed for CO₂ and N₂O. ASW dangling OH bonds displayed a red shift of roughly 50 cm⁻¹ upon interaction with these dopants.

Sandwich structures were prepared at 90 K, *i.e.*, ASW-dopant-ASW. At 105 K, some of the dopant molecules sandwiched in between the ASW escape by diffusion through the top ASW layer, and the remaining molecules appear to be distributed within the ASW film interior.

The factors mediating the ratio of dopants released during the phase transition to dopants that co-desorb with crystalline (cubic) ice were studied. The infrared signatures for these two sets of molecules suggest their local environments are similar. Future experiments using small molecules to explore molecular transport at complex interfaces are outlined.

Chapter 1: Introduction

1.1 Wading Through Water

In all of science, there is arguably no substance that has been investigated more times than water. On one hand, these efforts are indicative of a complex system that has been difficult to characterize using the available experimental and theoretical tools. On the other hand, these endeavors reflect the privileged status held by this critical life component. In spite of the progress that has been made in understanding the properties of water, there is plenty that remains unresolved.

Why has water been so difficult to characterize? Water is the richest one-component system known, with numerous phases each possessing distinct properties [1]. The predominant intramolecular interaction in pure water is hydrogen bonding [1, 2] and this is a challenging type of interaction to model in any system. Furthermore, because of its superior solvating capabilities, ensuring low levels of impurities in water is easier said than done. These impurities can lead to erroneous conclusions about experimental results. The example of "polywater" comes readily to mind; several years of research were required to conclude that this was not another phase of liquid water but simply liquid water containing small quantities of various impurities [3].

Everyday processes involving water are often rather complex. For example, it is well-known that water freezes to ice upon cooling, and yet there are very few molecular dynamics simulations illuminating the details of this phenomenon [4]. In

fact, the inordinate number of water studies clouds the reality that there is no "universally consistent fundamental description of water systems" [5]. The drive for a molecular level understanding of the properties and role of water in its condensed phase continues to fuel studies in a broad range of scientific fields. Atmospheric chemistry, molecular biology, and interstellar science are all areas where attaining this state of knowledge is critical to advances in basic and applied research.

Solid water, or ice as it is commonly known, has garnered special attention as an important surface for heterogeneous reactions [6-9]. The availability of water molecules for reaction and product stabilization appears to be a key factor mediating some heterogeneous processes [10]. Novel insights into important stratospheric chemical processes have been gleaned by focusing on the interaction of small (less than 5 atoms) molecules with ice films. In particular, studies of atmospherically important chlorine reservoir species, such as HCl and chlorine nitrate (ClONO₂), have shown that ice can influence the ozone cycle [6, 8]. The photochemistry of molecules constrained in or on ice is also becoming an area of fertile research, especially since work demonstrating that glycine, adenine, and serine form naturally after the ultraviolet (UV) photolysis of certain ice mixtures [11].

Among vitreous solids, the amorphous form of ice appears to be a substance of extraordinary character. Its low frequency collective vibrations, or phonons, exhibit characteristics similar to that of phonons in a crystalline material [12] rather than the behavior often observed in glassy materials. These results have been interpreted to mean that amorphous water can exist as disordered state with an unusually low

degree of local disorder. There is also speculation that amorphous water may provide the first clear evidence of "polyamorphism", the coexistence of two equilibrated amorphous phases [13, 14]. In addition, there are indications that this ice phase may serve as a model system for liquid water [15, 16] and other amorphous solid systems in general.

Performing experiments in ultrahigh vacuum (UHV) minimizes the concentration of unwanted species, and this reduces or eliminates many of the complexities associated with competing processes. In particular, this type of environment is crucial to simplifying the characterization of solid water. Only three ice phases can be cooled enough to exhibit a vapor pressure of less than 10^{-10} Torr: amorphous solid water (ASW), cubic ice (CI) and hexagonal ice (HI) [1]. These ice forms are the only thermodynamically stable phases in UHV, *i.e.*, the only phases capable of existing at these low pressures ($< 10^{-9}$ Torr). However, HI is difficult to prepare using the convenient method of vapor deposition, and thus experimental studies in these simplified environments generally focus on ASW and CI.

1.2 The Low Temperature Ice Phases: ASW, CI and HI

In general, ASW may be defined as a "solid phase of water that is metastable with respect to its crystalline phase" [17]. Here, the word metastable is meant to convey that ASW is never the most thermodynamically stable phase under any conditions. The existence of ASW stems solely from a kinetic favoring of its formation, over a more stable solid water form, in certain circumstances.

Nevertheless, ASW is the most prevalent ice phase in the universe [18]. It is found mainly in the interstellar medium, where it is usually combined with other condensed gases. In this environment, it is subject to UV radiation, ion winds, and cosmic rays, all of which may induce a host of effects; namely, chemical reactions, desorption, and lattice changes [19]. Needless to say, ASW is the solid water phase most relevant to the astrophysical community, and it has been the subject of many reviews [13, 14, 20].

The definition of ASW proffered above belies the vigorous debate concerning the very nature of ASW. The first report on ASW dates back to 1935; X-ray diffraction studies by Burton and Oliver [21] observed a diffuse pattern for water vapor deposited onto a copper rod at temperatures less than ~ 150 K. Since then, some groups have argued that different forms, or polymorphs, of amorphous ice (AI) exist. "Amorphousness" is difficult to quantify, and thus these groups have resorted to using certain properties, such as density, to distinguish between these AI polymorphs. Based on X-ray diffraction studies, Narten and coworkers [22] reported a "high density" (1.07 g/cm^3) amorphous phase prepared by vapor deposition at 10 K. This "high density" phase irreversibly changed to a "low density" (0.94 g/cm^3) AI over the range of 30-80 K. The compression of HI reportedly produces an AI with a density of 1.31 g/cm^3 , and this ice remains amorphous even after compression [23], slowly transforming into an ice form with a density of 1.17 g/cm^3 . Whether ASW does indeed have several polymorphs or if these varying densities stem from some other phenomenon is still an open question.

One of the important properties of ASW is its porosity, especially since this creates a relatively large available surface area for heterogeneous processes. ASW diffraction studies, which focus on short-range atomic oxygen distributions, provide no details about pore volumes. Therefore, the densities derived from these studies do not account for pore volumes in the ratio of mass to volume, and they are sometimes referred to as intrinsic densities [19]. In fact, due to its high porosity (relative to "low density" AI), the *bulk density* of "high density" AI is expected to be less than the *bulk density* of "low density" AI. Here, the term *bulk density* implies a density that takes into account phase porosity.

The porosity of ASW has been inferred from gas adsorption experiments at low temperatures (less than 30 K) [24, 25] and from other isothermal gas adsorption experiments [16, 26-28]; the large adsorption areas determined were not reconcilable with a non-porous substance. It is worth noting that gas adsorption studies provide information on the pores connected to the vacuum but say little or nothing about the enclosed pores. Measurements of the refractive index of ice, related to porosity by the Lorentz-Lorenz relation, can also be used to estimate ASW porosity [29]. However, there has been little progress on determining typical ASW pore dimensions, let alone pore distributions. Even the nature of the ASW surface remains unresolved [30, 31].

Why is ASW porous? It has long been speculated that at low substrate temperatures vapor deposited molecules quickly dissipate energy upon incidence, and therefore tend to remain close to the point of landing [1]. Such simple "hit and

stick" models have been used to depict how the porosity of a film depends on the incident angle of the incoming particles [25, 32]. These simulations are consistent with experiments probing the dependence of ASW morphology on the H₂O molecular beam incidence angle. Nevertheless, while there are postulates on how the energy dissipation probably occurs for ASW [19], there does not appear to be any experimental evidence directly supporting any of these rationalizations.

ASW films, vapor deposited at low temperatures, have displayed irreversible changes in properties upon annealing to temperatures well below (~ 30 K) any appreciable phase change [32-34]. Many groups have observed ASW spectral changes induced by annealing ASW deposited at low temperatures [33, 35, 36]. Hallbucker and coworkers [37] reported a heat release, presumably due to relaxation, during the heating of ASW. This heat release was accompanied by changes in the X-ray diffraction pattern. In addition, gas phase adsorption experiments [32, 33] suggest a decrease in ASW porosity occurs even when ASW films are annealed to temperatures not conducive to crystallization. Mainly because of compelling gas phase adsorption experiments [32], these irreversible changes have been interpreted as signaling slight molecular rearrangements in ASW that result in permanent pore closures. It is worthwhile noting that in light of this information, the general assumption that ASW by definition is porous may not always apply. Further investigations are required for a more complete picture.

There are a variety of methods used to form ASW: vapor deposition onto a cold substrate [21, 34], the rapid cooling of liquid water [16, 38, 39] and the high pressure

"amorphization" of crystalline ice [40-42]. Vapor deposition is by far the easiest technique for UHV studies, and thus it is almost always the method of choice in such endeavors. Kimmel and coworkers [32] found that the porosity of ASW films, examined via gas adsorption experiments, were dependent upon the incident angle of the collimated H₂O molecular beam used to form the film. Many agree that this work demonstrates the sensitivity of ASW characteristics to growth conditions. This dependence suggests that the conflicting results concerning the physical properties of ASW may stem from different growth conditions. Indeed, there are speculations that perhaps a continuum of AI structures can be formed, each with varying bulk physical properties dependent upon growth conditions [19].

In short, the current understanding of basic ASW properties is fragmentary. In part, this is because ASW does not display the properties of a single, well-defined phase, and consequently it has been a challenging ice form to characterize. There is a need for further experimental investigations that shed light on the size range of pores, the mechanisms responsible for the irreversible structural changes upon annealing, and the structure of the ASW surface. From a theoretical standpoint, a detailed understanding of the processes (*e.g.*, hydrogen bonding) that combine to yield the characteristic ASW infrared spectrum remains an outstanding problem. More importantly, it is apparent that to perform meaningful comparisons between various ASW studies, growth conditions must be specified precisely.

Like ASW, cubic ice is also a metastable ice phase. First reports about its existence originate from electron diffraction studies by König in 1942 [1]. In these

studies, the diffuse diffraction pattern of ASW changed upon annealing into a pattern consisting of sharp rings that suggested a cubic crystalline ice structure (similar to that in diamond). The metastable nature of CI was deduced from the irreversible transformation of CI to HI at temperatures greater than ~ 200 K [1]. Moreover, CI produced when ASW is annealed does not revert to ASW upon cooling, and this shows that CI is a more thermodynamically favored form of ice than AI. This phase transition from ASW to CI has been the subject of much scrutiny, and it purportedly occurs over the range of ~ 135 - 165 K [13, 33, 34, 43].

Unlike ASW, cubic ice displays the properties of a well-defined phase, and thus many of its basic attributes are known. As mentioned above, its structure has been precisely determined from diffractions studies, and density measurements [1, 2] all generally show a density of ~ 0.94 g/cm³. Compared to ASW, CI exhibits very little ability to trap gases, and this suggests that it is non-porous. CI is routinely prepared in UHV by annealing ASW [34, 44] or vapor depositing H₂O onto a substrate with a temperature of 135 - 155 K [45, 46]. However, there are other documented methods of producing CI in other environments, *i.e.*, not low pressures [47]. The phase transition from ASW to CI is accompanied by spectral changes, and these changes provide a convenient indication of this process. Unfortunately, there are a limited amount of techniques that can be used to confirm a total transformation. It is thus worth bearing in mind that experiments with CI are susceptible to the question of phase purity and the possibility of ASW domains within CI.

The solid water form obtained when liquid water is frozen at atmospheric pressures is HI. Consequently, it is the ice form commonly referred to as "ice". Like CI, it is crystalline and displays well-defined characteristics [1]. Several diffraction studies have confirmed its structure, although the exact position of the hydrogen atoms was temporarily a point of contention [1].

Forming HI via vapor deposition requires substrate temperatures ~ 200 K and higher. At these temperatures, the H_2O desorption flux is high ($> 10^{-5}$ Torr) [48], thus and ambient pressures greater than 10^{-5} Torr are needed to form a film [49]. These pressures increase the likelihood of trapping unwanted species within the film during sample preparation. More importantly, it is difficult to pump out systems quickly (within ~ 15 minutes) after such exposures. Thus, for mostly experimental reasons associated with its preparation, HI is rarely studied in a simplified UHV environment. This is unfortunate because there are important processes that involve this particular ice form. For example, polar stratospheric clouds, which play a major role in the ozone cycle, have HI as a major constituent [29, 50, 51]. Nevertheless, because of the similarities in the physical structure of CI and HI, many experiments performed in low pressure environments utilize CI as a model for HI [29, 50, 52].

The current state of knowledge on low temperature ice, and also of water in general, has been acquired over several decades by accruing an expansive body of theory and experiments. It is prudent, if not logical, to assume that the lingering questions will be resolved also by the meticulous accumulation of a large set of new results. In a general sense, the work described in this dissertation is a contribution to

the body of experimental data necessary for formulating a fundamental description of solid water. More specifically, it is an examination of the guest-host interactions within ice (ASW and CI to be exact) designed to yield basic knowledge about structure and molecular transport in ice. To set the results of this work in context, it is constructive to review briefly some of the previous studies detailing the interaction between various molecules and ice.

1.3 Icy Mixtures

The localization of an atom or molecule on the surface of a solid is termed adsorption. This terminology is relatively unambiguous when it applies to a nonporous solid that permits negligible diffusion into the bulk lattice by any atomic or molecular species residing on the solid surface. Some solids can be prepared in a manner that imbues them with an intrinsic porosity, *e.g.*, zeolites. In this case, an atom or molecule located on the surface of a pore can also be described as being adsorbed. Several reports detailing ice-related experiments use the term adsorption to describe accumulation in, or on, ice pores and on the outer molecular layer of an ice film or cluster [27, 44, 53, 54]. It is this relatively loose definition that will be used in this discussion. However, it is relevant to note that there is often little evidence in these studies that allows a distinction between a molecule located on the surface of a pore and within the bulk lattice.

There is a tendency to categorize interactions between ice and various species in terms of interaction strength; these energies are derived from vibrational shifts of ice

bands that are observed as ice interacts with different molecules [53, 55]. The spectra of ice in the OH stretching region is dominated by a broad ($\sim 300\text{ cm}^{-1}$) vibrational feature at $\sim 3250\text{ cm}^{-1}$, and, in some ice structures, a relatively weak feature at $\sim 3700\text{ cm}^{-1}$ is present as well [36, 55]. The latter feature is believed to originate from dangling OH (hereafter denoted by $d\text{-OH}$) groups that do not participate in the hydrogen bonding network present in ice, and thus this feature is observed only when these groups are present in appreciable concentrations. Several groups have reported no discernible change in the broad OH signal (at $\sim 3250\text{ cm}^{-1}$) during the interaction of various molecules with ice. However, the $d\text{-OH}$ signal has displayed vibrational shifts dependent upon the molecular species associating with the ice film, and these shifts range from a few to a hundred wavenumbers [55-57].

Compared to the typical interaction energies and their corresponding vibrational band shifts observed in rare gas matrices, the interaction energies derived from such shifts are small (less than 20 kJ/mol). Thus, there are some questions concerning the validity of the process used to obtain the interaction strength of molecules interacting with ice [33]. A less controversial method of characterizing these interactions is simply in terms of the magnitude of the $d\text{-OH}$ band shift. This approach sidesteps the debate concerning the correlation of $d\text{-OH}$ band shifts and interaction energies and still affords a convenient categorization scheme.

Generally, the shift experienced by the $d\text{-OH}$ band during the aforementioned interactions is always to lower frequencies, *i.e.*, a red shift. For example, the exposure of Ar, Kr, or CF_4 to a freshly prepared ASW film results in $d\text{-OH}$ band

shifts of roughly 12, 17, and 7 cm^{-1} , respectively [58]. On the other hand, acetylene, ethylene, and benzene each induce a shift of $\sim 100 \text{ cm}^{-1}$ in ice clusters [53]. In fact, the *d*-OH shift can become indiscernible when certain molecules are deposited onto ice; Schaff and Roberts [52] observed this phenomenon during the infrared studies of acetone on ice. In this case, the red shift occurs to such an extent that the weak *d*-OH band overlaps with the dominant OH band, and therefore this weak band becomes indistinguishable. These changes in the *d*-OH band position are attributed to "hydrogen-bond-like" associations between these various molecules and ice. This conclusion is based partly on the fact that the formation of hydrogen bonds in other systems also tends to induce red shifts.

Certain molecules not only adsorb onto ice but also appear to induce molecular rearrangements within the ice lattice. HCl, an atmospherically important species, is one such molecule and elucidating the fundamental mechanism of HCl adsorption has been especially challenging. Firstly, the nature of the adsorbed HCl was vigorously debated, with early arguments centered upon whether the adsorbate was molecular or ionic [50, 59-61]. Contrary to general intuition, there is experimental evidence suggesting HCl can ionize once adsorbed *molecularly* on ice [50, 62], and this implies a reorientation of neighboring water molecules to accommodate the process. In addition, some studies observe an eventual disruption of the ice lattice and the formation of stable ionic hydrates at appropriate HCl-water stoichiometries [10]. There now appears to be little doubt that the initial adsorption state for HCl serves as a precursor state from which subsequent interactions can occur.

Investigations of N_2O_5 and ClONO_2 on ice films have arrived at similar conclusions concerning the role of the initial adsorption state [19].

IR spectroscopy has been an invaluable tool in characterizing the nature of ice and its interactions with other species. However, thermal desorption studies [28, 63-67] have also been beneficial in providing novel insights into the sublimation characteristics of various ice systems. Two disparate fields have driven such studies: atmospheric chemistry and astrophysics. For astrophysics in particular, the realization that ice could trap and retain molecules to temperatures much higher than the sublimation temperatures exhibited by these molecules was an important one [28].

Early studies focused on establishing the sublimation traits of icy mixtures via thermal desorption experiments. One of the earliest reports on the trapping capabilities of ASW showed that the release of species trapped in ice occurred at distinct temperatures: O_2 trapped in ASW (prepared at 77 K) desorbed at roughly 95 K, 160 K and 214 K [28]. This behavior, in conjunction with similar observations for other trapped species in ASW [64, 68], implied that species could be present in interstellar ices at temperatures far beyond their sublimation temperatures. Sandford and Allamandola recorded the IR spectra of ice mixtures for different temperatures and "gas/ H_2O " ratios, and they found the release of trapped species did not transpire continuously as the ice temperature was increased [66, 67, 69]. An extension of these trapping studies was done by Hudson and Donn [63]. Monitoring gas release with a

mass spectrometer, they were able to correlate changes in the IR spectra of ice (*e.g.*, the ASW-to-crystalline ice transition) with the desorption of trapped species.

Recent studies have extended this work through the development of simplified models capable of quantitatively simulating experimental desorption data [70]. These desorption models have taken into account the fact that gas release in certain temperature regions is not indicative of the interaction strength between a molecular (or atomic) species and ice. Instead, these expulsions are related to changes induced in ice by thermal energy supplied during ice annealing, and consequently the desorption attributes of a species leaving an ice film is indeed mediated by the film. Several recent reports in this field have focused on the formation complex products produced by UV photolysis of interstellar ices [11]. These investigations utilize laboratory analogs of interstellar ice to explore the transformation in composition of interstellar ice induced by UV radiation, and they represent a new front in ice-related studies.

In general, the desorption of a molecular adlayer, consisting of multiple layers, from a surface results in two distinct desorption trace features (a detailed explanation of how desorption traces are obtained is provided in the ensuing chapter of this dissertation). One feature originates from molecules directly in contact with the underlying surface, *i.e.*, the monolayer, while the other is from molecules separated from the solid surface by one or more layers of molecules, *i.e.*, the multilayer. Because of a screening effect by the monolayer, the binding energy of molecules in the multilayer to the surface is less than the energy binding the monolayer to the

surface. Consequently, less energy is required to remove the multilayer, and it desorbs at lower temperatures than the monolayer.

The desorption characteristics of a species interacting with ice can be explained relatively simply if the species does not display the complex adsorption dynamics associated with molecules like HCl. In a thermal desorption study of several astrophysically relevant molecules, Collings and coworkers [71] found that less than four prominent desorption features were present in desorption traces of several species deposited onto thin ($< \sim 100$ layers thick) ASW films. In addition to the monolayer and multilayer desorption from the ice surface, they observed two features from molecules that get trapped within ASW. For some molecules, however, the monolayer and multilayer features appeared to overlap and were indistinguishable from one another. One of the features from the trapped molecules is associated with molecules that desorb during the ASW phase transition and the other is from molecules that desorb during the cubic ice film desorption. The release of trapped species during the aforementioned phase transition has been observed by several groups [24, 63, 69, 72, 73] and this release is sometimes referred to as a molecular volcano [24].

It is widely accepted that molecules trapped in ice can be released during the ASW-to-CI transition. What is unknown is the process that mediates the ratio of trapped species released during the phase transition to trapped species that are retained within CI. Several investigators have observed both features [24, 63, 71-73] during desorption studies, and yet the nature of site from which these molecules

desorb remains a source of speculation. Ayotte and coworkers [24] have suggested that it may originate from guest molecules trapped in a clathrate-hydrate cage. However, there are only a few species that appear to form clathrate-hydrates under low temperature and pressure conditions [74]. Collings and coworkers [71] observe that this co-desorption feature scales with ASW film thickness for "CO-ice" mixtures, suggesting that these molecules are distributed throughout the ice bulk (be it in pores or within the lattice). However, it is not clear if the amount of co-desorbing species, which is proportional to the intensity of the co-desorption feature, can be manipulated independent of ASW thickness, *e.g.*, by changing deposition conditions.

1.4 Thesis Overview

The nature of the interaction between CO₂ and N₂O molecules and ice is the subject of this dissertation, and it is work that was motivated primarily to understand the trapping, adsorption, and desorption processes in ice. The rationalizations supporting the choice of these molecules (CO₂, N₂O) is detailed in the ensuing chapters. For the first time, the *d*-OH red shift observed for the "CO₂-ice" and "N₂O-ice" systems is reported. Basically, this work

1. confirms the effectiveness of CO₂ and N₂O as probes of ice morphology
2. expounds upon the nature of the co-desorbing species in ice

3. sets the stage for future experiments, utilizing these probes, that will explore molecular transport at complex interfaces with ASW as a model for amorphous systems

The theoretical constructs behind the two diagnostic techniques used in this study are detailed in the following chapter, Chapter Two. In Chapter Three, a description of the experimental apparatus is provided. Chapter Four discusses the intermolecular interactions of two specific species (CO_2 or N_2O) with ice. Preliminary work focused on understanding the dynamics of ice crystallization is presented in Chapter Five. Finally, Chapter Six provides a summary of future work.

1.5 Chapter 1 References

- [1] P. V. Hobbs, *Ice Physics*, Claderon Press: Oxford, 1974.
- [2] F. Franks, In *Water: A comprehensive treatise*, F. Franks, Ed.; Plenum Press, New York, 1982, Vol. 7.
- [3] F. Franks, *Polywater*, MIT press: Cambridge, 1981.
- [4] M. Matsumoto, S. Saito and I. Ohmine, *Nature*, *416*, 409–413, (2002).
- [5] V. Buch and J. P. Devlin, In *Water in Confining Geometries*, V. Buch and J. P. Devlin, Eds.; Springer, Berlin, 2003.
- [6] Z. Y. Wang and S. K. Zhou, *Progress in Chemistry*, *16*, 49, (2004).
- [7] A. B. Horn, J. R. Sodeau, T. B. Roddis and N. A. Williams, *Journal of Physical Chemistry A*, *102*, 6107, (1998).
- [8] G. Faraudo and D. E. Weibel, *Progress in Reaction Kinetics and Mechanism*, *26*, 179, (2001).
- [9] L. Chu and L. T. Chu, *Journal of Physical Chemistry A*, *103*, 691, (1999).
- [10] S. Haq, J. Harnett and A. Hodgson, *Journal of Physical Chemistry B*, *106*, 3950, (2002).
- [11] M. P. Bernstein, J. P. Dworkin, S. A. Sandford, G. W. Cooper and L. J. Allamandola, *Nature*, *416*, 401, (2002).
- [12] H. Schober, M. M. Koza, A. Tolle, C. Masciovecchio, F. Sette and F. Fujara, *Physical Review Letters*, *85*, 4100, (2000).
- [13] C. A. Angell, *Annual Review of Physical Chemistry*, *34*, 593, (1983).
- [14] C. A. Angell, *Annual Review of Physical Chemistry*, *55*, 559, (2004).
- [15] C. A. Angell, *Science*, *267*, 1924, (1995).
- [16] E. Mayer and R. Pletzer, *Nature*, *319*, 298, (1986).
- [17] R. S. Smith, Z. Dohnalek, G. A. Kimmel, G. Teeter, P. Ayotte, J. L. Daschbach and B. D. Kay, In *Water in Confining Geometries*, V. Buch and J. P. Devlin, Eds.; Springer, Berlin, 2003.

- [18] T. L. Roush, *Journal of Geophysical Research-Planets*, 106, 33315, (2001).
- [19] R. A. Baragiola, In *Water in Confining Geometries*, V. Buch and J. P. Devlin, Eds.; Springer, Berlin, 2003.
- [20] M. G. Sceats and S. A. Rice, In *Water: A comprehensive treatise*, F. Franks, Ed.; Plenum Press, New York, 1982, Vol. 7.
- [21] E. F. Burton and W. F. Oliver, *Proceedings Royal Society*, A153, 166, (1935).
- [22] A. H. Narten, C. G. Venkatesh and S. A. Rice, *The Journal of Chemical Physics*, 64, 1106, (1976).
- [23] C. A. Tulk, C. J. Benmore, J. Urquidi, D. D. Klug, J. Neufeind, B. Tomberli and P. A. Egelstaff, *Science*, 297, 1320, (2002).
- [24] P. Ayotte, R. S. Smith, K. P. Stevenson, Z. Dohnalek, G. A. Kimmel and B. D. Kay, *Journal of Geophysical Research-Planets*, 106, 33387, (2001).
- [25] K. P. Stevenson, G. A. Kimmel, Z. Dohnalek, R. S. Smith and B. D. Kay, *Science*, 283, 1505, (1999).
- [26] B. Schmitt, J. Ocampo and J. Klinger, *Journal De Physique*, 48, 519, (1987).
- [27] R. Pletzer and E. Meyer, *Journal of Chemical Physics*, 90, 5207, (1989).
- [28] J. A. Ghormley, *Journal of Chemical Physics*, 46, 1321, (1967).
- [29] B. S. Berland, D. E. Brown, M. A. Tolbert and S. M. George, *Geophysical Research Letters*, 22, 3493, (1995).
- [30] D. Nordlund, H. Ogasawara, P. Wernet, M. Nyberg, M. Odelius, L. G. M. Pettersson and A. Nilsson, *Chemical Physics Letters*, 395, 161, (2004).
- [31] Y. Zubavichus, M. Zharnikov, Y. J. Yang, O. Fuchs, E. Umbach, C. Heske and M. Grunze, *Langmuir*, 22, 7241, (2006).
- [32] G. A. Kimmel, K. P. Stevenson, Z. Dohnalek, R. S. Smith and B. D. Kay, *Journal of Chemical Physics*, 114, 5284, (2001).
- [33] C. Manca, C. Martin and P. Roubin, *Chemical Physics*, 300, 53, (2004).

- [34] P. Jenniskens, S. F. Banham, D. F. Blake and M. R. S. McCoustra, *Journal of Chemical Physics*, *107*, 1232, (1997).
- [35] A. Givan, A. Loewenschuss and C. J. Nielson, *Journal of Physical Chemistry B*, *101*, 8696, (1997).
- [36] C. Manca, C. Martin and P. Roubin, *Chemical Physics Letters*, *364*, 220, (2002).
- [37] A. Hallbrucker, E. Mayer and G. P. Johari, *Journal of Physical Chemistry*, *93*, 4986, (1989).
- [38] G. P. Johari, A. Hallbrucker and E. Mayer, *Nature*, *330*, 552, (1987).
- [39] J. Dubochet and A. W. McDowell, *Journal of Microscopy-Oxford*, *124*, RP3, (1981).
- [40] Y. P. Handa, O. Mishima and E. Whalley, *Journal of Chemical Physics*, *84*, 2766, (1986).
- [41] O. Mishima, L. D. Calvert and E. Whalley, *Nature*, *310*, 393, (1984).
- [42] O. Mishima, L. D. Calvert and E. Whalley, *Nature*, *314*, 76, (1985).
- [43] D. Laufer, E. Kochavi and A. Barnun, *Physical Review B*, *36*, 9219, (1987).
- [44] J. E. Schaff and J. T. Roberts, *Journal of Physical Chemistry*, *98*, 6900, (1994).
- [45] P. U. Andersson, M. B. Nagard, G. Witt and J. B. C. Pettersson, *Journal of Physical Chemistry A*, *108*, 4627, (2004).
- [46] M. E. Palumbo, *Journal of Physical Chemistry A*, *101*, 4298, (1997).
- [47] J. E. Bertie, L. D. Calvert and E. Whalley, *Journal of Chemical Physics*, *38*, 840, (1963).
- [48] R. S. Smith and B. D. Kay, *Surface Review and Letters*, *4*, 781, (1997).
- [49] K. L. Foster, M. A. Tolbert and S. M. George, *Journal of Physical Chemistry A*, *101*, 4979, (1997).
- [50] J. D. Graham and J. T. Roberts, *Journal of Physical Chemistry*, *98*, 5974, (1994).

- [51] T. Huthwelker, M. Ammann and T. Peter, *Chemical Reviews*, *106*, 1375, (2006).
- [52] J. E. Schaff and J. T. Roberts, *Journal of Physical Chemistry*, *100*, 14151, (1996).
- [53] S. C. Silva and J. P. Devlin, *Journal of Physical Chemistry*, *98*, 10847, (1994).
- [54] T. Takoaka, M. Inamura, S. Yanagimachi, I. Kusunoki and T. Komeda, *Journal of Chemical Physics*, *121*, 4331, (2004).
- [55] B. Rowland, M. Fisher and J. P. Devlin, *Journal of Chemical Physics*, *95*, 1378, (1991).
- [56] J. Sadlej, B. Rowland, J. P. Devlin and V. Buch, *Journal of Chemical Physics*, *102*, 4804, (1995).
- [57] F. Borget, T. Chiavassa, A. Allouche and J. P. Aycard, *Journal of Physical Chemistry B*, *105*, 449, (2001).
- [58] C. Martin, C. Manca and P. Roubin, *Surface Science*, *502*, 275, (2002).
- [59] G. J. Kroes and D. C. Clary, *Journal of Physical Chemistry*, *96*, 7079, (1992).
- [60] Y. A. Mantz, F. M. Geiger, L. T. Molina, M. J. Molina and B. L. Trout, *Chemical Physics Letters*, *348*, 285, (2001).
- [61] M. Svanberg, J. B. C. Pettersson and K. Bolton, *Journal of Physical Chemistry A*, *104*, 5787, (2000).
- [62] N. Uras, M. Rahman and J. P. Devlin, *Journal of Physical Chemistry B*, *102*, 9375, (1998).
- [63] R. L. Hudson and B. Donn, *Icarus*, *94*, 326, (1991).
- [64] A. Barnun, G. Herman, D. Laufer and M. L. Rappaport, *Icarus*, *63*, 317, (1985).
- [65] A. Barnun, J. Dror, E. Kochavi, D. Laufer, D. Kovetz and T. Owen, *Origins of Life and Evolution of the Biosphere*, *16*, 220, (1986).
- [66] S. A. Sandford and L. J. Allamandola, *Icarus*, *76*, 201, (1988).

- [67] S. A. Sandford and L. J. Allamandola, *Astrophysical Journal*, 355, 357, (1990).
- [68] A. Barnun, J. Dror, E. Kochavi and D. Laufer, *Physical Review B*, 35, 2427, (1987).
- [69] L. J. Allamandola, S. A. Sandford and G. J. Valero, *Icarus*, 76, 225, (1988).
- [70] M. P. Collings, J. W. Dever, H. J. Fraser and M. R. S. McCoustra, *Astrophysics and Space Science*, 285, 633, (2003).
- [71] M. P. Collings, M. A. Anderson, R. Chen, J. W. Dever, S. Viti, D. A. Williams and M. R. S. McCoustra, *Monthly Notices of the Royal Astronomical Society*, 354, 1133, (2004).
- [72] J. D. Graham, J. T. Roberts, L. A. Brown and V. Vaida, *Journal of Physical Chemistry*, 100, 3115, (1996).
- [73] J. E. Schaff and J. T. Roberts, *Langmuir*, 14, 1478, (1998).
- [74] G. Natesco and A. Bar-Nun, *Icarus*, 148, 456, (2000).

Chapter 2: Fourier Transform Infrared Spectroscopy and Temperature

Programmed Desorption

2.1 Absorption Spectroscopy

Absorption spectroscopy, as its name suggests, is associated with the absorption of radiation by a sample. The absorption of radiation promotes the constituents of a sample (*i.e.*, atoms, ions or molecules) from one internal state to another, and is a process whereby radiant energy is transferred into the sample. The internal states of atoms, ions, or molecules are quantized, or consist of discrete energy levels. One of the stipulations for the efficient absorption of radiation is that the incident light be resonant with an energy level separation within the absorbing entity. Because these energy separations are unique for each absorbing entity, the constituents of a sample can be characterized by determining the frequencies of radiation absorbed by a sample.

Infrared (IR) absorption spectroscopy focuses on the absorption of IR radiation, and it is restricted to the study of neutral or ionic molecules. This restriction arises because only these species possess energy level separations that are resonant with IR radiation; these separations can be traced to inter-atomic vibrations present in a molecular species. Thus, IR absorption spectroscopy, which yields information about the vibrational energy levels of a system, is commonly referred to as vibrational spectroscopy.

The quantum mechanics of vibrational spectroscopy is covered in many elementary spectroscopy texts [1-3] and it will not be discussed in any detail in this

dissertation. The usual approach involves first discussing the vibrations of diatomic molecules and then detailing the vibrations of polyatomic molecules. The selection rules, transition moments and spectral lineshapes associated with vibrational spectroscopy are often presented as well.

Classically, the attenuation in irradiance as a wave traverses a medium is explained by examining the time-averaged Poynting vector, $\langle \vec{S} \rangle$, for time harmonic fields [4]:

$$\langle \vec{S} \rangle = 0.5 \operatorname{Re} \langle \vec{E} \otimes \vec{H}^* \rangle \quad (2.1)$$

where \vec{E} and \vec{H} are the electric and magnetic vector fields, respectively.

For a plane wave [4],

$$\vec{E}(\vec{x}, t) = \vec{E}_0 e^{i\phi(\vec{x}, t)} \quad (2.2)$$

$$\vec{H}(\vec{x}, t) = \vec{H}_0 e^{i\phi(\vec{x}, t)} \quad (2.3)$$

Here, \vec{x} is the directional distance traveled from some specified origin, t is the time interval relative to some reference time, $\phi(\vec{x}, t)$ is the phase of the wave, and \vec{E}_0 and \vec{H}_0 are vectors constant in time and space (commonly referred to as the amplitude vectors). For such a wave

$$|\vec{S}| = 0.5 \operatorname{Re} \left\{ \sqrt{\frac{\varepsilon}{\mu}} |\vec{E}_0|^2 \exp\left(-\frac{4\pi n'' z}{\lambda}\right) \right\} \quad (2.4)$$

where ε is the complex permittivity, μ is the permeability, n'' is the imaginary component of the complex refractive index, λ is the wavelength of the radiation,

and z is the optical path length traveled in a specified direction. The irradiance, I , which is equivalent to $|\bar{S}|$, is thus given by

$$I = I_0 \exp(-\alpha z) \quad (2.5)$$

where the absorption coefficient is $\alpha \equiv 4\pi n'' / \lambda$. In principle, all processes that remove radiant energy from a beam of radiation, whether by converting the energy into some other energy form (e.g., absorption followed by non-radiative processes) or changing the direction of energy flow (e.g., scattering), contribute to the absorption coefficient.

The attenuation in irradiance when light passes through a sample is usually quantified in terms of the transmittance or the absorbance of the sample. The transmittance, $T(\nu)$, of a sample at a specified frequency ν is defined as

$$T(\nu) = \frac{I(\nu)}{I_0(\nu)} \quad (2.6)$$

where $I_0(\nu)$ and $I(\nu)$ are the irradiance of the incident and transmitted beam, respectively. Although the terms *intensity* and *irradiance* are often used interchangeably, this synonymous usage is confusing, and it is strictly incorrect; spectral intensity (power per unit area per solid angle) possesses an angular dependence while irradiance (power per unit area) does not [4]. The absorbance, $A(\nu)$, of a sample is directly related to its transmittance, and it is defined as

$$A(\nu) = -\log(T(\nu)) \quad (2.7)$$

An absorption spectrum is displayed typically by plotting absorbance versus frequency or wavelength.

There are essentially two methods of obtaining an IR spectrum. One technique involves measuring the absorbance of a sample at each individual wavelength separately. To perform these measurements, radiation of suitable monochromaticity, *i.e.*, narrow bandwidth, is required, and thus this technique utilizes a dispersing element to separate polychromatic IR radiation into its component wavelengths. An IR spectrum can also be obtained without physically separating the electromagnetic constituents of a polychromatic, or broadband, source. This technique utilizes a mathematical technique, known as the Fourier transform, and a mechanical device, known as an interferometer, to facilitate the measurement of a spectrum. As a result, the latter method is referred to as Fourier transform infrared (FTIR) spectroscopy.

2.2 Fourier Transform Infrared Spectroscopy

The history, theory and practice of FTIR spectroscopy has been the subject of many texts [5-7]. In fact, FTIR spectrometers have been commercially available for almost half a century [8]. A thorough review of this technique necessarily includes its numerous practical and theoretical issues; but such a review is intrinsically long, and can be tedious to peruse. The goal in this chapter is by no means to present an exhaustive analysis of FTIR spectroscopy. Instead, a basic introduction shall be provided by summarizing some of the salient theoretical and practical aspects of this method. The desired outcome is a coherent picture detailing the capabilities and limitations of FTIR.

2.3 The Michelson Interferometer

While there are several different interferometer designs, they are all in effect variations of the first interferometer constructed by Albert Michelson in 1891 [5, 7]. Consequently, a convenient approach to understanding how these devices work is to first understand the operations of their progenitor, the Michelson interferometer. A Michelson interferometer (Figure 2.1) consists of a beamsplitter and two mirrors. Essentially, it is a device that splits a beam of radiation into two and then recombines the two resultant beams after introducing a phase difference between them.

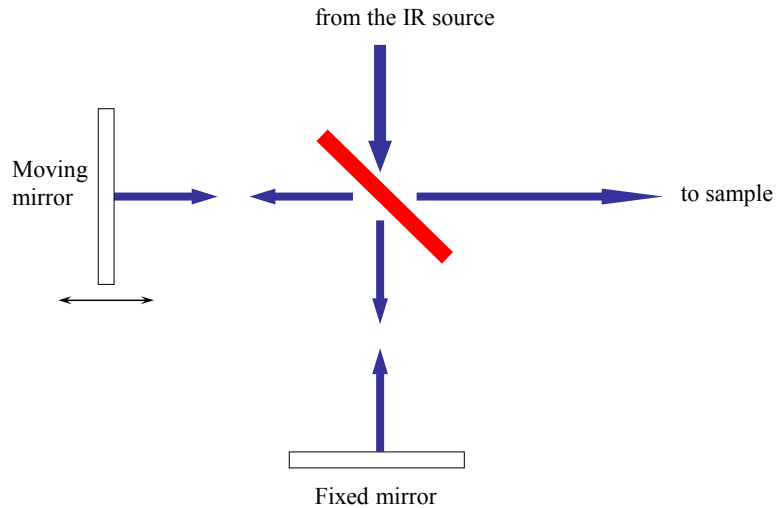


Figure 2.1. Radiation (shown in blue) from a broadband IR source is split by a beamsplitter (red) and directed toward two mirrors. The radiation reflected from these mirrors recombines at the beam splitter. The radiation reflected back to the source during this recombination has been omitted for clarity. The moving mirror is used to change the path difference between the two beams.

The effect of this beam splitting and re-combination is performed constructively by considering the fate of a homogenous monochromatic plane wave incident on a beamsplitter. As previously stated, the electric field, $\vec{E}(\vec{x}, t)$, of a plane wave can be represented classically by

$$\vec{E}(\vec{x}, t) = \vec{E}_0 e^{i\phi(\vec{x}, t)} \quad (2.8)$$

and the irradiance of this wave is proportional to $|\vec{E} \cdot \vec{E}^*|$, *i.e.*,

$$I = K |\vec{E} \cdot \vec{E}^*| \quad (2.9)$$

where K is the proportionality constant relating I and $|\vec{E} \cdot \vec{E}^*|$. The phase of the wave can be expressed as

$$\phi(\vec{x}, t) = \vec{k} \cdot \vec{x} - 2\pi\nu t \quad (2.10)$$

where \vec{k} is the wave vector. For the sake of convenience, it is advantageous to assume the beamsplitter divides the beam into two equal parts and the center of the beamsplitter is the spatial origin. It is also advantageous to assume that the beam is fully collimated. Under these assumptions, the two plane waves of equal irradiance generated by the beamsplitter can be represented as

$$\vec{E}_1(\vec{x}, t) = \frac{E_0}{\sqrt{2}} e^{i\phi_1(\vec{x}, t)} \quad (2.11)$$

$$\vec{E}_2(\vec{x}, t) = \frac{E_0}{\sqrt{2}} e^{i\phi_2(\vec{x}, t)} \quad (2.12)$$

These are two waves traveling in different directions, each propagating towards one of the mirrors (Figure 2.1) where they are reflected back to the beamsplitter. If the

path lengths traversed by wave $\bar{E}_1(\bar{x}, t)$ and $\bar{E}_2(\bar{x}, t)$ when they recombine at the beamsplitter are x_1 and x_2 respectively, the resultant wave is

$$\bar{E}_{1+2}(\bar{x}, t) = \frac{E_0}{\sqrt{2}} \left(e^{i(kx_1 + 2\pi\nu t)} + e^{i(kx_2 + 2\pi\nu t)} \right) \quad (2.13)$$

The irradiance of this resultant wave is

$$I_{1+2}(\Delta x) = K \frac{E_0^2}{2} (1 + \cos(k\Delta x)) \quad (2.14)$$

where Δx is the optical path difference, $x_1 - x_2$, also known as the retardation. Using the well-known relationship $k = 2\pi\bar{\nu}$, equation (2.14) transforms into

$$I_{1+2}(\Delta x) = K \frac{E_0^2}{2} (1 + \cos(2\pi\bar{\nu}\Delta x)) \quad (2.15)$$

where $\bar{\nu}$ is the inverse wavelength. Since $-1 \leq \cos(2\pi\bar{\nu}\Delta x) \leq 1$, the irradiance varies sinusoidally between zero and $0.5K|E_0|^2$ as the path difference is changed. Half of this irradiance is directed back to the source, and so the irradiance at the detector oscillates between zero and $0.25K|E_0|^2$ (Figure 2.2a). An extension of the above analysis to encompass two plane waves of different wavelengths incident on the beamsplitter is trivial, and the irradiance for this case is depicted in Figure 2.2 (b).

The overall effect of the interferometer is to modulate the source radiation. Namely, the radiation at the detector is made to have a frequency much lower than the frequency of the source. Prior to passing through the interferometer, 2000 cm^{-1} radiation has a frequency of $6 \times 10^{13} \text{ Hz}$. As Figure 2.2 (a) shows, one cycle for this radiation occurs at the detector when the phase difference is $5 \times 10^{-4} \text{ cm}$, *i.e.*,

$$\Delta x = \Delta x_{\text{cycle}} = \frac{1}{\bar{\nu}} \quad (2.16)$$

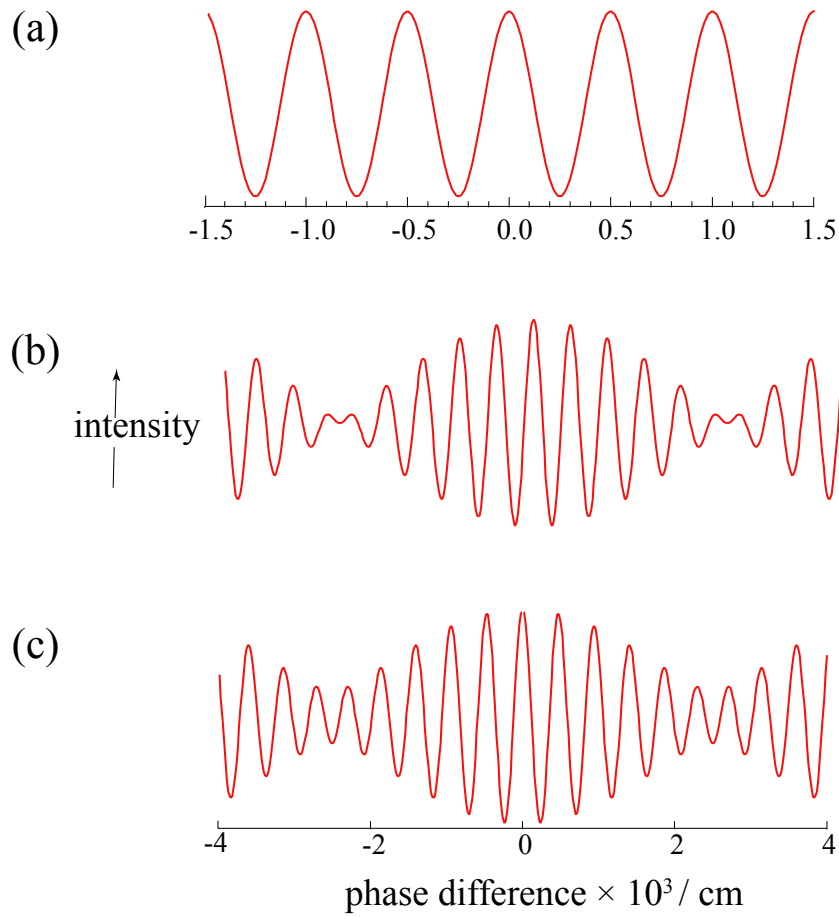


Figure 2.2. The intensity at the detector oscillates as a result of interference. This is shown in plots of $1 + \cos(2\pi\bar{\nu}\Delta x)$ versus phase difference for plane waves of light with (a) one wavelength, 2000 cm^{-1} , (b) two wavelengths, 2000 and 2200 cm^{-1} , with the same irradiance, and (c) two wavelengths, 2000 and 2200 cm^{-1} , of different irradiance (the 2000 cm^{-1} wave has 0.6 the irradiance of the 2200 cm^{-1} wave).

To accomplish this phase difference, the non-stationary mirror moves by

$$\frac{\Delta x_{\text{cycle}}}{2} = \frac{1}{2\bar{\nu}} \quad (2.17)$$

and the time period, Δt_{cycle} , for the moving mirror to travel this distance is

$$\Delta t_{cycle} = \frac{\text{distance traveled by the mirror}}{\text{velocity of the mirror}} = \frac{1}{2\bar{\nu}V_m} \quad (2.18)$$

where V_m is the mirror velocity. Thus, the frequency at the detector is $2\bar{\nu}V_m$. For 2000 cm^{-1} radiation and moving mirror velocities of 0.1-1 cm/s, detector signal frequencies range from 400-4000 Hz. This modulation permits infrared transducers, capable of following fluctuations in the audio frequency range (20 Hz-20 kHz), to be used as detectors in FTIR spectrometers.

The magnitude of the electric field vector, E_0 , is typically different for each frequency, and the irradiance at the detector for two plane waves of different frequency and intensity is shown in Figure 2.2 (c). In general, the irradiance for each wavelength (after passing through the interferometer) is

$$I(\bar{\nu}, \Delta x) = B(\bar{\nu})(1 + \cos(2\pi\bar{\nu}\Delta x)) \quad (2.19)$$

where save for $1 + \cos(2\pi\bar{\nu}\Delta x)$, all terms in equation (2.15) have been grouped into a frequency dependent factor. The last equation conveys simply the fact that the irradiance between wavenumbers $\bar{\nu}$ and $\bar{\nu} + d\bar{\nu}$ is $I(\bar{\nu}, \Delta x)d\bar{\nu}$, and thus the total irradiance at the detector is

$$I(\Delta x) = \int_{\bar{\nu}=0}^{\infty} B(\bar{\nu})d\bar{\nu} + \int_{\bar{\nu}=0}^{\infty} B(\bar{\nu})d\bar{\nu} \cos(2\pi\bar{\nu}\Delta x)d\bar{\nu} \quad (2.20)$$

This implies

$$I(\Delta x) - \int_{\bar{\nu}=0}^{\infty} B(\bar{\nu})d\bar{\nu} = K(\Delta x) = \int_{\bar{\nu}=0}^{\infty} B(\bar{\nu})d\bar{\nu} \cos(2\pi\bar{\nu}\Delta x)d\bar{\nu} \quad (2.21)$$

The phase difference independent term, $\int_{\bar{\nu}=0}^{\infty} B(\bar{\nu})d\bar{\nu}$, is the irradiance at zero path difference, and its experimental determination is relatively straight forward. At various phase differences, $K(\Delta x)$ can thus be evaluated by measuring $I(\Delta x)$ and then subtracting $\int_{\bar{\nu}=0}^{\infty} B(\bar{\nu})d\bar{\nu}$.

2.4 The Fourier Transform

The Michelson interferometer produces a detector signal dependent upon the phase difference, and the critical step is converting this signal into one displaying the irradiance, specifically $B(\bar{\nu})$, at each frequency. In a holistic sense, the Fourier transform can be described as a mathematical technique that converts a function $F(x)$ into some other function $G(y)$; for this transformation to be possible, the variable x must have a dimension that is the inverse of the dimension of y . Two symmetric functions, $F(x)$ and $G(y)$ are said to be a Fourier pair if [6]

$$F(x) = \int_{\bar{\nu}=-\infty}^{\infty} G(y) \cos(2\pi xy) dy \quad (2.22)$$

and

$$G(y) = \int_{\bar{\nu}=-\infty}^{\infty} F(x) \cos(2\pi xy) dx \quad (2.23)$$

As equation (2.21) shows, $K(\Delta x)$ is a symmetric function and thus

$$L(\Delta x) = 2K(\Delta x) = \int_{\bar{\nu}=-\infty}^{\infty} B(\bar{\nu}) \cos(2\pi\bar{\nu}\Delta x) d\bar{\nu} \quad (2.24)$$

Furthermore, because Δx and $\bar{\nu}$ do indeed have inverse dimensionality, $B(\bar{\nu})$ can be written as

$$B(\bar{\nu}) = \int_{\bar{\nu}=-\infty}^{\infty} L(\Delta x) \cos(2\pi\bar{\nu}\Delta x) d\Delta x = 2 \int_{\bar{\nu}=0}^{\infty} L(\Delta x) \cos(2\pi\bar{\nu}\Delta x) d\Delta x \quad (2.25)$$

Equation (2.20) shows that, in theory, $B(\bar{\nu})$ can be calculated once $K(\Delta x)$ (see equation (2.21)) is measured over $0 \leq \Delta x \leq \infty$.

2.5 Practical Aspects of FTIR Spectroscopy

The ideas presented up until this point have been primarily conceptual, and they convey the underlying principles of FTIR spectroscopy. However, the practical implementation of this theory is riddled with many challenges. Firstly, measuring the irradiance to an optical path length of infinity is practically impossible. Placing restrictions on the maximum retardation, Δx_{\max} is equivalent to multiplying the complete interferogram (extending from $-\infty \leq \Delta x \leq \infty$) by a truncation function $D(\Delta x)$ which is unity for $-\Delta x_{\max} \leq \Delta x \leq \Delta x_{\max}$ and zero elsewhere; this is the boxcar function. The spectrum obtained in this situation is

$$B'(\bar{\nu}) = \int_{\bar{\nu}=-\infty}^{\infty} L(\Delta x) D(\Delta x) \cos(2\pi\bar{\nu}\Delta x) d\Delta x = \int_{-\Delta x_{\max}}^{\Delta x_{\max}} C(\Delta x) \cos(2\pi\bar{\nu}\Delta x) d\Delta x \quad (2.26)$$

The Fourier transform of $C(\Delta x)$, which is $B'(\bar{\nu})$, is equal to the convolution of the Fourier transforms of $L(\Delta x)$ and $D(\Delta x)$; this is a result of convolution theory [9, 10]. Basically, the measurement of a spectrum with a spectrometer of finite resolution distorts the true spectrum, $B(\bar{\nu})$.

The extent of this distortion depends upon the characteristics of the true spectrum and the convoluting function. The Fourier transform of $L(\Delta x)$ is $B(\bar{\nu})$, and because $D(\Delta x)$ is a boxcar function [10, 11] its Fourier transform, $f(\bar{\nu})$, is the *sinc*(x) function

$$f(\bar{\nu}) = 2\Delta_{\max} \frac{\sin(2\pi\bar{\nu}\Delta_{\max})}{2\pi\bar{\nu}\Delta_{\max}} \quad (2.27)$$

From its maximum at $\bar{\nu} = 0$, $f(\bar{\nu})$ first becomes zero at $0.5\Delta_{\max}^{-1}$ and the width of this function can be arbitrarily defined as Δ_{\max}^{-1} (Figure 2.3). The interval between the maxima of two *sinc* functions when they are placed as close as possible without any overlap of their main feature (centered at $\bar{\nu} = 0$) is Δ_{\max}^{-1} . Specifically, two such features are sufficiently resolved if they are separated by Δ_{\max}^{-1} , and this value is often defined as the nominal resolution of a FTIR spectrometer. The convolution of $B(\bar{\nu})$ and $f(\bar{\nu})$ is

$$B'(\nu) = \int_{-\infty}^{\infty} B(\bar{\nu}')f(\bar{\nu} - \bar{\nu}')d\bar{\nu}' \quad (2.28)$$

For a $B(\bar{\nu})$ function that is has line width much narrower (*i.e.*, over 3 times narrower) than $f(\bar{\nu})$, the effect of this convolution is to impart the $f(\bar{\nu})$ lineshape to the measured spectrum. For example, the spectrum of a monochromatic line will take on a *sinc*(x) lineshape. Essentially, the resolution of the spectrum is restricted to

a value of Δx_{\max}^{-1} because of the convoluting boxcar function, and

$$\Delta \bar{\nu}_{\text{res}} = \Delta x_{\max}^{-1} \quad (2.29)$$

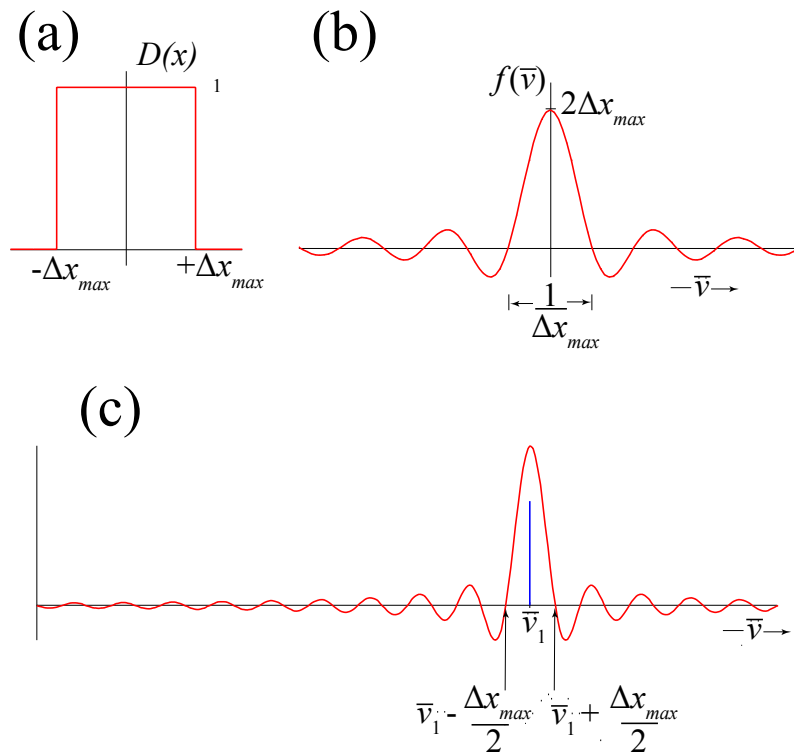


Figure 2.3. The Fourier transform of a boxcar function (shown in (a)) is the sinc function (shown in (b)), and this function has several side lobes adjacent to its main feature. (c) The spectrum of a monochromatic line takes on a $\text{sinc}(x)$ lineshape as a result of the inability to measure the interference signal over $-\infty \leq \Delta x \leq \infty$. The width of the feature obtained is shown.

Indeed, FTIR spectrometer software is configured such that a user specified nominal resolution controls the maximum distance traveled by the moving mirror during each scan.

The $\text{sinc}(x)$ function is not particularly useful because of fairly large amplitudes at wavenumbers well away from the central feature (Figure 2.3). These side lobes can be mistaken for the main feature of a weak transition. The side lobes of a $\text{sinc}(x)$ function were once referred to as *feet* or *podes*, and as a result the process of removing these features is known as apodization. Basically, apodization involves substituting the $\text{sinc}(x)$ convolution function with a simple weighting function to reduce the side lobes. For example, a triangular apodization function [5], which is a commonly used apodization function, distorts narrow absorption lines and imparts a $\text{sinc}^2(x)$ lineshape to these lines. At a peak separation value of $\Delta x_{\text{max}}^{-1}$ there is significant overlap between two $\text{sinc}^2(x)$ functions (as opposed to no overlap in the main feature of two $\text{sinc}(x)$ functions separated by the same value). However, the side lobes are minimized, and the two peaks are still easily discernible (Figure 2.4).

Several other apodization functions exist [12], and they are utilized routinely in FTIR spectroscopy. An ideal apodization function would yield an infinitely narrow function upon Fourier transformation. In general, as the main lobe of the convoluting function gets narrower, the ratio of the magnitude of the strongest side lobe to the central lobe increases. Consequently, the choice of which apodization function to use depends upon the experiment being performed, and some of the necessary considerations are detailed by Griffiths and deHaseth [5].

Another issue of concern in the implementation of FTIR spectroscopy is how to sample the signal reaching the detector. Specifically, the question involves how regularly a signal must be sampled to detect all the frequencies present in the signal

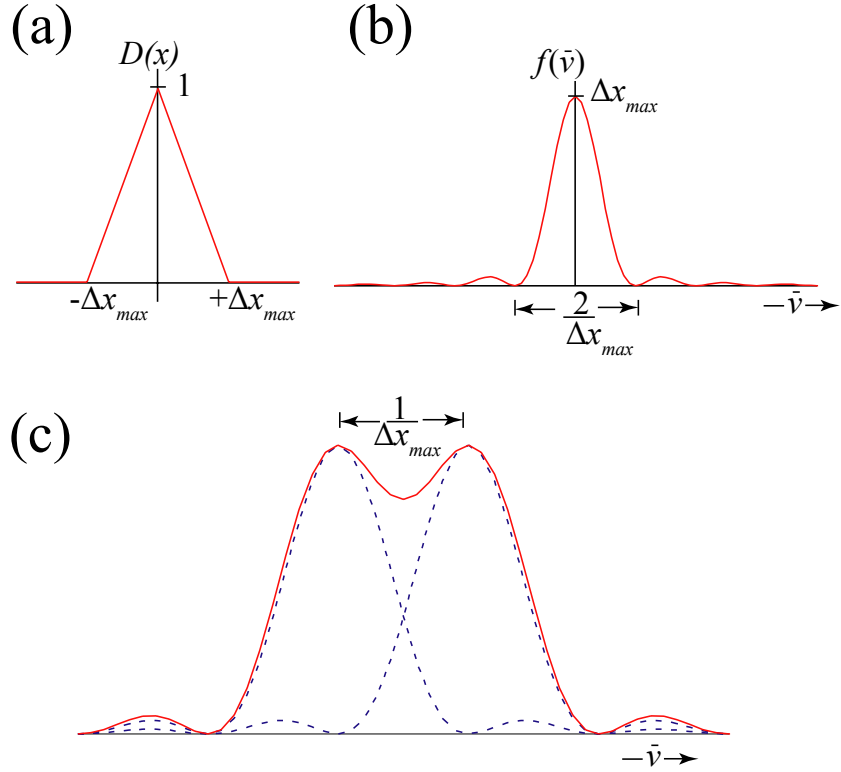


Figure 2.4. A triangular apodization function (shown in (a)) Fourier transforms to yield a sinc^2 function (shown in (b)), which has side lobes that are small compared to the main feature. Although there is significant overlap when two sinc^2 functions are separated by the distance shown in (c), these two functions (blue) are still distinguishable in the combined trace (red). At this separation, two sinc functions would display no overlap in their main feature.

According to the sampling theorem [11], discrete sampling at a frequency of twice the highest frequency present in a signal is necessary and sufficient to meet the aforementioned objective. Consider a source with a maximum wavenumber $\bar{\nu}_{\max}$. The retardation distance for one irradiance cycle for a plane of wavenumber $\bar{\nu}_{\max}$ at the detector is $\bar{\nu}_{\max}^{-1}$ (see equation (2.16)), and this is the shortest retardation distance per cycle amongst the various frequencies from the source. Thus, the minimum

sampling rate is a point every $(2\bar{\nu}_{\max})^{-1}$; this is akin to specifying at least two data points per the cycle for radiation of $\bar{\nu}_{\max}$.

The number of points, N_s , collected during a scan depends upon the nominal resolution specified and the maximum wavelength of the source. This number of points is equal to the maximum retardation divided by the sampling frequency. For a resolution of $\Delta\bar{\nu}_{res}$ and a source with a maximum wavenumber, $\bar{\nu}_{\max}$, N_s is given by

$$N_s = \frac{(\Delta\bar{\nu}_{res})^{-1}}{(2\bar{\nu}_{\max})^{-1}} = \frac{2\bar{\nu}_{\max}}{\Delta\bar{\nu}_{res}} \quad (2.30)$$

It is important to make the distinction between the number of data points per retardation and the number of data points per unit time. The former is a point every $(2\bar{\nu}_{\max})^{-1}$ while the latter is equal to how fast the moving mirror travels a distance of $0.5(2\bar{\nu}_{\max})^{-1}$. For a moving mirror velocity of V_m , this distance is traveled in $(4V_m\bar{\nu}_{\max})^{-1}$.

The time taken to collect a scan at a specific mirror velocity is dictated by the desired resolution. As previously mentioned, the moving mirror must travel $(\Delta\bar{\nu}_{res})^{-1}$ for a nominal resolution of $\Delta\bar{\nu}_{res}$. Consequently, regardless of the number of data points obtained, the collection time at a specified nominal resolution is the same for the same mirror velocity. The slight advantage in minimizing the number of data points comes in the reduction of computer time for data processing. At typical mirror velocities of 0.1-5 cm/s and a nominal resolution of 4 cm^{-1} , a scan is obtained in 0.05-2.5 seconds.

A single scan often possesses too much noise to be useful, and therefore several scans are collected and averaged to produce an interferogram with a suitable signal-to-noise ratio (SNR). The SNR increase, over a single scan, is equal to the square root of the number of scans averaged [13]. However, even when single scans possess an adequate SNR, FTIR spectroscopy is limited in the type of dynamic events it can follow in real time. In principle, a dynamic event with a half-life longer than 500 ms can be characterized by multiple time-resolved spectra [7].

A major limitation in decreasing the scan time comes from the manner in which the moving mirror is translated during data collection. This drive mechanism is restricted to maximum mirror velocities of ~ 5 cm/s, and the technical difficulties associated with modifying this system are, to say the least, challenging [7]. Nevertheless, several new FTIR spectroscopy methods increasing the rate of data acquisition already exist [7].

Up until this point, it has been assumed that the interferogram is symmetric with respect to retardation. In practice, instrumental artifacts often lead to an asymmetric interferogram [5, 7]. As a result, the moving mirror must travel from $-(\Delta\bar{\nu}_{res})^{-1}$ to $(\Delta\bar{\nu}_{res})^{-1}$ to complete a scan at a specified nominal resolution of $(\Delta\bar{\nu}_{res})$. The process of removing these artifacts to obtain the true symmetric spectrum is known as phase correction [5].

As discussed above, the intensity of the radiation incident upon the detector must be sampled in a certain manner to obtain an accurate spectrum. During each measurement, the detector converts this intensity into an electrical signal, which is

then processed, digitized and stored (along with the corresponding phase difference value). This digitization process is performed with an analog-to-digital converter (ADC). At the end of the scan, this digitized data, which is in fact the digitized interferogram, is then transformed into a spectrum.

The dynamic range of an ADC is a measure of the difference between the largest and smallest signals that can be digitized [5]. For example, a 16-bit ADC can be thought of as possessing 2^{16} levels, and therefore it can be described as having a dynamic range of $0-2^{16}$. To digitize a signal ranging from 0-10 V, the difference in magnitude between each level can be assigned a value of $10/2^{16}$ V or ~ 0.1 mV. In this case, any signal less than 0.1 mV cannot be measured, and it is assumed to be zero.

Interferograms from a broadband source are intrinsically signals with a centerburst irradiance that is high compared to regions of the interferogram well displaced from zero retardation. For suitable digitization accuracy, the irradiance of any signal should fall within the dynamic range of the digitizer. Thus, the software for most spectrometers will only permit data collection when irradiance at the detector for zero retardation is less than some maximum value, *i.e.*, the upper limit of the instrument's dynamic range. To limit the irradiance at the detector, screens or grids are placed in the beam path.

Real information can sometimes be excluded during the digitization if the noise level in the analog signal being processed falls outside the dynamic range of the ADC [5]. Hence, the dynamic range of many spectrometers is configured in a

manner that affords digitization of the noise. In fact, the co-addition of spectra only improves the SNR if the noise is large enough to be measured, *i.e.*, the magnitude of the noise falls within the dynamic range of the spectrometer.

The transformation of the discrete interferogram into a spectrum was, to a certain degree, time-consuming prior to 1970. In fact, with a large amount of data points, this transformation became prohibitively time-consuming. However, since the publication of the Cooley-Tukey Fast Fourier Transform algorithm in 1965, this issue has been suitably addressed with the implementation of software programs that perform the discrete Fourier transform relatively quickly [5].

The improved performance of FTIR spectrometers over dispersive instruments is attributed to the multiplex (or Fellgett) advantage and the throughput (or Jacquinot advantage) [5]. For each data point, the sum of the irradiance of light reaching the detector for all wavelengths is recorded (equation 2.20). Thus, at each data point some information is gained about all the wavelengths. This is in contrast to data collection with dispersive spectrometer, where each wavelength is determined separately. The amount of noise at a specific wavelength is related to the time spent observing that wavelength, *i.e.*, collecting information about that wavelength. As a result, with the same experimental parameters (*e.g.*, collection time, source, detector), a spectrum from a FTIR spectrometer will have a better SNR than a dispersive spectrometer; this is called the multiplex advantage. The throughput advantage arises from the fact that the optical throughput of an interferometer and a dispersive spectrometer are different for the same beam of light. The former has a

better throughput, which is a measure of how much the source irradiance is decreased by passing through a spectrometer.

2.6 Temperature Programmed Desorption

As an atom or molecule approaches a surface, it experiences an energetic interaction with the surface constituents much like the interaction two gas phase atoms experience as they approach each other. However, in this case, the incoming particle interacts simultaneously with several surface or near-surface constituents. There are a number of ways to model this event. A simplistic one-dimensional potential scheme, in which the interaction energy depends solely upon the particle's distance from the surface, is the model most widely invoked [14]. In this scheme, a molecule or atom attaches to the surface if it approaches the surface, loses some of its incident energy, and finds itself without enough energy to desorb from, or leave, the surface. In this attached state, the particle is said to be adsorbed on the surface.

Temperature programmed desorption (TPD) is an experimental technique in which the energy required by an adsorbed species to desorb is supplied by heating the surface, and this desorption is monitored by a mass spectrometer. TPD data is presented typically by plotting the mass detector signal, which is proportional to the desorption flux, versus the surface temperature. These traces are referred to as TPD spectra, and one of the primary uses of this technique is to estimate of the energetic barrier for desorption from these traces.

The desorption of a species that remains intact upon adsorption can be represented by the equation [14]



where $A_{(ads)}$ and $A_{(g)}$ denote species A localized on a surface and in the gas phase, respectively. The desorption flux, R_{flux} , in this case is given by

$$R_{flux} = \frac{d[A_{(ads)}]}{dt} = k_d [A_{(ads)}]^n \quad (2.32)$$

where n is the desorption order, $[A_{(ads)}]$ is the surface coverage of $A_{(ads)}$ with units of number of species A per unit area, and k_d is rate constant for the forward reaction of equation 2.31. The desorption order, much like the order of a reaction, cannot be deduced from a stoichiometrically balanced equation, and it is a value that must be determined empirically. Generally, desorption is assumed to be a simple activated process, and thus the rate constant for desorption is [14]

$$k_d = \nu e^{-\frac{E_d}{kT}} \quad (2.33)$$

where ν is a pre-exponential factor for k_d , E_d is the desorption energy, k is the Boltzmann constant and T is the surface temperature. Combining equations 2.32 and 2.33 yields

$$R_{flux} = \nu [A_{(ads)}]^n e^{-\frac{E_d}{kT}} \quad (2.34)$$

As equation 2.34 shows, the desorption flux (and hence the form of the desorption trace) depends on several factors; E_d , ν , and surface coverage.

There are several approaches to analyzing TPD spectra [15-18], and all of these are attempts to extract information about relative surface coverage, desorption energy, and the desorption order. By far the most widely used is the Redhead analysis. The inherent simplicity of this technique is a major reason for its widespread use. However, this simplicity is ultimately its undoing, and several more sophisticated techniques exist to address the shortcomings of the Redhead method.

While the rate constant increases with increasing temperature (equation 2.34), the number of species on the surface ultimately goes to zero when all species have desorbed. This leads to desorption peaks in TPD spectra, with the peak maximum depending upon the concentration of species originally on the surface. For example, the TPD feature for a monolayer (possessing a desorption energy independent of coverage) saturates when a full monolayer is present during the thermally induced desorption.

TPD spectra with well-defined features that can be correlated with molecular, or atomic, monolayer desorption provide an in-situ method of calibrating surface coverage. The integrated area of a TPD spectral feature is proportional to the number of desorbing species (associated with this feature). Thus, the integrated area of a saturated monolayer feature is a convenient measure of the number of species within a monolayer. The integrated areas of other TPD features can then be compared to that of the monolayer, and the total coverage is often defined in terms of monolayers.

In practice, the flux within the mass sensor, which determines the intensity of a mass signal, is actually not the desorption flux at the surface. The local flux at a

point away from the surface depends upon the trajectories of desorbing species. Consequently, for the same surface coverage the measured flux often varies with the position of the surface relative to the mass sensor. It is difficult, if not impossible, to prove that the flux within the mass sensor is effectively the desorption flux at the surface. Thus, most experiments are conducted with the surface at some constant distance from mass detector, *i.e.*, a constant distance for all traces. In this experimental configuration, the measured signal is simply proportional to the actual desorption flux and the proportionality constant relating this two quantities is the same for all spectra.

2.7 Chapter 2 References

- [1] W. S. Struve, *Fundamentals of Molecular Spectroscopy*, John Wiley and Sons, Inc.: New York, 1989.
- [2] M. J. Hollas, *High Resolution Spectroscopy*, John Wiley & Sons, Inc.: Chichester, 1998.
- [3] P. Atkins and R. Freidman, *Molecular Quantum Mechanics*, Oxford University Press: Oxford, 1998.
- [4] C. F. Bohren and D. R. Huffman, *Absorption and Scattering of Light by Small Particles*, John Wiley & Sons, Inc.: New York, 1998.
- [5] P. Griffiths and J. A. De Haset, *Fourier Transform Infrared Spectrometry*, John Wiley and Sons, Inc.: New York, 1986.
- [6] B. C. Smith, *Fourier Transform Infrared Spectroscopy*, CRC Press: Boca Raton, 1996.
- [7] G. D. Smith and R. A. Palmer, In *Handbook of Vibrational Spectroscopy*, J. M. Chalmers and P. R. Griffiths, Eds.; John Wiley and Sons, Inc., New York, 2002, Vol. 1.
- [8] L. Mertz, *Astronomical Journal*, 70, 685, (1965).
- [9] G. B. Arfken and H. J. Weber, *Mathematical Methods for Physicists*, Academic Press: San Deigo, 1995.
- [10] B. Kusse and E. Westwig, *Mathematical Physics*, John Wiley and Sons, Inc.: New York, 1998.
- [11] J. F. James, *A student's guide to Fourier transforms*, Cambridge University Press: Cambridge, 1998.
- [12] R. H. Norton and R. Beer, *Journal of the Optical Society of America*, 66, 259, (1976).
- [13] D. A. Skoog and J. L. Leary, *Principles of Instrumental Analysis*, Harcourt Brace College Publishers: Fort Worth, 1992.
- [14] J. C. Tully, *Surface Science*, 299/300, 667, (1994).
- [15] P. A. Redhead, *Vacuum*, 12, 203, (1962).

- [16] D. A. King, *Surface Science*, 47, 384, (1975).
- [17] A. M. Jong and J. W. Niemantsverdriet, *Vacuum*, 41, 232, (1990).
- [18] C. M. Chan, R. Aris and W. H. Weinberg, *Surface Science*, 1, 360, (1978).

Chapter 3: Experimental Apparatus

3.1 Introduction

Investigations into the nature of molecular interactions with ice are often undertaken using infrared (IR) spectroscopy. For such work, careful consideration must be given to the optical properties of the materials in the IR beam path as it travels from the source to the detector. Depending upon the substrate, IR spectroscopy can be performed in several different modes, *e.g.*, transmission, reflection, and attenuated total reflectance. Naturally, each mode has its advantages and limitations. With respect to ice studies, transmission and reflection absorption IR spectroscopy are both viable experimental techniques, and they have been used with varying degrees of success.

The work detailed in this dissertation was performed in a chamber designed and built to house a host of diagnostic equipment. A thorough description of this chamber can be found elsewhere [1], and only a brief description will be presented here. An emphasis will be placed on the physical aspects of the chamber that relate specifically to the two diagnostic techniques employed for the experiments detailed in this dissertation: transmission Fourier transform IR (FTIR) spectroscopy and temperature programmed desorption (TPD)

3.2 The UHV system

The ultra high vacuum (UHV) system is a three-tiered chamber, with a surface manipulator affixed to the topmost tier (Figure 3.1). The two tiers at the bottom level

of the chamber are designed to permit molecular beam scattering experiments and to accommodate instrumentation commonly required for surface analysis (*e.g.*, Low Energy Electron Diffraction, High Resolution Electron Energy Loss Spectroscopy, and Auger Electron Spectroscopy). The numerous ports at these levels afford a degree of versatility with respect to different experimental arrangements, and these ports also allow the chamber to house several different diagnostics simultaneously. Using a turbomolecular pump (TurboVac 361), pressures of $\sim 2 \times 10^{-10}$ Torr are attained routinely after heating the chamber at temperatures of ~ 400 K for 2-3 days.

During this heating process, which is commonly referred to as a chamber bakeout, regions of the chamber at significantly lower temperatures than other areas of the chamber can develop. At these regions, known as cold spots, the desorption rate is relatively small compared to other areas of the chamber. These cold spots often result in a virtual leak, which is the slow release of species from an area within the UHV system interior. To prevent cold spots from occurring during bakeout, the temperatures at different parts of the chamber are monitored periodically using various thermocouples attached to the chamber, and this ensures a relatively even heating process. Resistive heating tapes, permanently attached to the chamber, are used to heat the chamber, and the heat dissipation from each of these tapes is controlled via variable transformers (Variac).

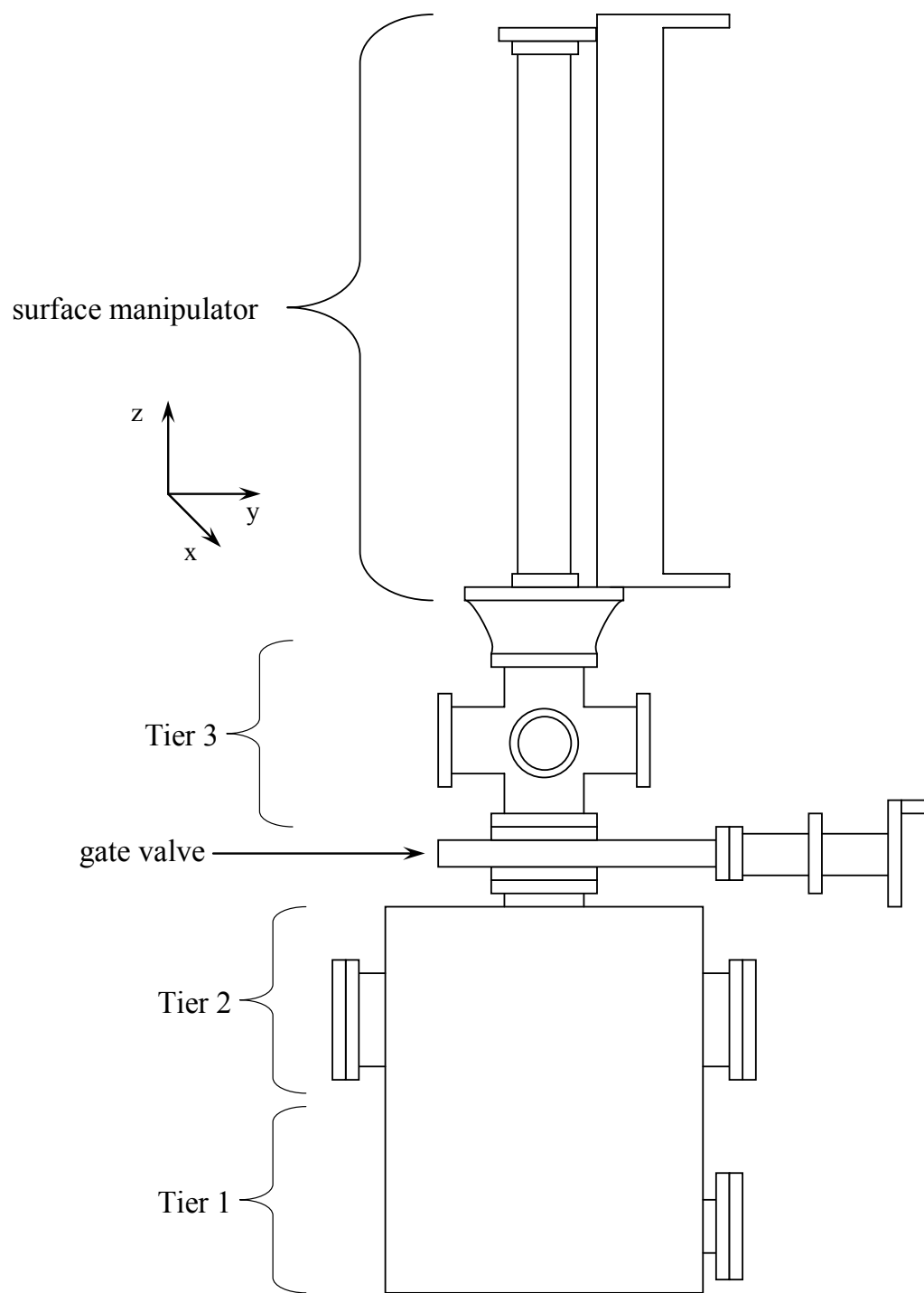


Figure 3.1. A schematic of the UHV Chamber. The numerous ports on tiers 1 and 2 have been omitted for clarity. The entire UHV system is evacuated by a turbomolecular pump located on the second tier.

3.3 The Top Tier: the FTIR Chamber

The top tier of the UHV system was configured specifically for IR experiments, and it is hereafter referred to as the FTIR chamber. It is connected to the levels below it via a gate valve (MDC, GV-4000M), and this permits the FTIR chamber to be vented (*i.e.*, brought up to atmospheric pressures) without necessarily having to vent the entire chamber. After such a venting procedure, it would be desirable to reduce the pressure differential across the aforementioned gate valve, by pumping out the FTIR chamber, prior to opening this gate valve. However, under the existing experimental configuration, the FTIR chamber is evacuated by a turbomolecular pump that evacuates the entire chamber, and this pump is located on the second tier of the chamber. Consequently, the entire system was vented even when changes were made only in the top tier of the chamber.

As Figure 3.2 shows, two calcium fluoride (CaF_2) windows allow IR radiation to enter and exit the FTIR chamber. The experimental set-up used for the IR and thermal desorption experiments discussed in the ensuing chapters was one in which leak valves and a mass spectrometer, a SRS residual gas analyzer (RGA 300), were attached to the chamber at the FTIR level (Figure 3.2). This obviated the need to move between different tiers, as all the equipment necessary for each experiment was on the same level.

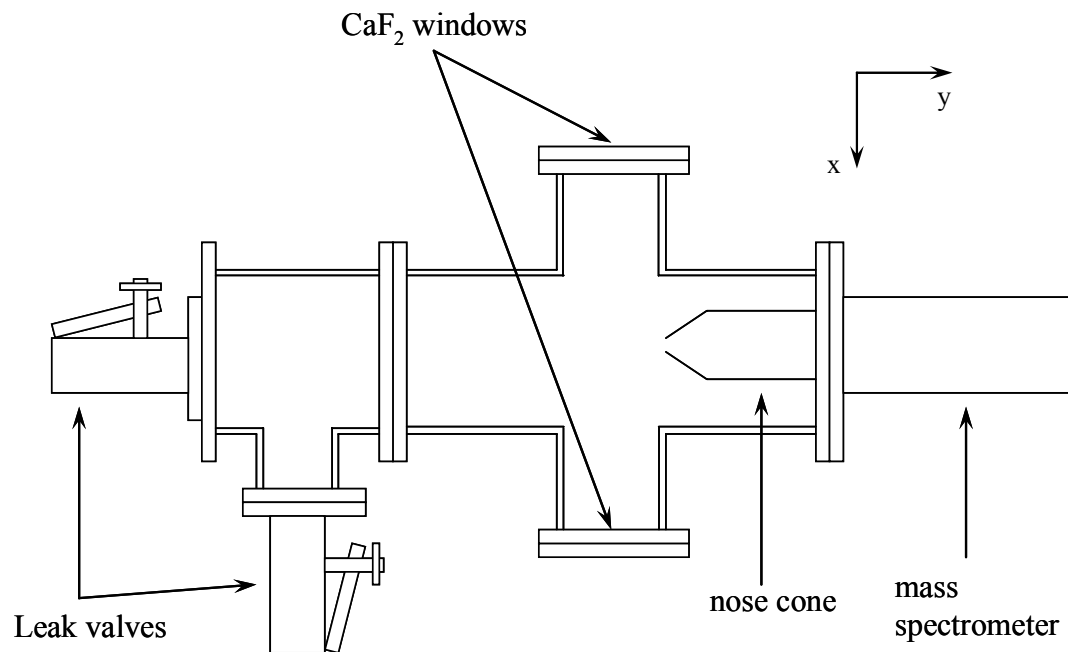


Figure 3.2. A schematic of the FTIR chamber. The axis system shown relates the orientation of this view to the view depicted in Figure 1.

3.4 FTIR Optics and Set-up

To record the IR spectrum of a sample located within the chamber, the collimated beam of a commercial FTIR spectrometer (Nicolet Protégé 740) was directed into the chamber (Figure 3.3). The IR source was a resistively heated silicon nitride filament enclosed in a tubular cavity with a square opening of ~ 5 mm. This device is known as a glowbar, and its spectral output approximates that of a blackbody [2]. The source was situated at the focal point of a mirror with a 87.07 mm focal length. The collimated beam leaving this mirror entered an interferometer, as shown in Figure 3.3. Two mirrors, a mirror with a focal length of 152.40 mm and a flat mirror, directed the beam exiting the interferometer into the chamber. As a result of this

experimental configuration, the beam was focused to ~ 9 mm (*i.e.*, $5.1 \times 152.40/87.07$ mm) within the chamber.

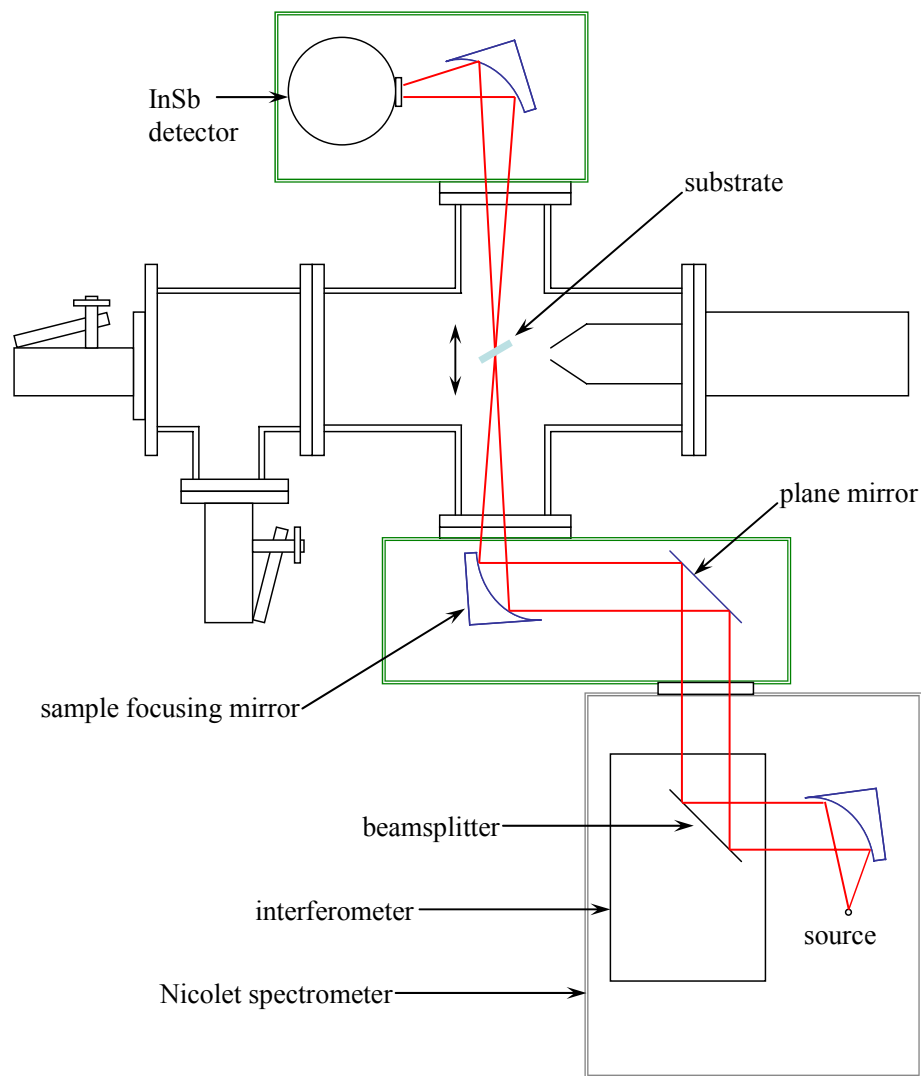


Figure 3.3. A schematic showing the IR beam path from the source to the detector. All pertinent components outside the UHV chamber and the spectrometer are placed in purge boxes (shown in green).

The size of the beam at the sample could not be reduced significantly by simply replacing the mirror focusing the beam into the chamber (*i.e.*, the sample focusing mirror) with a mirror having a shorter focal length. This is because the manipulator allowed the sample to be moved a maximum distance of 12.5 mm from the center of the FTIR chamber when translating the sample along a direction perpendicular to the face of the two CaF₂ windows (Figure 3.3). Hence, the beam could not be focused at the sample if a focusing mirror with a focus length less than 139.9 mm (*i.e.*, (157.4-12.5) mm) was used, and this placed a limit on the beam size at the sample ($\sim 5.1 \times 139.90/87.07$ mm). Instead, the beam size at the sample could be reduced by placing an aperture between the sample focusing mirror and the plane mirror (Figure 3.3). However, an aperture also reduces the intensity of the incident radiation at the sample, and so it was not used in any of the work reported herein.

An IR detector, with a indium antimonide (InSb) element (~ 2 mm \times 2 mm), converted the intensity of the IR radiation exiting the chamber into an electrical signal. To reduce noise from thermally induced transitions among close lying energy levels of this element, it was cooled with liquid nitrogen. This liquid nitrogen was located in a dewar that was in thermal contact with the InSb element; a dewar is a container consisting of two walls with an evacuated space in between them to reduce thermal energy loss. A filled dewar remained at liquid nitrogen temperatures for ~ 20 hours. As with all photoconductive detectors, the absorption of radiation by the InSb element changes its conductivity, and this change is measured by an electrical circuit.

CO₂ and H₂O have relatively strong absorptions in the mid-IR region (4000-2000 cm⁻¹), and FTIR spectrometers are often evacuated or purged to reduce the concentrations of these species in the beam path. To this end, all optics outside the spectrometer were placed in two Plexiglas boxes (Figure 3.3), and both the spectrometer and these boxes were purged with air filtered by a Whatman (FTIR 75-62) purge gas generator. An in-house air compressor supplied this generator with unfiltered air.

A wire grid polarizer (Molelectron, 93-98 % purity) placed in the IR beam path produced polarized IR radiation. This polarizer, which consists of a regular array of fine parallel aluminum wires on a barium fluoride (BaF₂) support, only transmits radiation of a certain polarization. Hence, there is a marked decrease in beam intensity after it passes through the polarizer. The exact mechanism that allows such an arrangement of wires to only transmit radiation with an electric field parallel to them is currently unclear [3].

The intensity of the IR source tends to decrease with time, and this can result in insufficient radiation at the detector. More importantly, an aging source may begin to exhibit significant intensity fluctuations from scan to scan. An average of such scans results in noise levels that are higher than the noise levels in an average, of the same number of scans, from a more stable source. The peak-to-peak absorbance (Figure 3.4) of a spectrum in a region that does not coincide with any known spectral feature is a reasonable measure of noise [4]. Using the experimental set-up described above, a peak-to-peak absorbance of $\sim 2 \times 10^{-4}$ was obtained routinely at ~ 2700 cm⁻¹, and this

corresponds to a transmittance of 0.9998. The spectral feature of any species was easily discernible as long as it was ~ 5 times larger than this typical noise level.

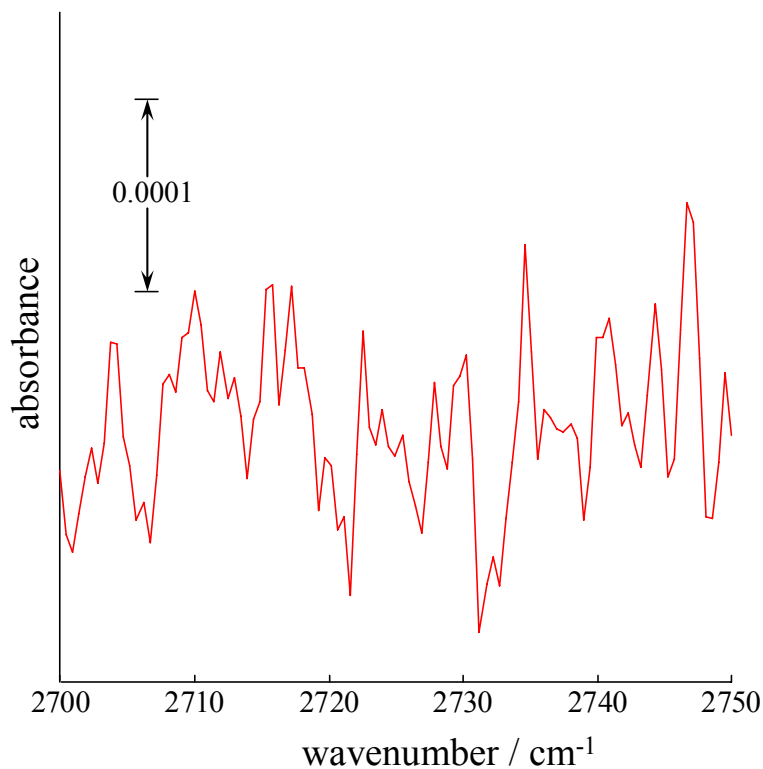


Figure 3.4. The peak-to-peak absorbance routinely obtained in the $\sim 2700 \text{ cm}^{-1}$ region with the experimental configuration described in this chapter.

3.5 The Surface Manipulator

A sample manipulator was used to control the sample position in the chamber, and this manipulator was a modified version of a manipulator designed and built by K. J. Lesker from Vacuum Generator parts [5]. In brief, the manipulator has a stainless steel tube that extends into the three-tiered vacuum chamber (Figure 3.5),

and this tube can be translated along three mutually perpendicular axes. Movement along one of these axes simply permits the end of the tube to move between the different tiers of the chamber, and the maximum distance the tube can be moved in this direction is ~600 mm. A copper piece is brazed onto one end this tube while the other end is open (Figure 3.5). Filling the tube with liquid nitrogen through its open end, cools the tube and the copper piece attached to it. The manipulator also permits the sample to be rotated by 360°.

3.6 The Substrate

The ice films studied were grown on a MgO(100) single crystal (~1 mm × 10 mm × 10 mm). In principle, any substrate that transmits light in the spectral region of interest (4000-2000 cm⁻¹) could have been used as an ice film support. The MgO(100) substrate was chosen because it could be prepared easily, and cleaning it *in-situ* was relatively simple. This substrate was prepared by cleaving a MgO crystal (with a thickness greater than 5 mm) twice to expose two fresh (100) crystal faces. This procedure was performed in a Plexiglas box purged by nitrogen gas. The substrate was inserted into the chamber, after attaching thermocouple wires to the substrate and placing it in a copper sample holder.

Thermocouple wires, for a *k*-type thermocouple, were adhered to the edge of the crystal face with a ceramic adhesive (Aremco Products 835M). Sometimes these wires detached unexpectedly from the substrate when the substrate was under

vacuum. To limit this occurrence, several ceramic adhesives were evaluated to determine which was the most suitable for binding thermocouple wires to a MgO surface.

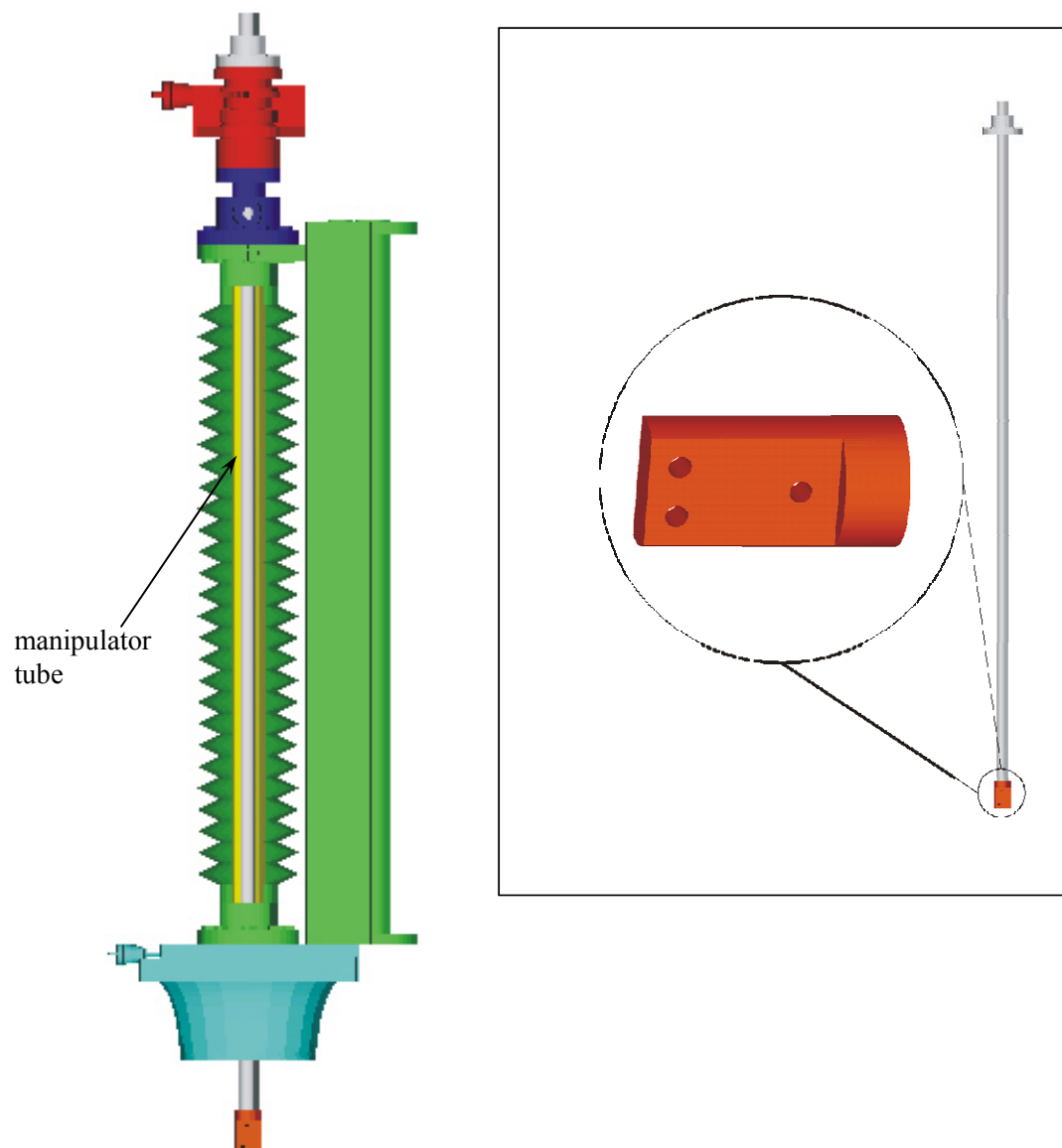


Figure 3.5. The surface manipulator that is attached to the UHV system. The stainless steel tube of the manipulator and the copper piece attached to this tube are shown explicitly in the inset.

3.7 The Sample Holder

The sample holder, which affixed the substrate to the manipulator, had to meet certain requirements. In order to form amorphous ice by vapor deposition, the substrate temperature had to be less than 120 K. Moreover, preliminary experiments and available literature suggested substrate temperatures of 100 K or less were needed to physisorb CO_2 and N_2O on a cold substrate. In addition to this cooling requirement, the sample holder had to be designed in a manner that allowed radiation to be transmitted through the sample. This latter specification implied the substrate could not be cooled by simply placing one of its surfaces on a cold metal surface. Instead, the substrate temperature had to be controlled by heating or cooling the edges of the crystal. The design and construction of a sample holder that conformed to these requirements was an evolutionary process that involved a systematic improvement of several designs. Those various designs have been detailed already [1], and the specific substrate holder used for the experiments reported in this dissertation is shown in Figure 3.6.

Two copper parts (labeled A and B in Figure 3.6), separated by a ceramic spacer, were attached to the copper piece at one end of the surface manipulator's stainless steel tube (Figure 3.5). The three screws that affixed these two parts to the aforementioned copper piece on the surface manipulator tube were electrically insulated from all of these three parts. This was accomplished using ceramic pieces known as ceramic hat washers (McAllister Technical Services). The two pieces were

also separated physically from the manipulator by a flat (~ 1 mm) spherical (~ 25 mm in diameter) sapphire disc (Esco Products).

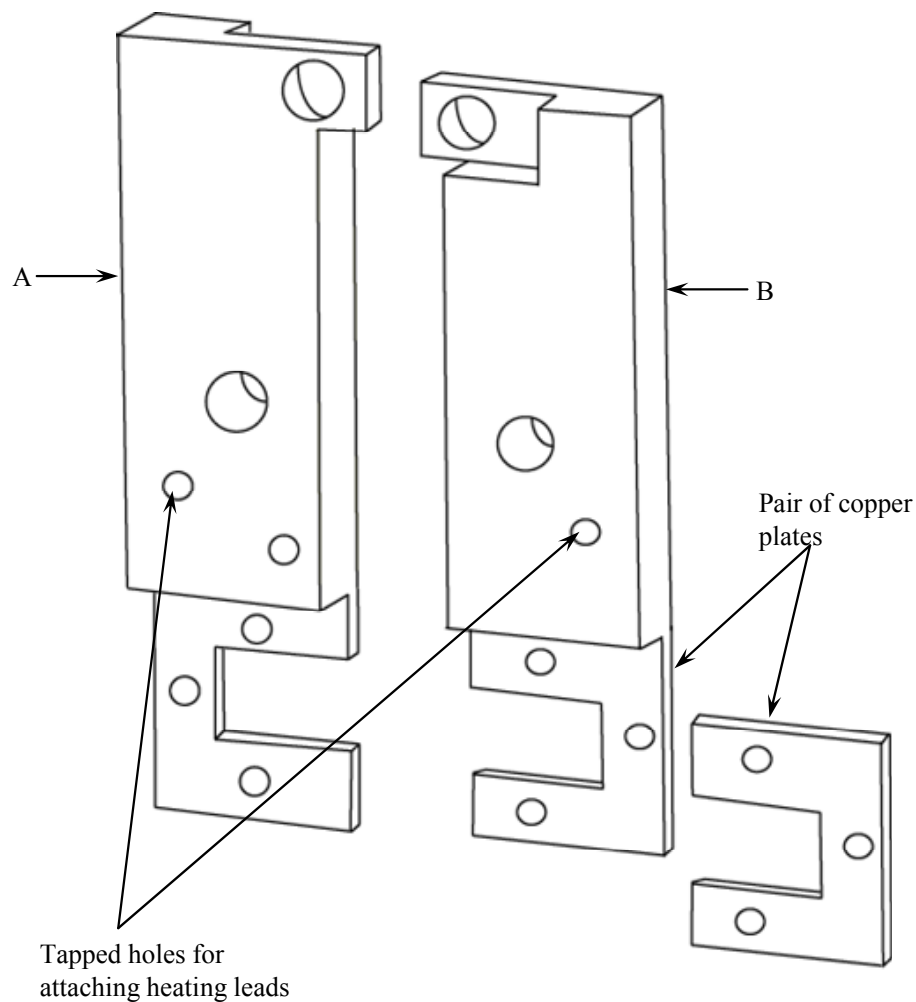


Figure 3.6. A drawing of the surface holder used to attach the surface to the manipulator. The two main copper parts of the holder are labeled A and B. One of the two copper plates that are used to sandwich the surface is shown.

The thermal conductivity of sapphire decreases with temperature. For example, it conducts $\sim 10 \text{ W cm}^{-1}\text{K}^{-1}$ at 80 K, and this value decreases to $\sim 0.3 \text{ W cm}^{-1}\text{K}^{-1}$ at

400 K [6]. Thus, the sapphire disc separating the manipulator from the sample holder ensured that very little heat was transferred from the holder to the manipulator during substrate annealing. In turn, this meant that any species accumulated on the surface of the cold manipulator rod, during vapor deposition onto the substrate, did not desorb during annealing. However, the thermal conductivity of the sapphire disc at ~ 80 K was enough to permit substrate temperatures of ~ 90 K when helium gas was bubbled through the liquid nitrogen cooling tube. Bubbling helium through a dewar of liquid nitrogen is a well-known technique used to decrease the temperature in a dewar [7]. In addition to acting as a thermal switch, the sapphire disc electrically insulated the copper sample holder from the manipulator.

The MgO substrate was attached to the copper sample holder by sandwiching it in between two pairs of copper plates (Figure 3.6). The two previously mentioned copper parts of the sample holder that were attached to the manipulator each extend into a flat plate (Figure 3.6), and each of these plates is paired with another copper plate. Stainless steel screws aid each copper plate pair clamp, or sandwich, the substrate at different edges, and together these plates hold the substrate rigidly in place.

Two narrow (diameter ~ 0.25 mm) tantalum wires placed on one surface of the substrate were used to increase the substrate temperature. These wires were the only electrical connection between the two copper pieces of the sample holder, (*i.e.*, the parts labeled A and B in Figure 3.6). Two leads connected to an external power supply were attached to each of these two sample holder parts, and because of the

high resistivity exhibited by tantalum (compared to copper), essentially all of the resistance in this electrical circuit came from the wires. Hence, these wires generated enough resistive heat to increase the sample temperature from ~ 90 K to ~ 400 K, at a rate of ~ 2 Ks⁻¹, when a current of ~ 18 A was passed through the circuit.

3.8 The Sample Holder: the Second Design

The sample holder design described above could not be used for thermal experiments. To limit the species entering the mass spectrometer detection region to those desorbing from the surface, the mass spectrometer was fitted with a stainless steel "nose cone" with a small (~ 8 mm in diameter) aperture (Figure 3.2). During thermal desorption experiments, the substrate was heated while it was directly in front (~ 1 mm) of the mass spectrometer; the substrate face was roughly parallel to the nose cone aperture. In addition, a fine (wire diameter ~ 0.025 mm) stainless steel mesh (openings ~ 1.3 mm) was placed over the aperture of the cone to prevent electrons, in the mass spectrometer ionization region, from reaching the surface. This mesh was attached by soldering it onto the cone, which was grounded. Even with the nose cone present, the close proximity of the copper plates to the sample made it impossible to prevent species desorbing from these plates from entering the mass spectrometer during thermal desorption. Hence, a new surface holder was constructed, and this holder, hereafter referred to as a sample holder 2, permitted the substrate to be cooled to ~ 90 K and allowed transmission IR and TPD experiments to be performed with the same substrate (Figure 3.7).

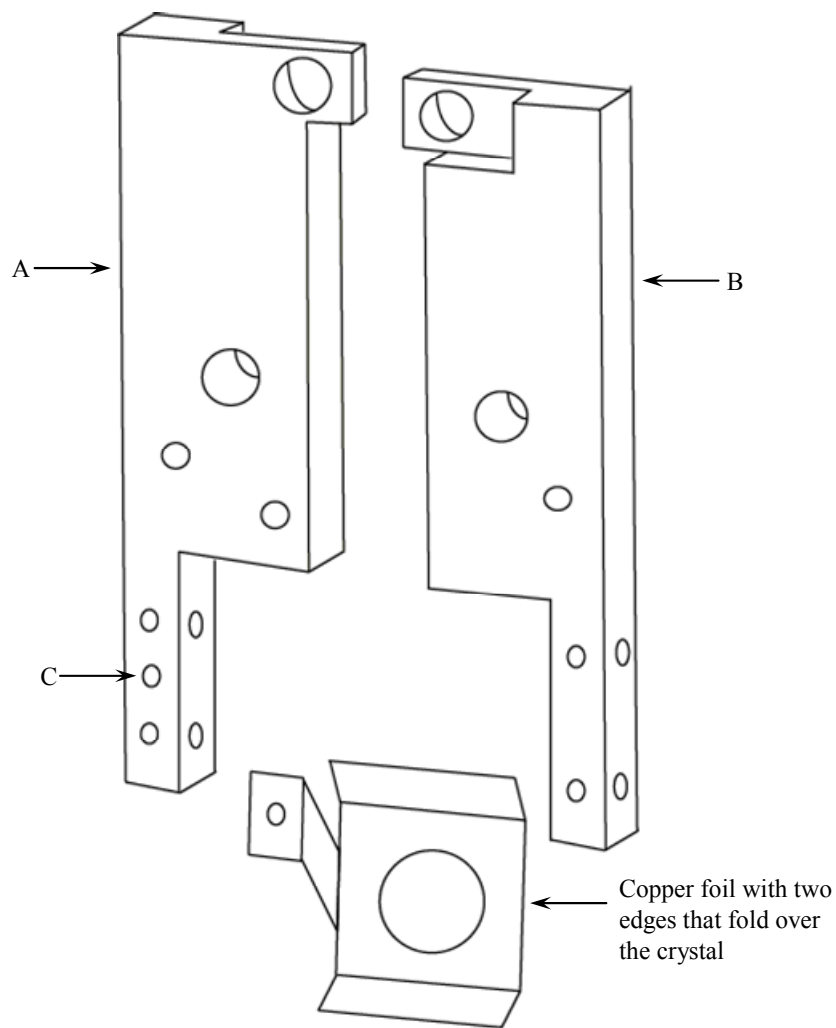


Figure 3.7. A drawing of sample holder 2; the copper foil is attached to the two main parts of the holder (A and B) using a screw (inserted into the tapped hole labeled C).

In this design, the MgO crystal was centered on a flat piece of copper foil (~ 0.2 mm \times 10 mm \times 14 mm), and this piece of foil had a protruding arm extending from one of its edges and a hole (~ 6 mm in diameter) at its center (Figure 3.7). Two

opposite edges of the foil were folded over the crystal to hold it in place. The arm extending from the copper foil was attached to one of two copper parts of the sample holder (parts A and B of Figure 3.7). As with the previous design, these two copper pieces, separated from the manipulator by a sapphire disc, were attached to the manipulator using three screws. In addition, the sample holder, the manipulator and each screw were all electrically insulated from each other.

As mentioned in the previous paragraph, the MgO substrate was placed on one side of a flat piece of foil. A homemade heater was adhered (Aremco Products 835M) onto the *other* side of the foil, and basically this heater was a wire coil made from narrow (diameter ~ 0.25 mm) tantalum wire (Figure 3.8). Several alumina sleeves (Omega Engineering, ORX-132116) were placed around the wire used for this coil to ensure that any current passed into this wire went through its entire length, *i.e.*, several portions of this wire were carefully insulated from each other. This ensured that the heater was a relatively high resistive element. Each end of this wire was connected to one of the two copper parts (Figure 3.7) attached to the sample holder. Two power leads, from an external power supply, were each attached to one the aforementioned copper parts, and consequently, electrical current could be passed through the homemade resistive heater. Using an electrical current of ~ 14 A, the substrate could be heated from ~ 90 K to ~ 500 K at a rate of ~ 2 K/s. Moreover, the hole at the center of the copper foil permitted IR radiation to be transmitted through the sample. During thermal desorption experiments, the face of the MgO

crystal with only two copper strips at two of its edges was placed directly in front (~1 mm) of the mass spectrometer nose cone.

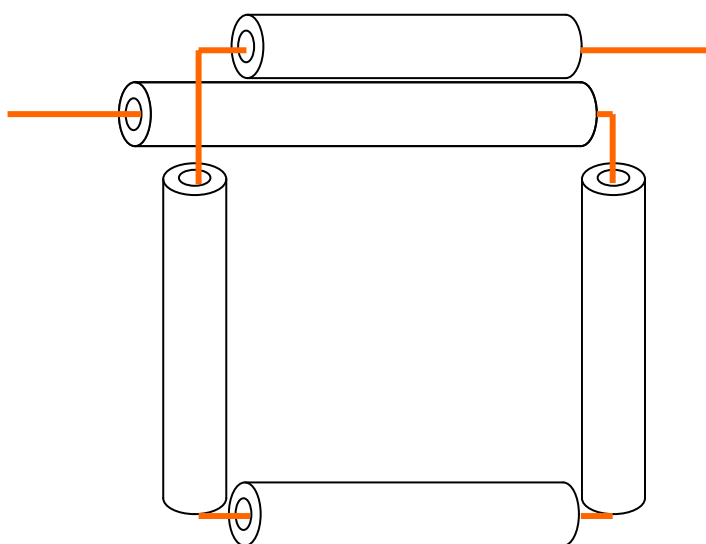


Figure 3.8. The homemade heater is a wire coil with alumina sleeves. The sleeves insulate the wire and ensure current travels throughout the entire length of the wire.

3.9 Sample Preparation

After attaching thermocouple wires to the crystal surface, the surface was mounted onto the manipulator by placing it in a sample holder and connecting this sample holder to the manipulator. The UHV chamber was then closed and evacuated. Prior to pumping out the chamber with the turbomolecular pump attached to the chamber, two cryogenic sorption pumps (Thermionics) were used to reduce the chamber pressure to 10^{-3} Torr. Typically, the turbomolecular pump evacuated the chamber to 10^{-6} Torr within an hour, and at this pressure the bakeout process was initiated. Generally, the chamber pressure increases as the temperature of the walls

increases but eventually this pressure begins to reduce as the temperature of the chamber walls stabilizes at ~ 400 K. When the chamber pressure stabilized, the heaters were turned off and the chamber was allowed to cool to room temperature. This cooling process took approximately 12 hours.

One of the advantages of using an MgO substrate is that it is a relatively inert surface, and annealing it to 500 K essentially removes any contaminants from its surface [8]. However, a contaminant free surface may still contain a lot of defect sites, particularly oxygen vacancies. A relatively clean and defect free surface can be produced by annealing an MgO surface to ~ 700 K in 10^{-7} Torr for 1 hour [8]. All surfaces used for the experiments reported in the ensuing chapters were subjected to this procedure after heating the chamber.

H₂O (distilled and purified by osmosis) was degassed by several freeze-pump-thaw cycles and used to produce vapor deposited ice films. This deposition process was performed typically at ~ 90 K, and this resulted in the formation of amorphous ice films. N₂O (Praxair, 99.999% purity) and CO₂ (Gilmore, 99.99% purity) were used without further purification.

3.10 Chapter 3 References

- [1] S. A. Hawkins: *Fourier transform infrared spectroscopy and temperature programmed desorption of water thin films on the MgO (100) surface*, Ph. D. Thesis, Department of Chemistry, University of Southern California, Los Angeles, 2004.
- [2] D. A. Skoog and J. L. Leary, *Principles of Instrumental Analysis*, Saunders College Publishing: Fort Worth, 1992.
- [3] X. J. Yu and H. S. Kwok, *Journal of Applied Physics*, 93, 4407, (2003).
- [4] B. C. Smith, *Fourier Transform Infrared Spectroscopy*, CRC Press: Boca Raton, 1996.
- [5] M. M. Suchan: *Molecules-surface interactions in HCl/MgO and Water/MgO Systems*, Ph. D. Thesis, Department of Chemistry, University of Southern California, Los Angeles, 2001.
- [6] Sheikh, II and P. D. Townsend, *Journal of Physics E-Scientific Instruments*, 6, 1170, (1973).
- [7] J. Yates, J. T., *Experimental Innovations in Surface Science*, AIP Press Springer-Verlag: New York, 1998.
- [8] L. K. Hodgson: *Photodissociation, molecule-surface collision-induced dissociation and direct adsorbate photolysis of nitroso molecules*, Ph. D. Thesis, Department of Chemistry, University of Southern California, Los Angeles, 1993.

Chapter 4: Transport and Guest-Host interactions in Ice

4.1 Introduction

Understanding interactions between molecules and ice continues to be the focus of numerous experimental and theoretical studies, and the dependence of physical properties on structure makes the determination of ice structures a prerequisite for such research. At low temperatures, water can exist in a number of phases. Of these, amorphous and cubic ices lend themselves readily to ultra high vacuum studies, and consequently a considerable amount of research involving these forms has been carried out.

Amorphous ice, commonly referred to as amorphous solid water (ASW), is a metastable form of ice. It is the most abundant phase of water in interstellar clouds [1, 2]. There is, however, little quantitative agreement among the many published results detailing its physical properties. For example, specific surface areas have been reported that range from ~ 12 to $640 \text{ m}^2 \text{ g}^{-1}$ [3-5].

Recent results by Kimmel and coworkers. show that such disagreements may arise from differences in ice preparation [5]. Their investigations indicated that ASW film morphology depends on both the growth conditions and the thermal histories of the films. Accordingly, meaningful comparisons between ASW studies performed by different groups require clear specification of these parameters.

The main IR signature of ASW is not a good indicator of film structure. Despite the fact that different preparation conditions lead to ASW samples having a number of different physical properties, spectra obtained at different temperatures and by

various investigators display remarkably similar shapes [6, 7]. Thus, these spectra are poor diagnostics. In the 2000–4000 cm^{-1} region, ASW spectra are dominated by a broad band that is $\sim 300 \text{ cm}^{-1}$ wide and centered at $\sim 3250 \text{ cm}^{-1}$. A relatively weak feature at 3696 cm^{-1} is believed to originate from dangling OH (*d*-OH) groups [4, 8]. The hydrogen atoms of these groups do not participate in the H-bonding network present in ice, and hence the term dangling bonds. Compared to the dominant ASW band, the *d*-OH line width is relatively narrow. The broad nature of the main spectral signature makes it difficult to discern subtle changes that occur in this band when ASW interacts with added molecular species. Consequently, the properties of the weak *d*-OH band are often monitored to glean information about such interactions and to explore structural changes induced by annealing.

To circumvent problems that derive from the use of a relatively weak signal as the observable, some studies have exploited IR spectral signatures of probe molecules [9-13]. If these molecules interact weakly with water molecules in the ice film, they may serve as good probes of certain properties. From a spectroscopic standpoint, a good probe should possess certain characteristics: an IR band having a narrow line width (to allow small shifts to be easily discerned), and reasonable oscillator strength to facilitate detection. For example, CO and CF_4 have been used as spectral probes of ice morphology because they fit the above criteria [9, 10, 13].

As probe molecules, both CO_2 and N_2O possess desirable characteristics. For example, in the gas phase, they both have strong IR absorptions in the mid-IR region. It is unclear, however, if the presence of CO_2 or N_2O leads to alterations in ice

structure. Sandford and Allamandola report the binding energy of CO to water to be about one fifth of the energy that binds a water molecule to a water film (~ 0.5 eV) [14]. Thus, it is reasonable to expect that the presence of CO molecules will not lead to significant changes in ice morphology. In contrast, binding energies of around 0.2 eV have been determined for CO₂ desorbing from ice films [14, 15], and therefore interactions between CO₂ and ice might (conceivably) alter ice structure. Though a literature search did not find binding energies of N₂O to ice, they are expected to be similar to those of CO₂.

This study explored the uptake and desorption of CO₂ and N₂O from ASW films by using IR spectroscopy as the main diagnostic. The similar physical properties of CO₂ and N₂O suggested that results obtained with each would be complementary. The observations reported below show that, regardless of the CO₂-ice and N₂O-ice interaction strengths, some spectroscopic characteristics exhibited by CO₂ and N₂O are indeed sensitive to ice morphology. Thus, these molecules can be used to monitor or probe structural changes within the ice film. Moreover, these molecules do not require exceptionally low (< 50 K) temperatures for their accumulation on ice. This obviates the need for helium cooling systems, which are generally more expensive than liquid nitrogen cooling systems.

The *d*-OH band shifts observed in each probe-ASW system are also reported. Silva and Devlin used these shifts to estimate binding energies of certain molecules to amorphous ice [12]. Recent theoretical results, however, suggest that there is no direct correlation between interaction energy and the magnitude of the *d*-OH band

shift. Manca and coworkers state that these shifts appear to be related to the local electric field along the OH bond of a dangling OH group [16]. The *d*-OH band shifts induced by CO₂ and N₂O provide yet another experimental test of theoretical models that attempt to elucidate the physical processes responsible for the *d*-OH vibrational frequency. Moreover, the small sizes of CO₂ and N₂O should facilitate their inclusion into quantum mechanical models.

4.2 Experimental Details

Experiments were carried out using the ultrahigh vacuum chamber and experimental configuration described in the previous chapter. The MgO (100) single crystal sample (~1 mm × 10 mm × 10 mm) was prepared under dry nitrogen conditions and quickly inserted into the chamber. A *k*-type thermocouple attached to one edge of the crystal with a ceramic adhesive (Aremco 569) recorded temperature. Sample holder 1, described in the previous chapter, was used to attach the sample to the precision manipulator.

The importance of the minimum temperature (~90 K) obtained routinely with this surface holder cannot be overstated, as maintaining temperatures less than 100 K was crucial to the formation of stable N₂O and CO₂ films. Namely, maintaining suitable concentrations of these molecules on an ice or MgO(100) surface for the 5-10 minutes needed to record a FTIR spectrum required temperatures below 100 K.

Unfortunately, the efficient thermal contact between the sample and the sample holder limited the *maximum* achievable surface temperatures to ~400 K and 200 K,

with samples at room temperature and 90 K, respectively. In addition, the close proximity of the surface holder components to the sample made it difficult to determine the origin of desorbing molecules during temperature programmed desorption (TPD). Thus, the ability to perform accurate and meaningful TPD was sacrificed when using this sample holder.

Purified and de-ionized H₂O was introduced into the chamber via a leak valve following several freeze-pump-thaw cycles. N₂O (Praxair, 99.999%) and CO₂ (Gilmore Liquid Air Company, 99.99%) were dosed through a separate leak valve. In all of the experiments, the admitted gases were background dosed, thereby subjecting both faces of the crystal to the gas, with continuous pumping during dosing.

Each spectrum consisted of an average of 200-500 scans obtained within 5-10 minutes and recorded with 1 cm⁻¹ resolution using a Happ-Genzel apodization function. A cooled surface, flashed to 400 K just before cooling, served as a reference, *i.e.*, the background traces. The InSb detector cut-off frequency of ~1850 cm⁻¹ set the lower limit on the observable frequency range.

Ice films were obtained by exposing the MgO(100) surface to a constant flux of water vapor for a fixed period of time prior to recording sample spectra. Ice thickness was estimated by comparing a film's integrated absorbance with the integrated absorbance of a water monolayer on MgO(100). The IR spectrum of a water monolayer on MgO (100) was determined in experiments preceding this

dissertation work; TPD was used to calibrate water coverage [17]. The adsorbate surface residence time τ can be estimated by using:

$$\tau = \tau_0 e^{\Delta H_{ad}/RT_s} \quad (4.1)$$

where τ_0 typically is assumed to be 10^{-13} s, T_s is the surface temperature, and ΔH_{ad} is the heat of adsorption [18]. The isosteric heat of adsorption of the water monolayer on MgO(100) and the desorption barrier for water molecules on ice are roughly 0.8 and 0.5 eV, respectively [19, 20]. At a surface temperature of 100 K, both the monolayer and multilayer films are stable for several hours because of long residence times. At surface temperatures of 90 K, water vapor deposition resulted in ASW formation. Crystalline (cubic) ice was obtained by annealing ASW films past the phase transition temperature; this phase transition was signaled by changes in the spectral characteristics of the annealed ASW film at ~ 3200 cm^{-1} .

The introduction of N_2O and CO_2 was achieved by exposing water films (and in some cases the MgO(100) substrate) to a background pressure of N_2O or CO_2 for fixed times prior to recording spectra. All probe molecule depositions were performed at 90 K. Ideally, the amount of probe molecules on or within the water film can be estimated by dividing the integrated absorbance of a specific probe IR feature with the integrated absorbance of that same IR feature at monolayer coverage. However, TPD coverage calibrations for these molecules could not be performed because the surface holder suitable for TPD experiments failed to reach temperatures low enough (*i.e.*, < 100 K) for a detectable accumulation of these molecules on the MgO(100) surface. Consequently, the background pressure and

exposure time for each N₂O and CO₂ dose will be stated. The integrated absorbance of a particular probe molecule IR feature (*e.g.*, the asymmetric stretch band) obtained immediately after dosing N₂O or CO₂ onto the MgO(100) substrate at 90 K was approximately proportional to the exposure time at a constant background pressure.

CO₂ has three active IR bands in the 2000-4000 cm⁻¹ region [21], the most intense being the asymmetric stretch ν_3 fundamental near 2349 cm⁻¹. Studies of CO₂ thin films show that this mode splits into the longitudinal optical (LO) and the transverse optical (TO) modes in crystalline CO₂ [22]. The same type of splitting occurs with the ν_3 fundamental mode of crystalline N₂O [22]. The transition dipole moment associated with the LO mode lies perpendicular to the face of the film, while the TO mode transition dipole moment is parallel to the film surface. Consequently, to observe both modes requires incident radiation capable of exciting transition dipole moments perpendicular and parallel to the film surface. As *p*-polarized light meets this criterion, it was used for most the experiments. For these polarization studies, a wire grid polarizer (Molelectron) was placed in the infrared beam path; the angle between the surface normal and incident beam ranged from 48° to 58°.

4.3 Results: Interactions of CO₂ with ASW

The overall shapes of the absorption spectra obtained after depositing CO₂ onto ASW films at 90 K depend on the amount of CO₂ deposited and the ASW film thickness. Figure 4.1 shows the trend observed in the ν_3 region upon depositing varying amounts of CO₂ on ASW films of constant thickness. A single band

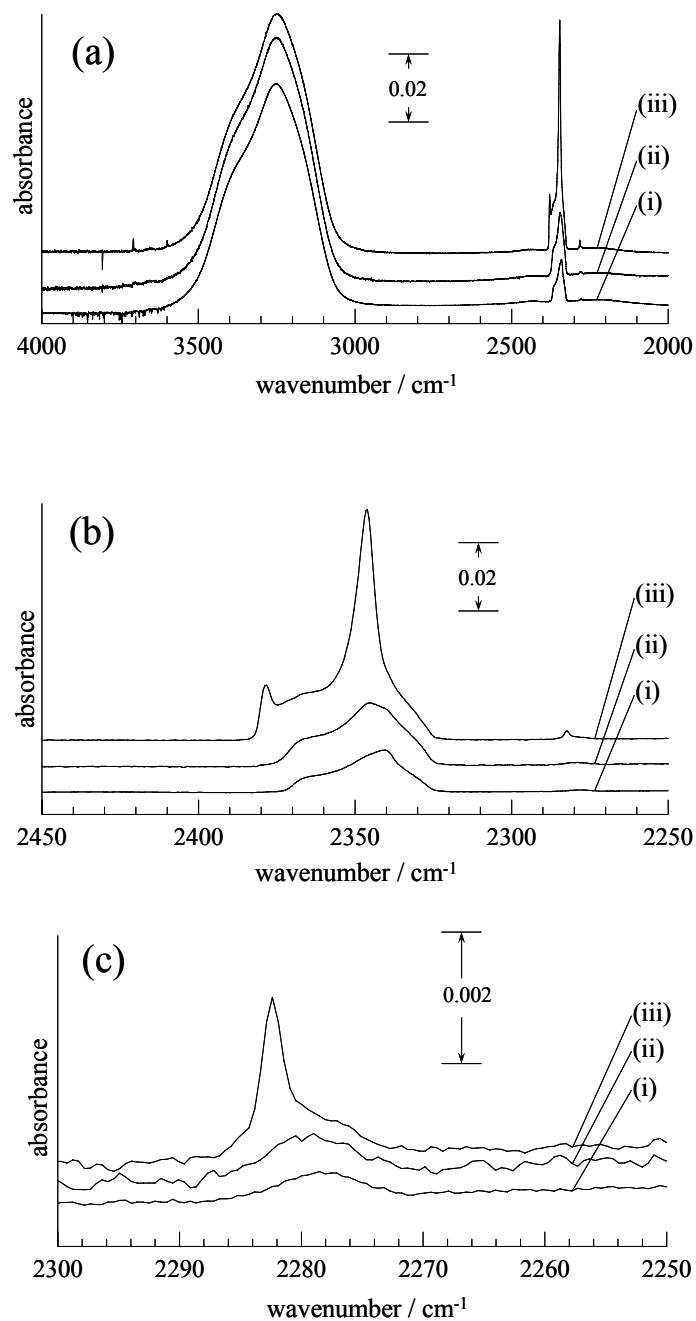


Figure 4.1. (a) Varying amounts of CO₂ deposited at 90 K onto ASW films of approximately constant thickness (~65 layers). CO₂ exposure times (in minutes) at constant pressure (4×10^{-8} Torr) were: (i) 1.5 (ii) 3 (iii) 6. The broad water feature at ~ 3250 cm⁻¹ provides estimates of relative film thickness. The horizontal scale is expanded to emphasize (b) the CO₂ and (c) ¹³CO₂ v₃ region.

(2325-2375 cm^{-1}) was observed with small doses, with peaks at 2379 and 2345 cm^{-1} evident with higher doses. At 90 K, equal exposures of CO_2 to ASW films that differed only in thickness revealed that the thinner the ASW film the greater the intensities of the features at 2345 and 2379 cm^{-1} (Figure 4.2).

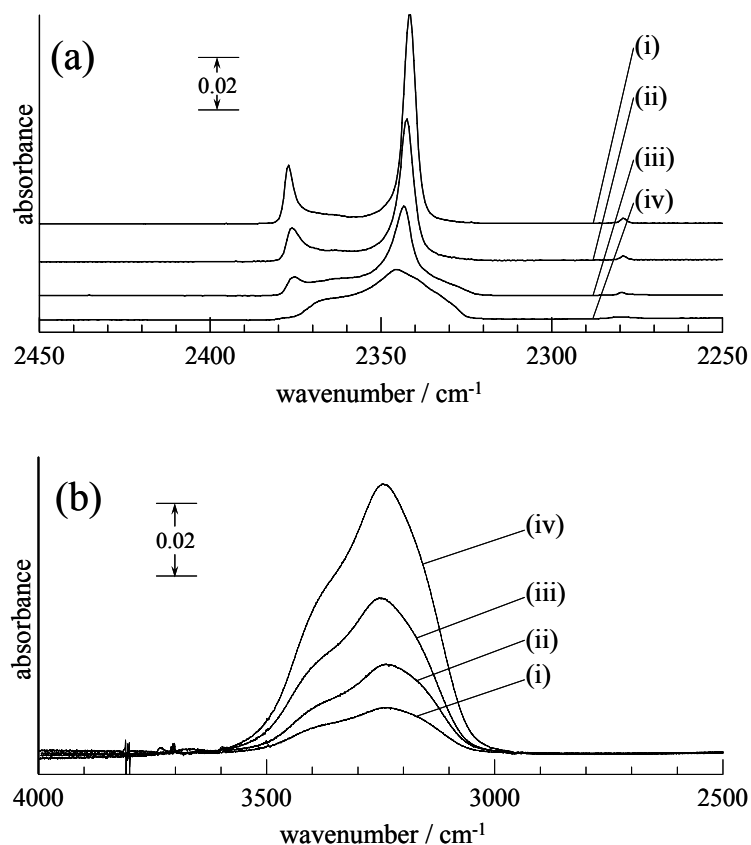


Figure 4.2. The same amount of CO_2 was deposited at 90 K onto ASW films of varying thickness. The films were exposed to 4×10^{-8} Torr CO_2 for 3 min. H_2O exposure times at 5×10^{-8} Torr were: (i) 2 (ii) 4 (iii) 8 and (iv) 16 min, corresponding to 10, 20, 40 and 80 layers, respectively. Entries (a) and (b) show spectral regions for CO_2 and H_2O , respectively.

Referring to Figure 4.1, a band was also observed in the $^{13}\text{CO}_2$ ν_3 region. It consisted of a peak at $\sim 2278\text{ cm}^{-1}$ at low dosage, and a relatively narrow feature at $\sim 2282\text{ cm}^{-1}$ that emerged as the amount of accumulated CO_2 increased [Figure 4.1(c)]. The overall shape of this isotopologue feature depended on both the amount of CO_2 deposited and the ASW thickness. For equal amounts of CO_2 dosed at 90 K, the thinner the ASW film the greater the intensity of the feature at $\sim 2282\text{ cm}^{-1}$. The two small peaks on the high frequency side of the water IR band are CO_2 combination bands [Figure 4.1(a), trace (iii)].

Raising the substrate temperature to 105 K for 15-20 minutes after CO_2 deposition onto an ASW film resulted in a residual CO_2 band around 2340 cm^{-1} . The temperature of 105 K was chosen because experiments involving CO_2 films adsorbed at 90 K on the $\text{MgO}(100)$ substrate showed complete CO_2 desorption by 105 K. Both the maximum peak intensity and the integrated absorbance of the residual band were, to within experimental uncertainty, proportional to the ASW film thickness (Figure 4.3). For ASW films having the same thickness, however, increasing the CO_2 dosage time at 90 K did not necessarily result in a concomitant increase in the integrated absorbance of the 2340 cm^{-1} band (Figure 4.4). In fact, the 2340 cm^{-1} feature appeared to saturate. Namely, for sufficiently long exposure times, the shape and intensity of this band did not continue to increase with exposure. This suggests the amorphous host has taken up the maximum amount of CO_2 that it is capable of absorbing.

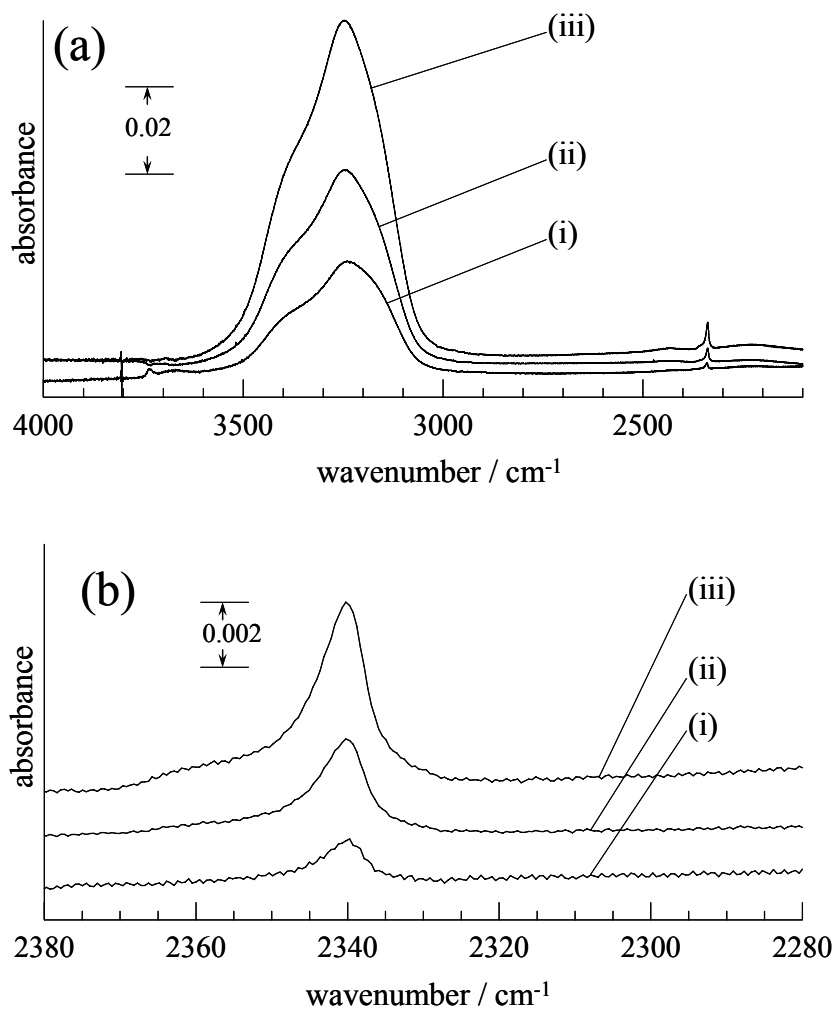


Figure 4.3. Spectra of the CO₂ that remained after depositing at 90 K equal amounts of CO₂ (3 min at 4×10^{-8} Torr) onto ASW films of varying thickness followed by raising the temperature. The temperature was raised to 105 K where it was held for 15-20 minutes before each trace was obtained. Entries (i) – (iii) correspond to ASW films of thickness 20, 40, and 80 layers, respectively. Panels (a) and (b) show the same traces on different horizontal scales.

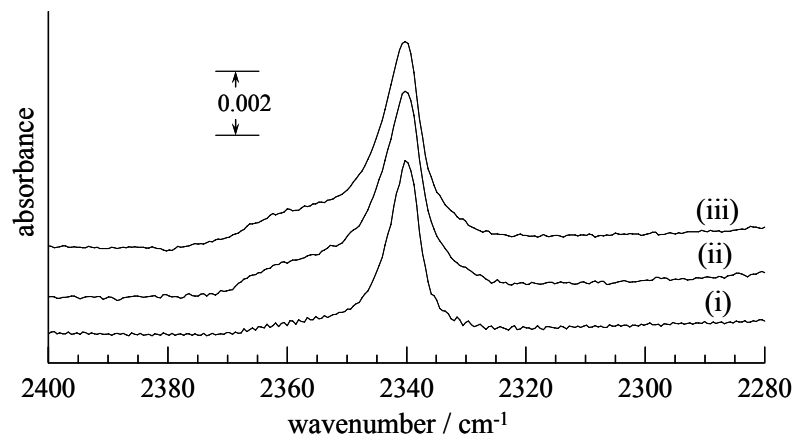


Figure 4.4. Spectra of the CO₂ that remained after depositing different amounts of CO₂ onto ASW films of constant thickness (~65 layers) and then increasing the temperature to 105 K. The spectra were recorded at 105 K, 15-20 min after the reaching this temperature. The CO₂ exposure times at 4×10^{-8} Torr were (i) 1.5 (ii) 3 and (iii) 6 min. See Figure 4.1 for the spectra recorded following CO₂ deposition at 90 K.

The residual CO₂ band was relatively stable up to the ASW phase transition temperature. During the conversion of ASW to cubic ice, the intensity of this band went almost to zero (Figure 4.5). A similar phenomenon involving the release of molecules trapped in porous ice films has been reported previously [23].

It was found that the residual band intensity is sensitive to the amount of water deposited on the CO₂ at 90 K. In a series of "sandwiching" experiments, a fixed amount of CO₂ was deposited between two ASW films. This involved forming the bottom ASW layer, dosing CO₂, and then depositing the top ASW layer. The dosing times for the two ASW layers were chosen in a manner that ensured that the total amount of water in each sandwich remained constant. The results revealed that the thicker was the ASW film on top of the accumulated CO₂, the greater was the

intensity of the residual CO₂ peak. Similar sandwiching experiments could not be performed with crystalline ice films because formation of the top cubic ice film

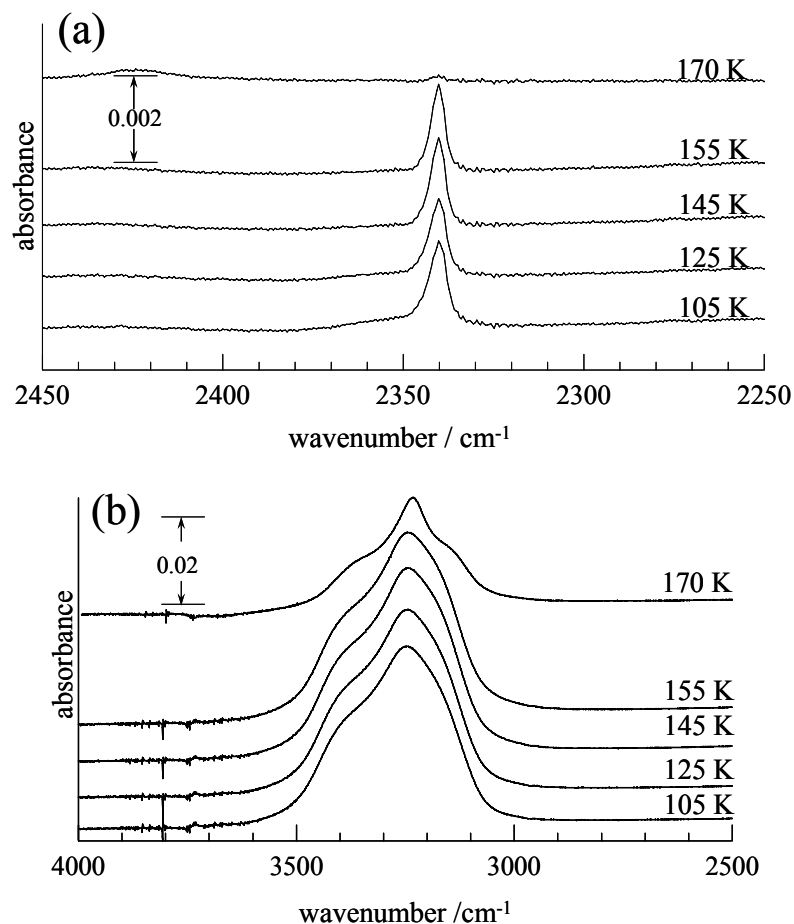


Figure 4.5. CO₂ (4×10^{-8} Torr, 4 min) was deposited onto a 90 K ASW film of 40 layers. The temperature was then raised to 105 K for 15 min, at which time a spectrum was recorded. The figure depicts the evolution of the 105 K spectra as the temperature was increased in steps to the temperatures shown and held at these temperatures for the duration of a scan (~ 8 min). The spectra were recorded immediately after each temperature increase and at the temperatures indicated. Entries (a) and (b) show the spectral region for CO₂ and H₂O, respectively. The broad H₂O feature (~ 3250 cm⁻¹) changes upon annealing past 165 K because of the ASW-to-cubic phase transition.

would require deposition or annealing temperatures greater than 150 K, and CO₂ desorption begins well below 150 K.

The ¹³CO₂ ν₃ region showed no discernable IR signature after 105 K isothermal desorption. This was most likely due to the relatively small percentage of these isotopologues in the CO₂ sample and the small total amount of CO₂ remaining after desorption. Naturally, increasing the total amount of CO₂ remaining at 105 K by increasing film thickness should eventually lead to a distinguishable signature in the isotopomer ν₃ region.

Converting the ASW film to cubic ice via flash-annealing to 170 K prior to CO₂ deposition drastically altered the outcome of isothermal desorption at 105 K. Though cubic ice films were cooled to 90 K before CO₂ adsorption, no CO₂ spectral features remained after 105 K desorption. Changing the thickness of the cubic film and the CO₂ dosing time did not alter this result.

Experiments monitoring the *d*-OH feature utilized ASW films that were more than 800 layers thick. This stemmed from the difficulty associated with observing the *d*-OH IR band in thinner films (*c.f.*, Figures. 4.5 and 4.6). The spectra presented in Figure 4.6 were taken between successive doses of CO₂. Each CO₂ deposition added to previously accumulated CO₂ and a new feature (~3655 cm⁻¹) emerged as the amount of CO₂ increased. Though CO₂ combination bands (3708 and 3599 cm⁻¹) complicate the overall picture, the 3655 cm⁻¹ band is in fact the shifted *d*-OH band.

This conclusion is supported by "N₂O-ASW" spectra that are presented below, in which the absence of N₂O combination bands in this spectral region simplifies the spectrum.

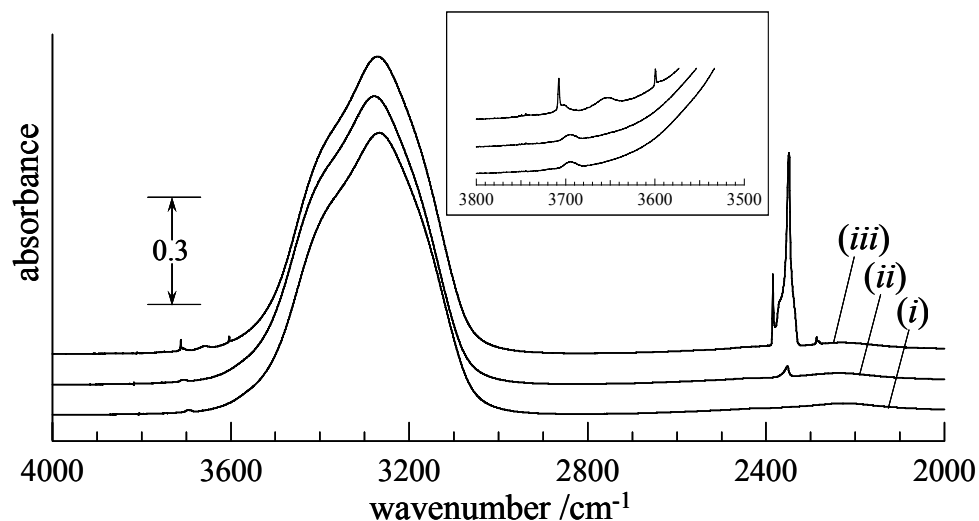


Figure 4.6. Different amounts of CO₂ on an ASW film (~1000 layers). The amount of CO₂ was varied via the sequence: (i) no deposition (ii) 4×10^{-8} Torr for 2 min and (iii) 1×10^{-7} Torr for 16 min. Spectra shown were recorded immediately after each deposition. The inset shows the *d*-OH feature is red shifted as a consequence of CO₂ deposition; namely the feature at ~ 3700 cm⁻¹ moves to ~ 3650 cm⁻¹.

4.4 Results: N₂O Interactions with ASW

The experimental results obtained for N₂O and CO₂ are similar. The nature of the observed N₂O ν_3 features after dosing N₂O onto ASW films at 90 K depended on both the amount of N₂O dosed and the ASW film thickness. At low N₂O coverages, only a single band at 2215-2250 cm⁻¹ was present (Figure 4.7). Two additional peaks at 2238 and 2256 cm⁻¹ were evident at higher coverage. At 90 K, depositing equal

amounts of N_2O onto ASW films that differ only in thickness demonstrated that the thinner the ASW film the greater the intensity of the 2238 and 2256 cm^{-1} features and the smaller the intensity of the 2215-2250 cm^{-1} band (Figure 4.8).

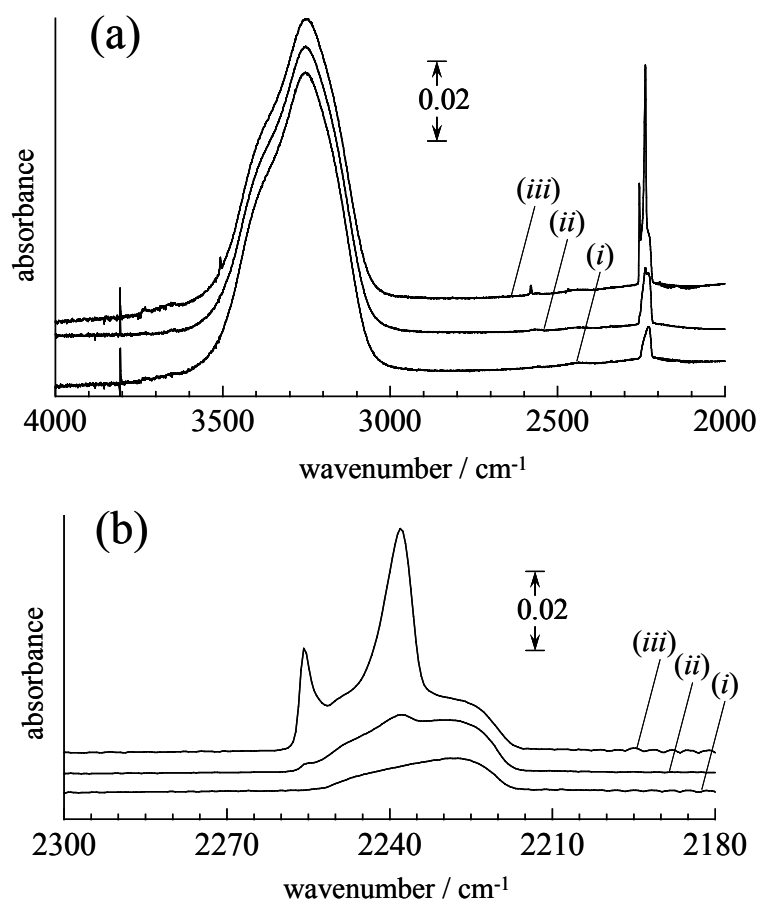


Figure 4.7. (a) Varying amounts of N_2O were deposited onto 90 K ASW films. The broad H_2O feature ($\sim 3250 \text{ cm}^{-1}$) provides an estimate of relative film thickness, which were approximately equal to 70 layers. The N_2O exposure times at 4×10^{-8} Torr were: (i) 2 (ii) 4 and (iii) 8 min. (b) The horizontal scale is expanded to emphasize the N_2O ν_3 region.

Isothermal desorption of the accumulated N₂O (deposited onto an ASW film at 90 K) for 15-20 minutes resulted in a "residual" N₂O band at 2222 cm⁻¹ (Figure.4.9). A desorption temperature of 105 K was chosen because experiments involving N₂O films on the MgO substrate revealed that any N₂O deposited at 90 K desorbed at

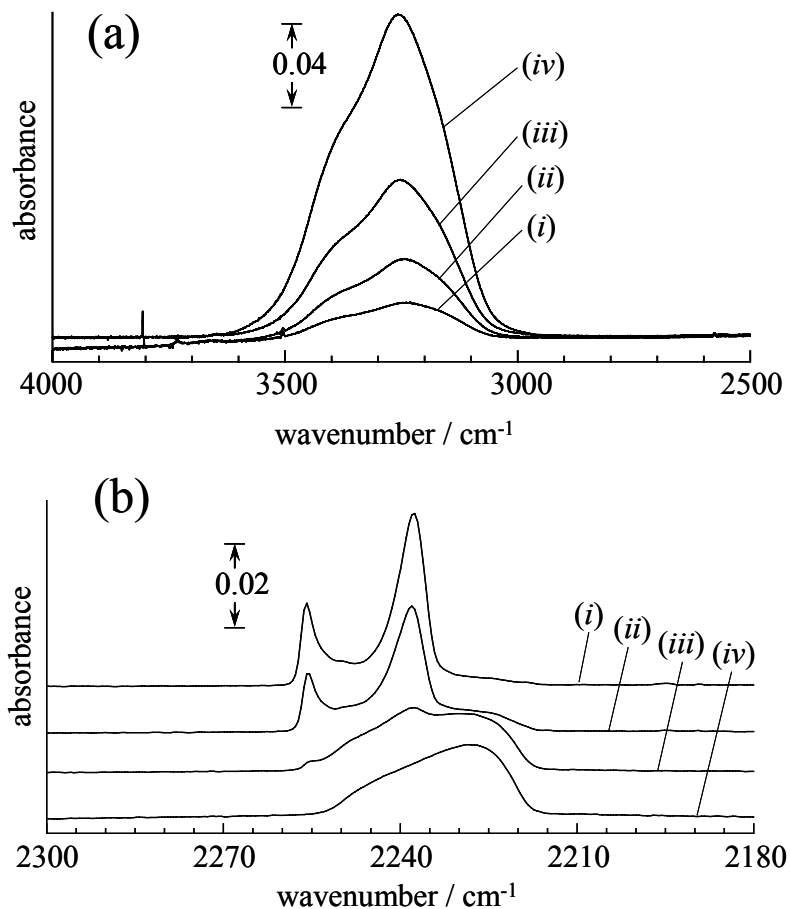


Figure 4.8. (a) ASW films of different thicknesses were prepared at 90 K by vapor depositing H₂O at 4×10^{-8} Torr. (a) H₂O spectra (i) – (iv) were recorded with deposition times of (i) 4, (ii) 8, and (iii) 16 min, corresponding roughly to 15, 35, and 70 layers. (b) Each film was exposed to 4×10^{-8} Torr N₂O for 4 min, and the corresponding N₂O spectra are labelled (i)-(iv).

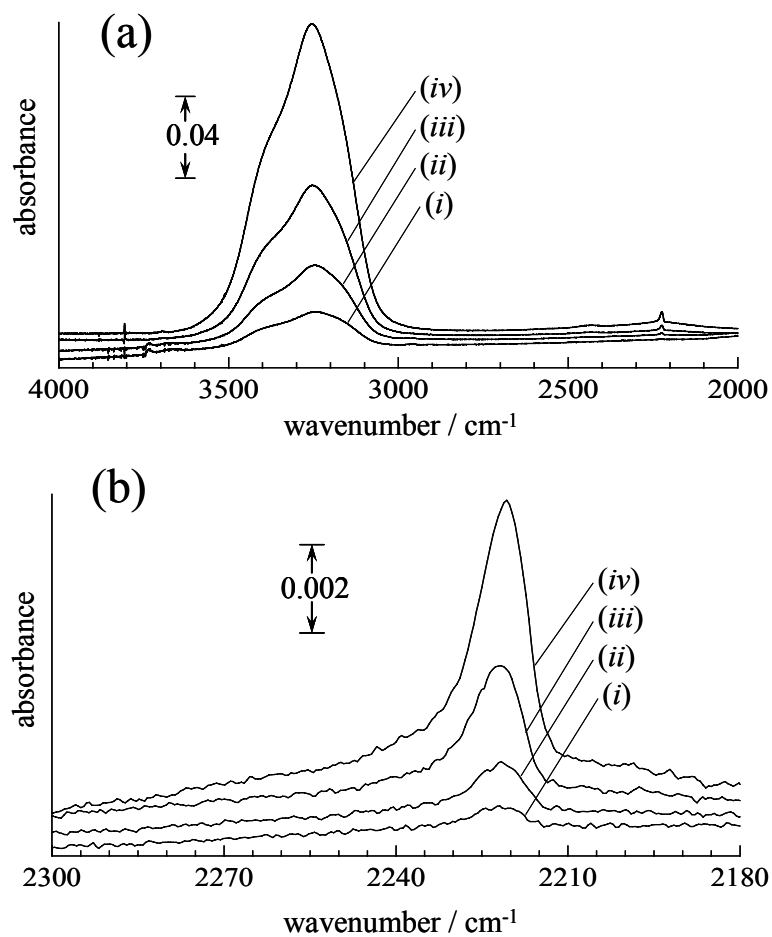


Figure 4.9. ASW films at 90 K were exposed to 4×10^{-8} Torr N₂O for 4 min. The temperature was then raised to 105 K and held there for 15-20 min before a spectrum was recorded. Approximate ASW thicknesses for (i)–(iv) were 15, 35, 70, and 150 layers, respectively. Entries (a) and (b) show H₂O and N₂O features, respectively.

~100 K. Thus, the spectra recorded in these experiments are due to N₂O that is present in the film, rather than on its surface. Figure 4.9 shows the sensitivity of this residual N₂O feature to ASW thickness. For an ASW film of a specific thickness,

doubling the amount of N₂O dosed onto the film at 90 K did not necessarily double the intensity of the spectral feature associated with the remaining N₂O (Figure 4.10). A similar effect was seen with CO₂ (Figure 4.4).

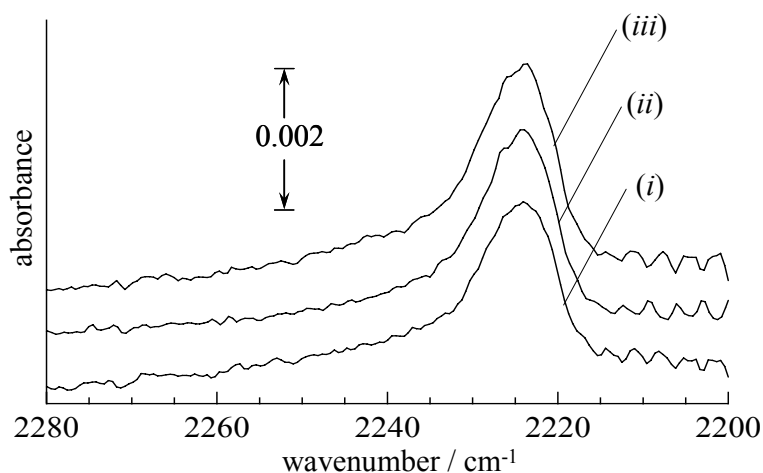


Figure 4.10. Spectra of the N₂O that remained after depositing different amounts of N₂O onto ASW films of same thickness (70 layers) and then increasing the temperature to 105 K. The temperature was then raised to 105 K and held there for 15–20 min before a spectrum was recorded. N₂O exposure times at 4×10^{-8} Torr for (i)–(iii) were 2, 4, and 8 min, respectively.

The N₂O residual feature was stable at temperatures below the ice transition temperature. As shown in Figure 4.11, this IR band persisted even at a temperature of 155 K which is much higher than the desorption temperature of pure N₂O films and only a few degrees below the ASW-to-crystalline transition temperature. Converting the ASW film to crystalline ice prior to 90 K N₂O adsorption resulted in no remaining N₂O features after 105 K isothermal desorption.

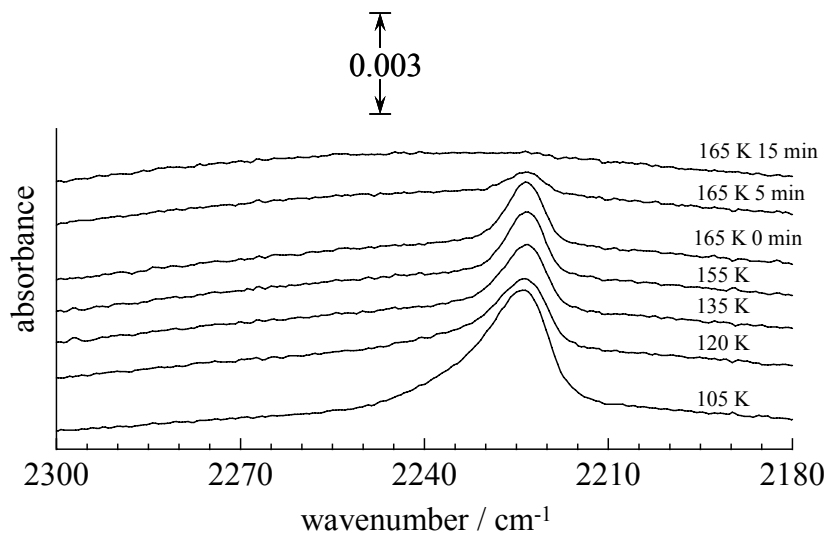


Figure 4.11. N₂O (4×10^{-8} Torr for 4 min) was deposited onto a 90 K ASW film of 40 layers. The temperature was then raised to 105 K for 15 min, at which time a spectrum was recorded. The figure depicts the evolution of the 105 K spectra as the temperature was increased in steps to the temperatures shown and held at these temperatures for the duration of a scan (~ 8 min). The spectra were recorded immediately after each temperature increase and at the temperatures indicated. Three scans (~ 5 min in duration) were recorded at 165 K; the time interval between reaching 165 K and commencing each of these scans is specified for three relevant spectra.

ASW films formed on top of deposited N₂O led to larger residual N₂O intensities, after isothermal desorption, than ASW films situated beneath accumulated N₂O. In a series of experiments, N₂O was sandwiched between two ASW films at 90 K, and, aside from the amounts of water dosed prior to and after N₂O deposition, all variables (*i.e.*, total amount of water and N₂O dosed, deposition and desorption temperatures) were the same in each experiment. All that changed was the respective thicknesses of the lower and upper ASW films. The constancy in the amount of total

water is confirmed by the similarity in shape and intensity of the water IR band (Figure 4.12). As shown in Figure 4.12, the amount of N_2O remaining after 105 K desorption increased with increasing thickness of the top ASW film in these sandwiching experiments. Figure 4.12 can be reconciled by noting: (i) ASW films grown on N_2O overlayers are likely to be more porous than ASW films grown on $MgO(100)$, where there is good registry. (ii) At 105 K, ASW films undergo some degree of annealing, which can trap dopants.

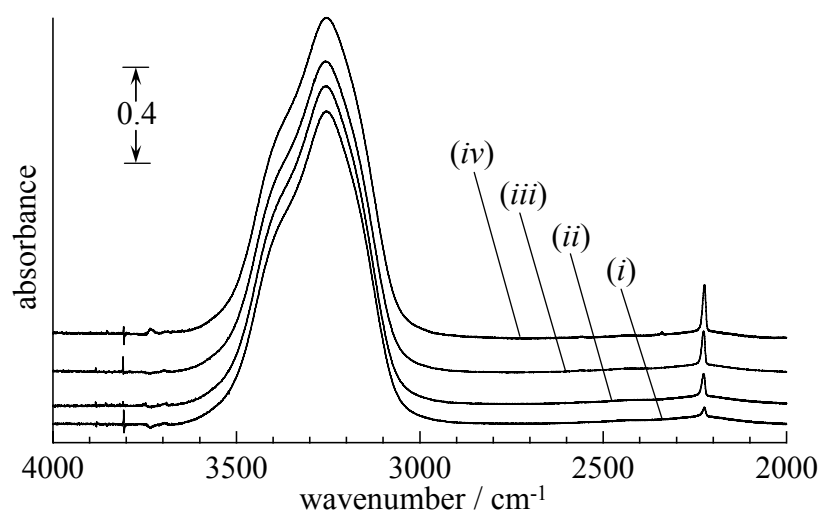


Figure 4.12. Spectra were recorded after sandwiching N_2O between two ASW films at 90 K, then raising the temperature to 105 K, and keeping it there for 15 min. The amount of deposited N_2O and the total number of water layers (~ 80) is the same for all spectra. The ratios of bottom layer to top layer thickness are: (i) 80:0, (ii) 60:20, (iii) 40:40, and (iv) 20:60.

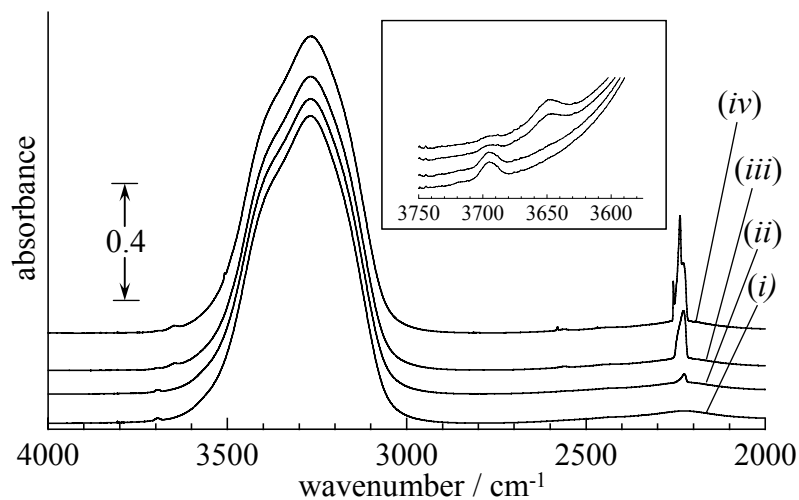


Figure 4.13. Spectra were recorded for different amounts of N_2O deposited onto an ASW film of ~ 1000 layers at 90 K. The amount of N_2O was increased via the sequence: (i) no deposition, (ii) 4×10^{-8} Torr for 4 min, (iii) 1×10^{-7} Torr for 3 min, and (iv) 2×10^{-7} Torr for 7 min. Spectra were recorded immediately following each deposition. The inset shows the $d\text{-OH}$ feature is red shifted as a consequence of N_2O deposition.

The influence of N_2O on the position of the $d\text{-OH}$ peak is shown in Figure 4.13. As mentioned earlier, experiments monitoring the $d\text{-OH}$ band focused on thick ASW films (> 800 layers) because this band was hard to detect in thin ASW films. The spectra presented in Figure 4.13 were taken between successive doses of N_2O and they reveal a $d\text{-OH}$ red shift of $\sim 50 \text{ cm}^{-1}$ as the amount of N_2O accumulates. Also, though some N_2O remains after isothermal desorption at 105 K, the $d\text{-OH}$ peak returns to its original position at $\sim 3700 \text{ cm}^{-1}$.

4.5 Discussion

When molecules are deposited on ice films, an issue to be addressed is where they reside after deposition. Three simple scenarios can be considered. One is that the molecules diffuse through the film and accumulate on the substrate via the displacement of water molecules. A second scenario involves molecules penetrating into the bulk of the ice and residing there. Localization on top of the water film surface is yet another possibility. Nothing precludes *a priori* the simultaneous participation of these processes.

The displacement of water molecules in the first adlayer (*i.e.*, the layer in contact with the MgO substrate) by CO₂ is unlikely. Theoretical studies predict that the heat of adsorption of CO₂ on MgO(100) is $\Delta H_{ad} \sim 0.3$ eV [23]. In sharp contrast, the experimentally determined value of ΔH_{ad} for monolayer water on MgO(100) is ~ 0.8 eV, which is very large for a physisorbed molecule [20]. It is this considerable difference in the ΔH_{ad} values that makes the displacement of monolayer H₂O by CO₂ highly improbable on this surface. It is assumed that this argument also applies to N₂O, despite the lack of theoretical or experimental binding energies for N₂O on MgO(100).

The two IR peaks at 2379 and 2345 cm⁻¹ that emerge as CO₂ coverage increases (Figure 4.1) lie at energies that are similar to the LO and TO resonances of thin, polycrystalline CO₂ films [22]. These peaks also exhibit the same polarization dependence as the aforementioned resonances, *i.e.*, the peak at ~ 2380 cm⁻¹ is

drastically reduced in spectra recorded with *s*-polarized light. Moreover, the $^{13}\text{CO}_2$ band at 2284 cm^{-1} that emerges as the exposure time of CO_2 to an ASW film increases, also appears in the spectra of CO_2 thin films. There is little doubt that these observations imply the formation of a CO_2 thin film. Similarly, the two additional IR features that grow in as N_2O accumulates (Figure 4.7) are correlated strongly with the LO and TO vibrational resonances of N_2O thin films [22]. The propensity of CO_2 and N_2O dosed onto ASW films at 90 K to produce features characteristic of polycrystalline CO_2 and N_2O indicates that enough accumulation of these molecules has occurred on top of the ASW film to yield thin films.

Some CO_2 and N_2O molecules enter the film interior even at 90 K. It is intuitive to assume that a property that varies with film thickness must be related to a phenomenon occurring in the interior. Consequently, it is easy to understand why the dependence of the CO_2 and N_2O band shapes on ASW thickness (Figures 4.2 and 4.8) leads to the conclusion that some of these molecules diffuse into the film at 90 K. Both CO_2 and N_2O are expected to possess significant surface mobility because 90 K is only ~ 10 K lower than the temperature required for appreciable desorption. This mobility facilitates diffusion of small molecules into films [24].

Prior to the formation of a CO_2 or N_2O thin film, the deposited molecules diffuse into and reside within the ASW film at 90 K. Also, the amount of favorable residence sites within ASW films rises as the film thickness grows. These conclusions originate primarily from the fact that film formation is only evident after

a certain amount of CO₂ or N₂O has *already* accumulated. The relatively broad feature initially observed upon dosing these molecules onto ASW films (Figures 4.1 and 4.7) serves as evidence of this prior accumulation. This initial feature is assigned to probe molecules within the ASW film. Moreover, the integrated area of this band just prior to the emergence of the narrow LO and TO resonances scales linearly with film thickness over two orders of magnitude (10 – 1000 ASW layers). The possibility that CO₂ or N₂O molecules are all situated entirely on top of the ASW film and that the apparent influence of film thickness on probe molecule spectra is simply a manifestation of a change in ASW film surface roughness with film thickness is thus eliminated. This is because a surface roughening effect is not expected to maintain a linear relationship with film thickness over such a large range.

The conclusions stated above are consistent with the results depicted in Figures 4.1 and 4.7 where the increase in the LO and TO peak intensity can be correlated with an increase in CO₂ or N₂O film thickness. Specifically, the thinner the ASW film, the less the amount of deposited molecules needed to fill the favorable sites within the ice film before CO₂ or N₂O thin film formation commences on the "populated" ice film (Figures 4.2 and 4.8).

The last statement addresses the issue introduced at the beginning of this section. Namely, where do the deposited molecules reside? Of the three scenarios under consideration, only the latter two are active in the systems under study here.

Moreover, the experimental results obtained were able to distinguish between probe molecule uptake into the bulk versus film formation.

Studies of the adsorption of small molecules often differentiate between monolayer (2D) and multilayer (3D) spectral features [25-28]. In these studies, interaction with the surface affects the energy levels of first-layer adsorbates in a manner that is distinct from the ensuing layers. This leads to monolayer IR signatures (at vibrational energies that differ from those of the multilayer) that saturate because of the finite number of adsorption sites. In addition, many of these investigations observe that the vapor pressure of the overlayers is at least an order of magnitude greater than that of the monolayer. Thus, there is a temperature range in which isothermal desorption removes the multilayer but little of the monolayer.

Neither CO₂ nor N₂O displayed an isothermal desorption temperature that facilitated a distinction between monolayer and multilayer IR features of these molecules. Here, the term monolayer refers to the first layer of CO₂ or N₂O atop the ASW film surface. For example, isothermal desorption of CO₂ deposited onto ASW resulted in a decrease in the CO₂ band intensity until either no CO₂ signature or only the residual CO₂ feature peaked $\sim 2340\text{ cm}^{-1}$ remained; the outcome depended upon the ASW film thickness. The fact that the residual 2340 cm^{-1} peak scales with film thickness indicates that it is not the monolayer band. IR features associated with the monolayer probably coincide with features of the multilayer. Furthermore, such a similarity in the peak positions and desorption temperatures of the monolayer and multilayer support the assumption that the binding energies of molecules in these

two regimes are approximately the same. Martin and coworkers [29] found the difference in adsorption energies between monolayer and multilayer CO adsorbed on ASW to be < 3 kJ/mol.

The fact that residual band integrated absorbance varies linearly with ASW film thickness suggests that this feature originates from CO₂ and N₂O within the film.

Devlin noted that spectra of small molecules and water vapor co-deposited at temperatures ~ 10 K are similar to spectra of molecules absorbed in ASW films [24]. Indeed, FTIR studies of CO₂-H₂O ices [14], formed at 10 K and warmed to temperatures above 100 K demonstrate that these mixtures have a band at 2340 cm⁻¹. The substantial release of trapped molecules during the phase transition of ASW has been observed in previous studies [23, 30]. Because this occurs as the film crystallizes, it depends on the experimental conditions that influence crystallization, *e.g.*, heating rate and annealing temperature. In monitoring the main ASW band and the remaining CO₂ and N₂O IR signatures, it is clear that the release of any trapped molecules occurs during the conversion from ASW to cubic ice (Figure 4.5).

A plausible process by which gases are trapped has been discussed by Ayotte and coworkers [23]. They suggest that some of the molecules deposited onto the ASW film enter pores that open to the vacuum, and two things happen simultaneously when the film temperature is raised. The desorption rate of molecules accumulated within these pores rises, due to the temperature increase, while the ASW film undergoes a slight molecular rearrangement. This rearrangement closes avenues of connectivity to the vacuum possessed by some pores and, thus, traps molecules that

have yet to desorb from the film interior. These trapped molecules remain enclosed in the film until ASW crystallization when the rearrangement required for the phase transition allows these molecules to escape.

The apparent saturation in the integrated absorbance of the residual band intensity for a specific ASW film (Figures 4.5 and 4.11) can be accounted for with such a model. Once the favorable sites within the film become populated, additional molecules localize on the film surface. If CO₂ and N₂O film formation does not drastically influence the desorption rate of molecules residing within the ASW, then isothermal desorption at a specific temperature will result in the trapping of approximately the same amount of molecules when *all* the available interior sites are populated. The assumption that both the desorption rate from ASW cavities and the rate of ASW film pore closure depend on temperature forms the basis of this inference. As stated earlier, the inability to calibrate CO₂ and N₂O coverage via TPD precluded a determination of CO₂ and N₂O concentrations from integrated absorbances. However, an estimate of 100 H₂O molecules for each trapped CO₂ molecule was obtained by using the integrated absorption cross section per molecule of the CO₂ ν_3 stretch in CO₂ films [31], and assuming an ASW density and layer thickness of 0.9 g/cm³ and 4 Å, respectively.

There is evidence of structural rearrangement in ASW films induced by annealing at temperatures well below that of the amorphous to cubic ice transition. Manca and coworkers [32] reported ASW reorganization commencing at 105 K, and Kimmel and coworkers [3] demonstrated that the thermal history of an ASW film

influences its porosity. It was anticipated that these structural changes would lead to a decrease in the amount of trapped CO₂ and N₂O. To verify this, ASW films were annealed to 110-130 K for 15 minutes and then cooled to 90 K prior to CO₂ or N₂O deposition. The CO₂ and N₂O that remained after isothermal desorption was far less than the amount trapped by films that were not annealed in this manner (Figure 4.14). Thus, the 110-130 K annealing of ASW films deposited at 90 K results in structural rearrangements that influence the trapping of small molecules. It is noteworthy that this happens even though the ASW spectral signature undergoes no discernible change (Figure 4.14). Presumably these rearrangements are associated with collapsing pores that are responsible for trapping molecules. As mentioned earlier, crystalline films failed to trap a detectable amount of deposited molecules, consistent with the fact that these films lack significant porosity.

The presence of CO₂ and N₂O within the ASW film does not necessarily bring about a shift in the *d*-OH feature. As Figure 4.13 shows, this band remains unaffected by relatively small N₂O accumulations within the film. However, increasing the amount of deposited N₂O eventually leads to a 50 cm⁻¹ red shift in the *d*-OH peak position.

Brunauer-Emmett-Teller (BET) isotherms have been used to determine adsorption energies of molecules interacting with ice films [29]. These studies report no correlation between *d*-OH band shifts and heats of adsorption. Though no inferences are made here about interaction strength between ice and CO₂ or N₂O, recent theoretical efforts have been directed at determining parameters responsible

for shifts of the *d*-OH group [16]. Thus, the data presented here provide grist for the mill of theory.

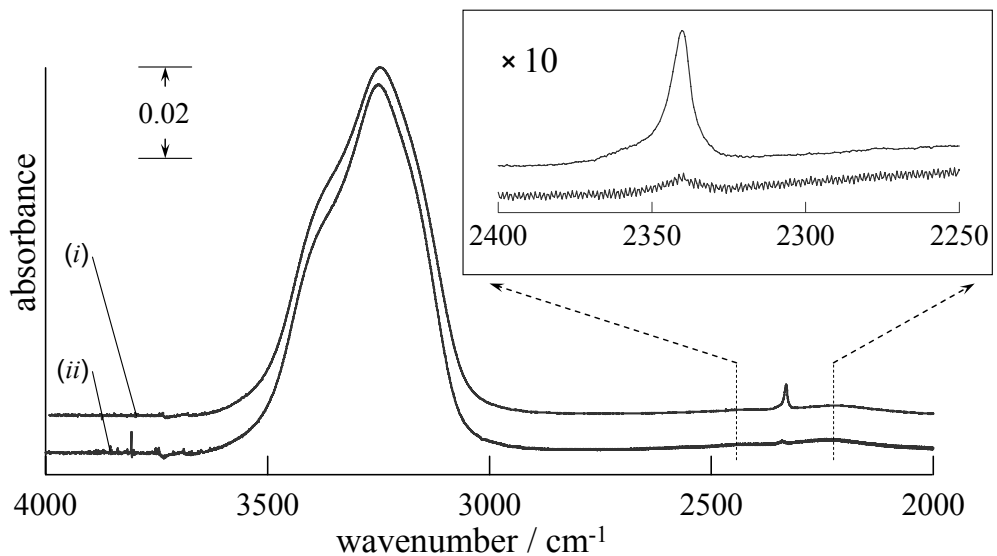


Figure 4.14. 90 K ASW films of approximately the same thickness were exposed to 4×10^{-8} Torr of CO_2 for the same duration (3 min). After CO_2 deposition, the temperature was increased to 105 K and held there while a spectrum was recorded. Traces are the spectra recorded for (i) a film that was not annealed prior to CO_2 exposure and (ii) a film that was annealed for 15–20 min at 120 K and then re-cooled to 90 K prior to CO_2 exposure. The inset shows these spectra on an expanded horizontal scale with the corresponding absorbance magnification.

Molecular layers sandwiched between *non-porous* ASW films have been used as barriers to H_2O inter-film mixing during thermal annealing [33]. In such studies, the sandwiched molecular layer is believed to remain as deposited until the ASW phase transition. During this transition, the molecules in this layer escape via pathways

created in the transforming ASW. Thus, up until the aforementioned transition, these sandwiched layers are expected to physically separate non-porous ASW films.

However, by all indications, the 90 K ASW films prepared in this dissertation work are porous. The IR features of sandwiched CO₂ and N₂O films change markedly once the sandwich is annealed past 100 K, which is the sublimation temperature for these species; most noticeably, the integrated absorbance of these IR features decreases indicating that some these species escape from the sandwich structure. Moreover, the spectral feature of the remaining CO₂ and N₂O molecules suggest these molecules are located within the ASW bulk, *i.e.*, these molecules display the same IR signatures as guests molecules that enter via transport from the surface into the ASW bulk (*c.f.*, Figures. 4.9 and 4.12). Together these observations make it unlikely that the remaining CO₂ or N₂O molecules hinder diffusion between *porous* ASW films.

4.6 Summary

The experimental study described in this chapter has explored issues of porosity, uptake, and transport in ASW films. The probe molecules CO₂ and N₂O provide IR spectral signatures that enable the distinction between their surface films and their bulk inclusions in ASW hosts, including nuances such as binding to dangling OH sites. Good sensitivity is achieved because CO₂ and N₂O have strong ν_3 absorptions and relatively narrow spectral features, *e.g.*, compared to those of the ASW host. The conclusions listed below constitute a qualitative picture of the associated phenomena.

- (1) The ASW films grown at the deposition conditions used in the experiments reported herein are porous, *i.e.*, ASW films grown at 90 K can be porous. The CO₂ and N₂O guest molecules move throughout the bulk until essentially all of the adsorption sites are occupied.
- (2) When the temperature of a porous ASW film is increased from its deposition temperature of 90 K to temperatures in the range 110-130 K, the porosity changes dramatically. If the sample thus annealed is then cooled to 90 K, it traps much less CO₂ or N₂O than freshly grown 90 K samples, *i.e.*, samples that have not been annealed. It is interesting that this annealing brings about no discernible change in the ASW spectral feature centered at $\sim 3250\text{ cm}^{-1}$.
- (3) Guest molecules trapped within ASW films remain there as the temperature is increased from 90 K to 155 K. Thereafter, the ASW to cubic ice transition occurs and these guest molecules are expelled. Once the ice film is crystalline, it is no longer possible for it to take up the guest molecules within the film.
- (4) Large inclusion regions can be prepared by using sandwiched films at 90 K: ASW-guest-ASW and so forth. Raising the temperature to 105 K drives off most of the guest molecules, though guest molecules are left behind that are included in the bulk. These display the same spectral signature as guest molecules that enter via transport from the surface into the bulk.
- (5) Dangling OH bonds can be detected. Their spectral feature is sharp relative to that of the ASW film, as they are not hydrogen bonded. Guest molecules interact

with these sites, resulting in a 50 cm^{-1} red shift. This is reminiscent of gas phase studies of hydrogen-bonded dimers, where such effects are common.

4.7 Chapter 4 References

- [1] K. P. Stevenson, G. A. Kimmel, Z. Dohnalek, R. S. Smith and B. D. Kay, *Science*, 283, 1505, (1999).
- [2] P. Jenniskens and D. F. Blake, *Science*, 265, 753, (1994).
- [3] R. Pletzer and E. Meyer, *Journal of Chemical Physics*, 90, 5207, (1989).
- [4] C. Manca, C. Martin and P. Roubin, *Chemical Physics Letters*, 364, 220, (2002).
- [5] G. A. Kimmel, K. P. Stevenson, Z. Dohnalek, R. S. Smith and B. D. Kay, *Journal of Chemical Physics*, 114, 5284, (2001).
- [6] A. Givan, A. Loewenschuss and C. J. Nielson, *Journal of Physical Chemistry B*, 101, 8696, (1997).
- [7] L. Schriver-Mazzuoli, A. Schriver and A. Hallou, *Journal of Molecular Structure*, 554, 289, (2000).
- [8] B. Roland and J. P. Devlin, *Journal of Chemical Physics*, 94, 812, (1991).
- [9] A. Allouche, P. Verlaque and J. Pourcin, *Journal of Physical Chemistry B*, 102, 89, (1998).
- [10] M. E. Palumbo, *Journal of Physical Chemistry A*, 101, 4298, (1997).
- [11] T. Takoaka, M. Inamura, S. Yanagimachi, I. Kusunoki and T. Komeda, *Journal of Chemical Physics*, 121, 1 September 2004, (2004).
- [12] S. C. Silva and J. P. Devlin, *Journal of Physical Chemistry*, 98, 10847, (1994).
- [13] V. Buch, L. Delzeit, C. Blackledge and J. P. Devlin, *Journal of Chemical Physics*, 100, 3732, (1996).
- [14] S. A. Sandford and L. J. Allamandola, *Journal of Astrophysics*, 355, 357, (1990).
- [15] P. U. Andersson, M. B. Nagard, G. Witt and J. B. C. Pettersson, *Journal of Physical Chemistry A*, 108, 4627, (2004).
- [16] C. Manca and A. Allouche, *Journal of Chemical Physics*, 114, 4226, (2001).

- [17] S. Hawkins, G. Kumi, S. Malyk, H. Reisler and C. Wittig, *Chemical Physics Letters*, *404*, 19, (2004).
- [18] G. A. Somorjai, *Introduction to Surface Chemistry and Catalysis*, John Wiley and Sons, Inc: New York, 1994.
- [19] R. S. Smith and B. D. Kay, *Surface Review and Letters*, *4*, 781, (1997).
- [20] D. Ferry, A. Glebov, V. Senz, J. Suzzane, J. P. Toennies and H. Weiss, *Journal of Chemical Physics*, *105*, 1697, (1996).
- [21] G. Herzberg, *Infrared and Raman Spectra*, Van Nostrand Reinhold Company, Inc: New York, 1945.
- [22] M. A. Ovchinnikov and C. A. Wight, *Journal of Chemical Physics*, *99*, 3374, (1993).
- [23] P. Ayotte, R. S. Smith, K. P. Stevenson, Z. Dohnalek, G. A. Kimmel and B. D. Kay, *Journal of Geophysical Research*, *106*, 33837, (2001).
- [24] J. P. Devlin, *Journal of Physical Chemistry*, *96*, 6185, (1992).
- [25] J. Heidberg and B. Redlich, *Surface Science*, *368*, 140, (1996).
- [26] J. Heidberg, B. Redlich and D. Wetter, *Berichte Bunsenges Physical Chemistry*, *99*, 1333, (1995).
- [27] O. Berg and G. E. Ewing, *Surface Science*, *220*, 207, (1989).
- [28] H. Chang, H. H. Richardson and G. E. Ewing, *Journal of Chemical Physics*, *89*, 7561, (1988).
- [29] C. Martin, C. Manca and P. Roubin, *Surface Science*, *502-503*, 275, (2002).
- [30] A. Bar-Nun, J. Dror, E. Kochavi and D. Laufer, *Physical Review B*, *35*, 2427, (1987).
- [31] H. Yamada and W. B. Person, *Journal of Chemical Physics*, *41*, 2478, (1964).
- [32] C. Manca, C. Martin and P. Roubin, *Chemical Physics*, *300*, 53, (2004).
- [33] S. M. McClure, E. T. Barlow, M. C. Akin, D. J. Safarik, T. M. Truskett and C. B. Mullins, *Journal of Physical Chemistry B*, *110*, 17987, (2006).

Chapter 5: The Nature of Trapping Sites in Ice

5.1 Introduction

Amorphous solid water (ASW) films are capable of influencing the desorption characteristics of certain molecules deposited onto their surfaces or co-condensed during their formation [1-4]. Moreover, most of the experimental results are consistent with the idea that thermally induced structural changes in these films play a major role in the aforementioned desorption process. In particular, these structural changes trap molecules residing within ASW, and they inhibit the release of these molecules until ASW crystallization and the sublimation of the crystallized ice. But what are these structural relaxations and where do they occur, *i.e.*, throughout the film or localized to certain layers? Several groups [5-9] have observed that some of these trapped species are retained within crystalline ice after the phase transition. However, there are only speculations as to how or why this happens, and this is because the processes occurring during this phase transition are poorly understood. Indeed, the very nature of ice at the phase transition is in itself a source of controversy.

ASW is often described as a glassy state of water, and implicit in such a description is the suggestion that liquid water can be supercooled suitably enough to induce a glass transition [10, 11]. Determining this glass transition, a key step in establishing this relationship, has been hampered by the experimental difficulty of probing liquid water's properties in the temperature range of 160-230 K. On one hand, it is difficult to inhibit the crystallization of supercooled water at ~ 230 K, and

on the other, amorphous ice readily crystallizes at ~ 160 K. Thus, what emerges is an experimentally inaccessible region, the so-called "no man's land" [12] that makes the nature of supercooled water below ~ 230 K controversial.

There are reports suggesting amorphous ice undergoes a glass transition to supercooled water at ~ 140 K, prior to crystallizing at ~ 160 K [13-16]. In this case, rather than transforming glassy water to crystalline ice, the phase transition transforms supercooled water to crystalline ice. In contrast, there are reports also that suggest the glass transition temperature (T_g) is greater than ~ 160 K [1, 9, 11, 17], and this implies that observing the glass transition is prevented simply by the fact takes place in an experimentally inaccessible region.

If the glass transition does indeed occur before the phase transition, the question then turns to the nature of the supercooled liquid formed by the glass transition. Fragility is a term used to characterize the temperature dependence of relaxation processes in liquids; the viscosity of a fragile liquid displays a non-Arrhenius dependence on temperature, and a fragile liquid becomes very fluidic, relative to its glassy state, in a short temperature range above T_g [10]. Recent thermal desorption studies have interpreted inter-mixing in isotopically labeled ASW films (grown one atop the other) at ~ 150 K as bulk diffusion [13, 14], and this led to the conclusion that ASW behaves as a fragile liquid above ~ 140 K. However, subsequent studies argue that this inter-mixing is a result of H_2O transport through the interconnected network of fractures created *during* crystallization and that this process is distinctly different from bulk diffusion [9, 17].

While the details about the molecular rearrangements accompanying ASW crystallization are important, obtaining these details has been difficult. Instead, investigations have settled for a more practical goal; a microscopic description of these dynamics [18-20]. The work detailed in this chapter takes this same approach, and it focuses on the ASW crystallization dynamics by exploring how these dynamics influence the release of trapped species. Specifically, this study examines what factors (ASW film thickness, deposition technique, annealing rate, *etc.*) affect the ratio of trapped CO₂ molecules that escape during crystallization to those that are retained within ice. This knowledge will support rationalizations, consistent with the observed experimental results, about likely processes occurring during crystallization. Moreover, the IR spectroscopy of these trapped species will also provide valuable insight into the nature of the local environment surrounding these species.

Using a combination of TPD and IR experiments, two independent but complementary means are used to explore differences in the properties of the trapped species (aside from their differing desorption temperature). These results show that thermal desorption experiments without accompanying IR experiments may lead to erroneous conclusions about obtained results. As detailed in the previous chapter, CO₂ is well-suited for these types of IR studies.

5.2 Experimental

The experiments were performed in the UHV chamber described in chapter 3 of this dissertation. The MgO (100) substrate was prepared by cleaving an MgO crystal in dry nitrogen. This substrate was inserted into the chamber, and then cleaned using an established procedure. TPD studies were performed using a Stanford Research Systems residual gas analyzer (SRS RGA 300). A stainless steel cone with a small (~9 mm) aperture was used to screen out molecules not originating from the surface during TPD.

The substrate was attached to a manipulator, which provided XYZ translation and 360° rotation of the substrate, using a surface holder. Unless explicitly stated, the surface holder used for these experiments is one that allowed IR and TPD experiments to be performed using the same holder; this surface holder design is detailed in chapter 3 (see Figure 3.7). For this holder, the lowest temperature attainable was typically ~90 K. This was achieved by bubbling helium gas through a filled liquid nitrogen reservoir which was in contact (thermally) with the surface holder. The surface could be heated to a temperature of ~500 K using a homemade heater, and this temperature was monitored by a *k*-type thermocouple adhered to the surface.

FTIR experiments were carried out with a commercial spectrometer (Nicolet Protégé 460), and the IR beam was directed in and out of the chamber using mirrors. H₂O (distilled and purified by osmosis) was degassed by several freeze-pump-thaw

cycles, and CO₂ (Glimore 99.99%) was used without further purification. These gases were introduced into the chamber using separate leak valves.

5.3 Results

The formation of a CO₂ film at 90 K on MgO (100) yields a *p*-polarized IR spectrum with distinctive LO and TO features. The TPD trace of such a film exhibits one desorption feature at ~105 K (Figure 5.1), and this suggests there is little difference in the binding energies of the CO₂ monolayer (*i.e.*, CO₂ molecules in contact with the MgO surface) and multilayers. This is in contrast to a CO₂/MgO(100) study by Heidberg and others [21] in which a CO₂ monolayer was

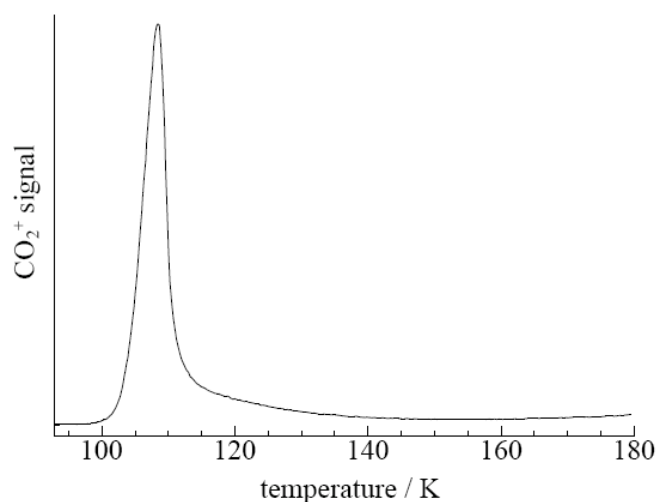


Figure 5.1. A TPD trace of a CO₂ film prepared at 90 K on MgO(100). The TPD experiment was performed by heating the surface at ~1 K/s and monitoring a mass-to-charge ratio (*m/e*) of 44. MgO exposure to CO₂ was carried out at a pressure 4×10^{-8} Torr for 3 min.

produced by exploiting a significant difference in the vapor pressure, and hence binding energy, of the CO₂ monolayer and the ensuing multilayers. However, it is well-known that the concentration of defect sites on the MgO(100) surface depends upon how the surface is prepared (*i.e.*, polished or unpolished, cleaved in vacuum or in nitrogen, *etc.*) [22]. Thus, it is conceivable that these apparent differences stem from different surface preparatory methods. No other TPD spectra of CO₂ desorbing from MgO(100) appear to have been reported.

In agreement with recent studies [23], the TPD traces of CO₂ deposited onto ASW consists of three desorption features (Figure 5.2). The low temperature (~105 K) peak is attributed to CO₂ multilayer and monolayer desorption from ice, while the two features at higher temperatures (>150 K) are from CO₂ molecules trapped in ASW. Some of these trapped CO₂ molecules desorb during crystallization at ~165 K, while the remaining species co-desorb with crystalline ice film. The tail at T > 180 K is a result of co-desorption from the sample holder. This was deduced by varying the sample holder position relative to the mass spectrometer aperture.

The spectral characteristics of the CO₂ molecules that are retained within crystalline ice can be explored, without interference from CO₂ released during the phase transition, by ice annealing to appropriate temperatures after CO₂ deposition. As the TPD trace in Figure 5.3 shows, annealing temperatures of 165 K are suitable for this purpose; the annealed film was re-cooled to ~90 K prior to obtaining the TPD trace. Also shown in this figure is a TPD trace of a sample prepared in the same

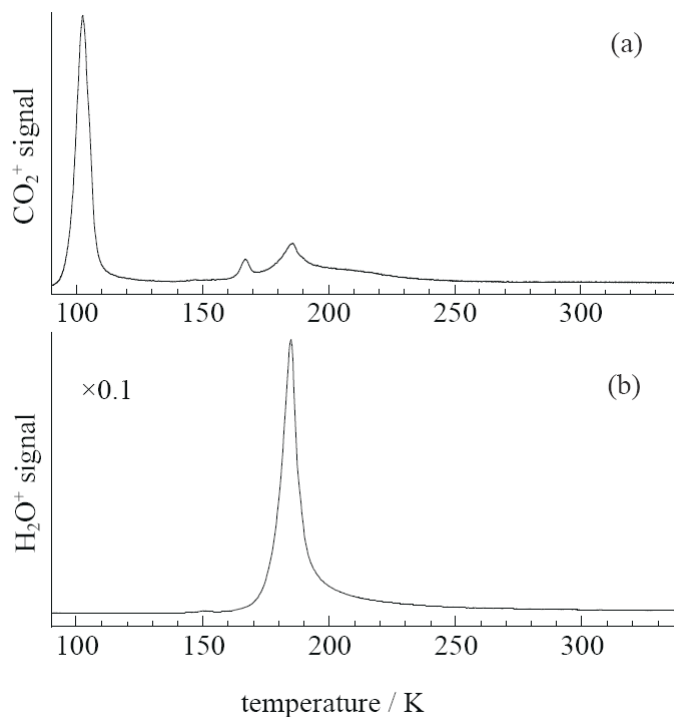


Figure 5.2. CO₂ was deposited (4×10^{-8} Torr for 3 min) onto an ASW film (5×10^{-8} Torr for 7 min) ~ 80 layers thick. The H₂O desorption was monitored by measuring m/e 18. Panels (a) and (b) show the TPD traces of CO₂ and H₂O respectively. The TPD trace of H₂O was scaled for clarity.

way (*i.e.*, same ASW thickness, deposited CO₂, *etc.*) but annealed to ~ 105 K. The IR spectra of these two samples (Figure 5.4), recorded after they had been re-cooled to 90 K and before obtaining the aforementioned TPD traces, suggests that CO₂ molecules that remain in crystalline ice possess significantly smaller oscillator strengths than the CO₂ molecules escaping during the phase transition. Indeed, for these samples, there is no distinguishable IR feature for the former species (Figure 5.4), in spite of the TPD data suggesting there are more of these species than that of the latter (Figure 5.3).

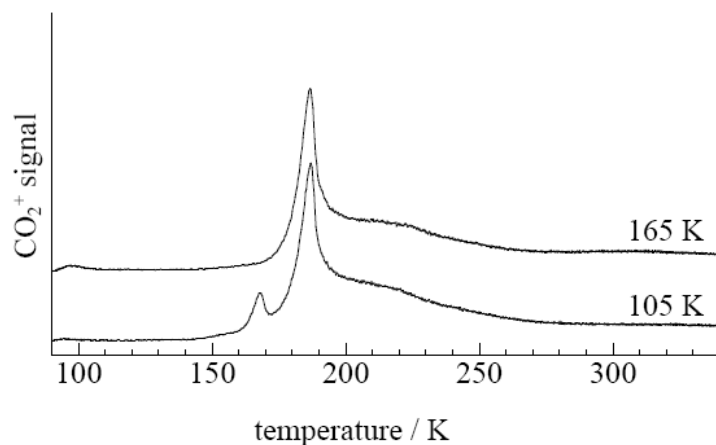


Figure 5.3. TPD traces of CO_2 (4×10^{-8} Torr for 3 min) deposited onto ASW films (~ 80 layers). The temperature to which each sample was annealed prior to recording FTIR spectrum is indicated. As the traces show, the CO_2 TPD feature at 185 K was not affected by the annealing to 105 K.

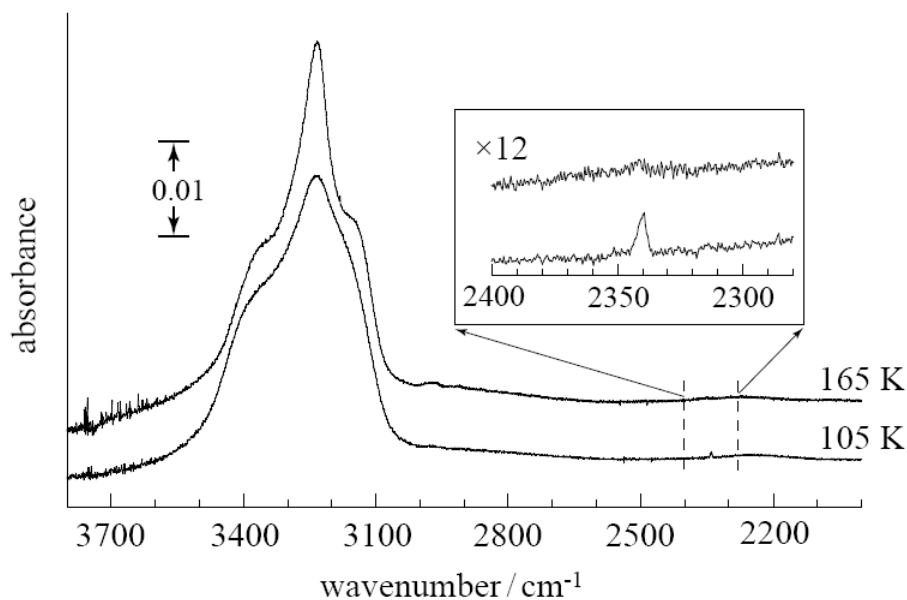


Figure 5.4. Spectra (*p*-polarized) of ASW films (~ 80 layers) exposed to CO_2 (4×10^{-8} Torr for 3 min). Each sample was annealed to the temperature indicated and then re-cooled to 90 K. The broad H_2O feature ($\sim 3250 \text{ cm}^{-1}$) changes upon annealing past 165 K because of the ASW-to-cubic phase transition. The inset shows the expanded scale of the CO_2 ν_3 band absorbance region with the corresponding magnification factor.

5.4 Discussion

Morphological changes in porous ASW films can be induced thermally, and molecules that have to desorb by diffusing through ASW as these changes take place can become trapped within ASW. There are three ways to create a situation whereby a species has to diffuse through ASW to desorb. One procedure involves co-condensing H₂O and another gas at low temperatures (less than 100 K) to form a solid film with two different molecular species. Another method is to form an ASW film on top of a solid film comprised of a different molecular species. Finally, molecules can be deposited onto ASW at temperatures where they can adsorb into the ASW surface but are able to diffuse relatively freely on this surface. These molecules diffuse into ASW and have to make their way out of this ASW to desorb. For each of these methods, the amount of guest molecules trapped within the film depends on a set of factors unique to the method. For example, the composition of the gas mixture and the deposition temperature influence the composition of the solid film formed by co-condensing ASW and another gas species. In turn, this influences the quantity of guest molecules that are subsequently trapped by annealing the film.

Some of these trapped molecules escape during the crystallization, and the general consensus is that these molecules reside within ASW pores. However, the location and nature of the molecules that are not released during this transition have been a source of speculation. Initial considerations suggested these molecules may be part of CO₂ clathrate hydrate domains within ice; whether these domains are created during crystallization or they exist even before this process is not something

that has been addressed. While the IR signatures of CO₂ molecules in hydrates have been reported, the relative absorption strengths of these CO₂ molecules compared to CO₂ molecules in a CO₂ film appear to be unknown [24]. Thus, it is unclear if the lack of a discernible IR feature stems from the fact that these are CO₂ molecules in a clathrate hydrate, and if in these structures the absorption strength of CO₂ is severely attenuated (relative to other CO₂ molecules in ice). Nevertheless, studies indicate that CO₂ does not form clathrate hydrates readily at low pressures [24, 25]. As a result, it is very unlikely that CO₂ molecules co-desorbing with H₂O are from CO₂ hydrate structures within ice.

There are two likely explanations as to why CO₂ molecules that co-desorb with crystalline ice exhibit no discernible IR feature. The oscillator strength of the two trapped species (*i.e.*, those that escape during crystallization and those that do not) could be truly different, and this suggests that the immediate surroundings for these species are dissimilar. However, it is also possible that the CO₂ molecules responsible for the TPD peak at ~185 K do not originate from the surface and that is why they exhibit no IR feature. Investigations with a similar but different molecule, specifically a CO₂ isotopologue (¹³CO₂), are currently underway to determine which of the two scenarios is more likely.

If a distinguishable IR feature for ¹³CO₂ trapped in crystalline ice is observed, this would indicate that the ¹²CO₂ molecules detected in the ¹²CO₂ TPD trace (see Figure 5.3) do not originate from the surface. It is improbable that IR features of CO₂ are influenced strongly by the surrounding H₂O molecules while the IR features of

$^{13}\text{CO}_2$ are not. An IR or TPD feature that can be ascribed to molecules retained within crystalline ice will be used to explore whether these molecules are distributed throughout the crystalline bulk, *i.e.*, whether the intensity of this feature scales with film thickness. Moreover, a comparison of the IR features from these two sets of trapped species (*i.e.*, those that escape during crystallization and those that do not) will yield insight into the similarity, or dissimilarity, in the environment surrounding these two groups. For example, it is possible that not all the ice crystallizes and that it is ASW domains imbedded within the polycrystalline ice film that host the guest molecules co-desorbing with the crystalline ice film. Finally, the factors that mediate the ratio of the molecules released during the phase transition to molecules retained within crystalline ice will be investigated by exploring how this ratio varies with deposition technique (co-dosing or depositing CO_2 atop ASW films), film thickness, and annealing rate. The last factor listed influences the crystallization kinetics and which, in turn, may be a mediating factor with regards to the amount of molecules released during the phase transition.

5.5 Epilogue

The aforementioned $^{13}\text{CO}_2$ studies were completed during the process of writing this dissertation. $^{13}\text{CO}_2$ was deposited onto ASW films (~80 layers thick), and the absence of a $^{13}\text{CO}_2$ ν_3 IR feature after the phase transition agreed with the CO_2 results described in this chapter. However, the TPD for the $^{13}\text{CO}_2$ isotopologue revealed no $^{13}\text{CO}_2$ molecules desorbing with the cubic ice film, and this was

consistent with the $^{13}\text{CO}_2$ IR results. This suggests that the CO_2 TPD signal (*i.e.*, *m/e* 44) observed during desorption of the H_2O film does not originate from CO_2 molecules trapped in ice. The source of this CO_2 is currently unclear.

Experiments with thicker (> 80 layers) ASW films show that the thicker the ASW film, the larger the amount of $^{13}\text{CO}_2$ molecules that co-desorbs with the cubic ice film; this is true when all factors except ASW film thickness are kept constant. Moreover, the IR signatures for molecules released during the phase transition and molecules retained within cubic ice are similar. Based on this similarity, it is concluded that there is little difference in the local environments for these two sets of molecules. Most likely, both groups consist of molecules trapped in pores within ice, be it ASW or cubic ice.

5.6 Chapter 5 References

- [1] J. A. Ghormley, *Journal of Chemical Physics*, *46*, 1321, (1967).
- [2] A. Barnun, J. Dror, E. Kochavi, D. Laufer, D. Kovetz and T. Owen, *Origins of Life and Evolution of the Biosphere*, *16*, 220, (1986).
- [3] G. A. Kimmel, K. P. Stevenson, Z. Dohnalek, R. S. Smith and B. D. Kay, *J. Chem. Phys.*, *114*, 5284, (2001).
- [4] P. Ayotte, R. S. Smith, K. P. Stevenson, Z. Dohnalek, G. A. Kimmel and B. D. Kay, *Journal of Geophysical Research-Planets*, *106*, 33387, (2001).
- [5] J. E. Schaff and J. T. Roberts, *Langmuir*, *14*, 1478, (1998).
- [6] M. P. Collings, M. A. Anderson, R. Chen, J. W. Dever, S. Viti, D. A. Williams and M. R. S. McCoustra, *Monthly Notices of the Royal Astronomical Society*, *354*, 1133, (2004).
- [7] J. D. Graham, J. T. Roberts, L. A. Brown and V. Vaida, *Journal of Physical Chemistry*, *100*, 3115, (1996).
- [8] R. L. Hudson and B. Donn, *Icarus*, *94*, 326, (1991).
- [9] S. M. McClure, E. T. Barlow, M. C. Akin, D. J. Safarik, T. M. Truskett and C. B. Mullins, *Journal of Physical Chemistry B*, *110*, 17987, (2006).
- [10] C. A. Angell, *Science*, *267*, 1924, (1995).
- [11] C. A. Angell, *Annual Review of Physical Chemistry*, *55*, 559, (2004).
- [12] O. Mishima and H. E. Stanley, *Nature*, *396*, 329, (1998).
- [13] R. S. Smith, Z. Dohnalek, G. A. Kimmel, K. P. Stevenson and B. D. Kay, *Chemical Physics*, *258*, 291, (2000).
- [14] R. S. Smith and B. D. Kay, *Nature*, *398*, 788, (1999).
- [15] G. P. Johari, A. Hallbrucker and E. Mayer, *Nature*, *330*, 552, (1987).
- [16] S. Bahr, A. Borodin, O. Hofft, V. Kempter, A. Allouche, F. Borget and T. Chiavassao, *Journal of Physical Chemistry B*, *110*, 8649, (2006).

- [17] S. M. McClure, D. J. Safarik, T. M. Truskett and C. B. Mullins, *Journal of Physical Chemistry B*, *110*, 11033, (2006).
- [18] R. S. Smith, C. Huang, E. K. L. Wong and B. D. Kay, *Surface Science*, *367*, L13, (1996).
- [19] R. S. Smith, C. Huang and B. D. Kay, *Journal of Physical Chemistry B*, *101*, 6123, (1997).
- [20] S. Mitlin and K. T. Leung, *Canadian Journal of Chemistry-Revue Canadienne De Chimie*, *82*, 978, (2004).
- [21] J. Heidberg and B. Redlich, *Surface Science*, *368*, 140, (1996).
- [22] S. A. Hawkins: *Fourier transform infrared spectroscopy and temperature programmed desorption of water thin films on the MgO (100) surface*, Ph. D. Thesis, Department of Chemistry, University of Southern California, Los Angeles, 2004.
- [23] M. P. Collings, J. W. Dever, H. J. Fraser and M. R. S. McCoustra, *Astrophysics and Space Science*, *285*, 633, (2003).
- [24] F. Fleyfel and J. P. Devlin, *Journal of Physical Chemistry*, *95*, 3811, (1991).
- [25] G. Notesco and A. Bar-Nun, *Icarus*, *148*, 456, (2000).

Chapter 6: Future Experiments

6.1 Amorphous Materials

An amorphous material, in the popular and essentially correct conception, is a solid that possess no long range order with respect to the position of its constituents. This relatively loose description allows a plethora of materials to be catalogued as amorphous materials, and it sidesteps the current confusion in the literature concerning the distinction between a glass and an amorphous material; there is a tendency to use these two terms interchangeably, but some argue that this is incorrect [1, 2]. Amorphous materials are not new. The manufacture of glassy materials from silica commenced thousands of years ago. What is new is the increased interest in these substances as novel materials, produced in amorphous form, have become technologically important [1, 3-5]. In particular, there has been increased focus on the fundamental processes that occur within such systems [3, 6-8]. In attempts to predict the glass transition of various amorphous materials, these studies are addressing why and how glasses form.

Amorphous ice has been a model system for studying amorphous materials [9-11]. It is easily prepared, relatively free of contaminants, in simplified environments (ultrahigh vacuum), and structural changes in this amorphous state can be monitored using small probe molecules [12-15]. Experiments using this amorphous system have supported the current consensus that the structure of all amorphous materials depends upon formation conditions, and they have revealed that even at temperatures well-below (~50 K) known phase transition temperatures, amorphous materials can

undergo molecular rearrangements [13]. In turn, these rearrangements influence the molecular transport through this phase.

How can this system be modified to provide even more subtle details about amorphous materials? One strategy is to introduce spatial heterogeneities into an amorphous solid water (ASW) film in a controlled fashion, and then to examine how these induced effects modify the characteristics of the system. The rationale behind such a strategy is easy to comprehend. The amorphous state is influenced by its immediate surroundings, and to examine this influence, these surroundings should be altered in a systematic way. For example, the creation of boundaries within an amorphous system enhances the participation of these entities in processes occurring within the system. This approach is akin to that in which ice nanocrystals were created to enhance the ratio of surface to bulk H₂O molecules (relative to that in an H₂O film) [16-18]. In those investigations, this enhanced ratio allowed surface effects to be more easily distinguished.

6.2 Amorphous Ice: Transport and the Amorphous-Crystalline Interface

The creation of domains of crystalline ice distributed, essentially in a homogenous fashion, throughout an ASW film would constitute a novel model system from which additional information about amorphous materials may be obtained (Figure 6.1). An ASW film annealed to ~130 K appears nonporous when examined by probe molecules deposited onto the ASW surface. That said, it is important to bear in mind that this lack of porosity may not pervade throughout the

film. Morphological changes restricted to the first few film layers can in principle limit the accessibility of probe molecules, deposited on ASW, to pores located within the ASW interior. It has been suggested that during crystallization fractures are created as the more compact crystalline ice phase "shrinks" away from the surrounding ASW [19-21]. Thus, it is anticipated that creating crystalline domains within a relatively nonporous ASW film will create fractures (or voids), and the presence of these crevices will make the film porous. This porosity can be examined using probe molecules, and it would be of interest to determine if the anticipated results are realized.

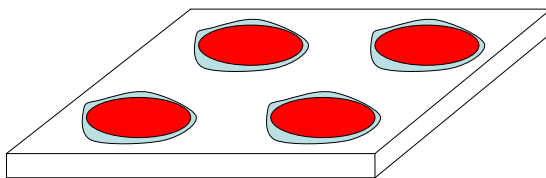


Figure 6.1. An ASW film with domains of crystalline ice (shown in red) may possess cracks or voids (shown in blue) at the amorphous-crystalline interface.

It would be constructive also to examine the crystallization dynamics of this novel system, *i.e.*, domains of crystalline ice embedded within ASW. Appropriate annealing temperatures can be selected such that the process of ASW crystallization occurs over minutes, and this process can be monitored using the IR spectra of ice or probe molecules [14, 21-23]. In these isothermal experiments, heat is supplied through the supporting substrate, *i.e.*, supporting the film. Thin (~15 layers) ASW

films deposited onto crystalline ice exhibit dramatic increases in their crystallization rate relative to films deposited onto a Pt(111) substrate. For example, it takes ~1000 seconds for a 15 layer ASW film deposited on Pt(111) to be half way to complete crystallization at ~140 K. In contrast, a film of the same thickness formed on crystalline ice is half crystallized in ~30 seconds at the same temperature. This result is interpreted as a "seeding" effect in which the underlying crystalline ice film obviates the need for a nucleation step to initiate crystallization [23]. Within the semiconductor industry, it is known that substrate-induced crystallization can be used to lower the crystallization temperature of a film [24]. Hence, it is expected that an "ASW-crystalline ice array" (Figure 6.1) crystallizes over a shorter time scale than a regular ASW film (containing the same amount of ASW that is in the array). Indeed, it may be possible to find a temperature where these samples crystallize on very different time scales, *e.g.*, one in minutes and the other in hours.

The preceding discussion concentrated on a system comprising of crystalline ice domains within ASW, and it addressed specifically the crystallization process. A system in which isolated regions of ASW are formed on a supporting substrate represents another novel system from which many subtleties about transport and flow in amorphous materials may be gleaned (Figure 6.2). Based on the stability of ASW films at temperatures less than 100 K (see chapter 4), it is anticipated that these ASW regions of $\sim 50 \mu\text{m} \times 50 \mu\text{m}$ will be stable for several hours. But what occurs as the substrate is heated slowly? If the glass transition of amorphous ice does indeed occur prior to the phase transition *and* supercooled water in this temperature range is

a fragile liquid, then the voids surrounding these ASW "patches" may be filled as H₂O molecules diffuse into this region (Figure 6.2). Presumably, it is the fluidic nature a fragile liquid exhibits at temperatures above its glass transition that would permit such lateral mobility and changes in the system's boundary.

An amorphous ice film retains trapped species up until the phase transition [14, 25]. Consequently, *if* there is a glass transition before the phase transition, these trapped species do not escape during the first process. However, it is unclear if this would be the case still if the supercooled liquid formed during the glass transition commences to flow. Naturally, this depends upon the dynamics of the flow process. These molecules may be carried along, or they may be able to escape because of the mechanism by which the molecular transport occurs. A priori, the outcome is not apparent. And yet it is an outcome that has important implications for how molecular transport in amorphous materials takes place just above the phase transition temperature.

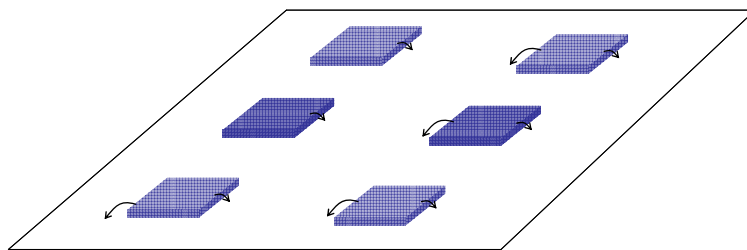


Figure 6.2. The slabs (shown in blue) represent isolated regions of ASW on a supporting substrate. As these isolated regions approach the phase transition temperature, there may be a significant increase in lateral mobility (indicated by the black arrows) and material may be transported to the surrounding regions.

6.3 Experimental Strategy

An approach to obtaining new insights into the crystallization dynamics and molecular transport in ice has been described. What has yet to be discussed is how the samples needed for such an endeavor can be created. Specifically, this issue concerns the introduction of morphological changes into an ASW film in a selective and controlled manner.

The proposed experimental strategy is to fabricate such samples by pulsed laser irradiation of ASW films through fine meshes with apertures of $\sim 50 \mu\text{m} \times 50 \mu\text{m}$. The wavelength of the laser radiation is chosen such that it excites H_2O vibrations specifically, and it does not excite the substrate. The spectral width of the ASW absorption band at $\sim 3400 \text{ cm}^{-1}$ is relatively large ($\sim 300 \text{ cm}^{-1}$), and any radiation within this range will be absorbed. The details about how energy pumped into a vibrational mode of an H_2O molecule, within an ASW film, leads to film annealing are complex but qualitatively understood. Basically, energy implanted into an OH excitation stretch degrades to heat which is then transferred to the surroundings, *i.e.*, neighboring H_2O molecules and the underlying substrate (which is kept cold). As a result, once the irradiation ceases, the system cools efficiently. A similar laser heating technique has been used to desorb water from the Ru(001) surface [26-28].

The proposed process involves first forming ASW films on a MgO(100) substrate at low temperatures (less than 100 K). This substrate permits transmission IR experiments in the region of $4000\text{-}2000 \text{ cm}^{-1}$. Next, with a stainless steel mesh positioned in front of the cold sample, the sample is irradiated with a pulsed laser

beam (Figure 6.3). Depending upon the laser fluence and duration of irradiation, all H₂O behind the exposed areas of the mesh will either be desorbed, remain unchanged (*e.g.*, if the laser fluence is insufficient), or undergo morphological changes as a result of heating. Figure 6.3 depicts the situation in which all the H₂O exposed to the irradiation desorbs.

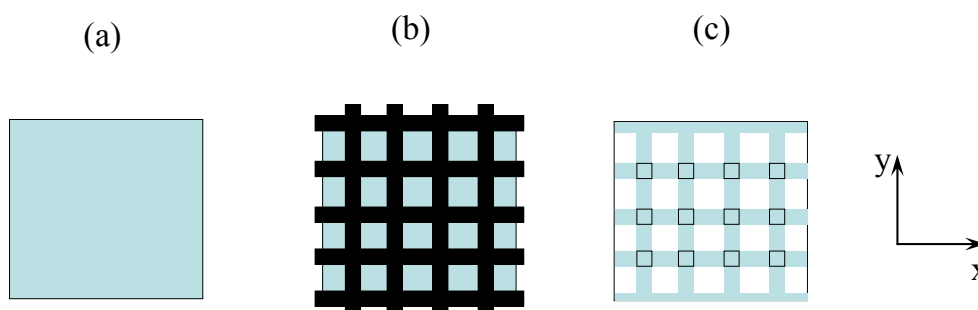


Figure 6.3. (a) An ASW film is formed on a supporting substrate. (b) A mesh (shown in black) is placed in front of the film, and the film is irradiated. (c) All the ASW in the exposed areas desorb, leaving the structure depicted in blue. To form isolated rows of ASW with the axes of the rows parallel to the y-axis shown, the mesh can be translated in small increments along the x-axis. At each increment the substrate is irradiated to desorb any exposed ASW. To form isolated areas of ASW (the black squares), this process has to be done along both axes of the mesh (shown as x and y).

Ideally, the control of the laser fluence and irradiation time would be suitable enough to vary the amount of morphological change in the irradiated areas from small (*i.e.*, in the case of a relatively small increase in local temperature) to very significant (*i.e.*, induce a phase change). In addition, this control would permit also

laser-induced desorption of H₂O. Attaining some semblance of this ideal situation will be challenging, but it may be possible. A logical approach is to examine first the effects of laser irradiation on ASW films without the mesh in place.

With regard to ASW films irradiated without a mesh in place, molecules still remaining on the surface after irradiation are expected to be cooled efficiently by the substrate once this process ceases. For the situation in which a significant amount of H₂O desorbs as a result of irradiation, a comparison of the H₂O infrared (IR) spectrum before and after irradiation should provide a good indication of this change; there will be a marked reduction in H₂O absorbance, and, most likely, the ASW IR spectrum will have transformed to that displayed by crystalline ice. The latter statement assumes the temperature within the film is relatively even. In addition to IR spectroscopy, temperature programmed desorption (TPD) can be used also to confirm desorption, and this involves the comparison of TPD spectra from two different samples, prepared in the same manner, having the same thickness. Only one sample is subjected to irradiation, and the TPD spectrum for this sample will display a decrease in the H₂O TPD intensity, relative to the other sample, if desorption occurred during the irradiation. It is also possible to place the ASW sample in front of the mass spectrometer while it is being irradiated to detect any H₂O desorption.

While there are several ways to confirm desorption, the detection of any transformations from ASW to crystalline ice without significant desorption is limited essentially to monitoring changes in the H₂O IR spectrum. These changes may be

difficult to perceive. The main IR band of both its amorphous and crystalline phases is broad, and there is a significant overlap between these two features. Nevertheless, using these two bands, it is possible to de-convolute the IR band of a H₂O film to determine the ratio of crystalline to amorphous ice.

To detect the formation of crystalline ice within the sample in a more sensitive manner, probe molecules with narrow IR features (*e.g.*, CO₂ and N₂O) can be trapped in ASW films prior to the laser irradiation. This involves forming an ASW film at low temperatures, exposing the film to a specific probe species, and then annealing the film at ~110 K to trap these molecules within the ASW film. Any regions of ASW converted to crystalline ice during laser irradiation will expel these trapped species, and the IR feature of these molecules will display a decrease, when compared to the spectrum taken prior to any laser irradiation.

Hence, a systematic variation in the irradiation parameters (fluence and duration of laser exposure) can be used to determine a suitable set of conditions over which crystalline ice is formed with little desorption. The conditions necessary to desorb an ASW film can be ascertained in a similar fashion. Morphological changes that do not result in desorption or crystallization will have to be detected using probe molecules. Specifically, such changes will have to be followed by monitoring the trapping capabilities of a film.

In this process, an ASW film of a certain thickness is created at low temperature (< 100 K), and then this film is induced to trap probe molecules deposited onto its surface by annealing to ~110 K (see chapter 4). Next, an IR and TPD spectrum of the

trapped species in this ASW sample is obtained. After desorbing this film, another ASW film of the same thickness is formed under identical conditions, but this film is then subjected to laser irradiation (for some specified laser fluence and duration). Probe molecules are deposited onto this film, and subsequently it is induced to trap some of these molecules. After this, the IR and TPD spectrum of the trapped species is recorded. A comparison of the obtained IR or TPD spectra should be sufficient to determine if laser irradiation produced any morphological changes that subsequently influenced the trapping capabilities of the ASW film.

Once a set of conditions for inducing various types of changes in an ASW film has been established, the effects of irradiation through a mesh can be explored. Ideally, the goal is to limit the induced changes to regions of the film directly behind the apertures of the mesh. However, there is the issue of thermal flow to the surrounding areas not directly behind these apertures. For openings of $50\ \mu\text{m} \times 50\ \mu\text{m}$, the area of each irradiated region in contact with the surface is $2.5 \times 10^{-3}\ \text{mm}^2$, and for a thin ($\sim 5\ \text{nm}$ thick) film the combined areas of the edges for this region (assuming a square slab shape) in contact with the surrounding H_2O is $10^{-6}\ \text{mm}^2$. Consequently, it is anticipated that most of the heat flow will be to the substrate in this situation. For thicker ($\sim 0.1\ \mu\text{m}$) films, it is unclear how much heat will flow laterally, and this effect will have to be evaluated empirically.

The binding energy of the H_2O monolayer ($\sim 0.7\ \text{eV}$) to a $\text{MgO}(100)$ substrate is significantly larger than the binding energy of the multilayers ($\sim 0.5\ \text{eV}$). In fact, this difference in binding energies is exploited to produce H_2O monolayers on this

substrate using thermal desorption [29]. Consequently, it is likely that there may be experimental conditions over which laser induced multilayer desorption occurs but the monolayer remains on the surface. Using a mesh, it may be possible to create monolayer regions of H₂O in between isolated regions of multilayer amorphous ice (Figure 6.2). A comparison of experiments from this type of arrangement to those from exactly the same arrangement but with the monolayer removed might yield insights into the diffusion dynamics of H₂O on a water monolayer as opposed to the MgO surface.

6.4 Experimental Details: the Current Configuration

The UHV chamber that will be used for these experiments was described in chapter 3 of this dissertation. Basically, it is a three-tiered chamber with a surface manipulator attached to the top tier. This manipulator allows the surface to be moved between tiers, and it provides XYZ translation and 360° rotation of the sample. The sample is cooled typically by bubbling helium gas through a liquid nitrogen reservoir.

The top tier of this chamber is used for FTIR experiments, and in these experiments optical mirrors direct the IR beam of a commercial spectrometer (Nicolet Protégé 460) in and out of the chamber using CaF₂ windows. The beam size at the surface is ~8 mm. Also, this tier can accommodate leak valves and a mass spectrometer. A mass spectrometer, fitted with a stainless steel cone having a small (~9 mm in diameter) aperture is used for TPD experiments. This cone limits the

detected desorption during TPD to species originating from the surface. A grounded stainless steel mesh (wire diameter ~ 0.025 mm, openings ~ 1.3 mm) covering the aperture of this cone prevents stray electrons leaving the mass spectrometer ionization region from reaching the adsorbate. The bottom tier of the chamber is designed to house several diagnostics simultaneously, and hence it has numerous ports.

The MgO(100) crystal substrate is prepared under dry nitrogen conditions, quickly inserted into the chamber, and cleaned following established procedure. A thermocouple, fixed to one edge of the crystal with a high temperature adhesive, records temperature. A surface holder that permits TPD and IR experiments to be performed mounts the sample onto the manipulator, and this holder allows the sample to be cooled to ~ 90 K. The surface is heated using a homemade heater attached to the surface holder, and with this heater the sample can be heated to ~ 500 K at rate of ~ 2 K/s.

Water coverage is obtained by exposing the substrate to a constant flux of water vapor for fixed time periods, and the thickness of the water films is estimated by comparing a film's integrated absorbance to that of a water monolayer on MgO(100). Probe molecules are introduced into the chamber using a separate leak valve from that used to vapor deposit water.

6.5 Experimental Details: the Modifications

None of the experiments proposed can take place without laser radiation of an appropriate wavelength (λ), *i.e.*, within the region 3.225-2.857 μm (3100-3500 cm^{-1}), and hence generating this laser light is the first logical step in attempting the proposed experiments. Laser light in this wavelength range has been produced using: an Er:YAG laser at 2.94 μm [26], an infrared free electron laser (IRFEL) at 3 μm [28], and a Nd:YAG laser (1.064 μm) coupled to a Raman cell to produce 2.93 μm light (the second Stokes line) [30]. Essentially all the components necessary for the last technique have already been acquired, and consequently, it is currently the most convenient method of choice.

However, there are issues of how much laser fluence will be necessary, and how much this technique can be expected to produce. Foster and others [30] generated 2.93 μm light by Raman shifting 1.064 μm light from a pulsed Nd:YAG (20 Hz, 8 ns pulses) using a 1 m D_2 Raman cell at 900 psi, and the power produced was $\sim 2.5 \times 10^3$ W (20 $\mu\text{J}/\text{pulse}$, 8 ns pulses). However, the Nd:YAG energy per pulse used to generate this power was not specified, and so it is unclear if this was the maximum power attainable. It is the vibrational energy spacings within D_2 (~ 3.34 μm (2990 cm^{-1})) that permits this Raman shift in wavelength.

Studies using an Er:YAG laser found that powers of $\sim 2.5 \times 10^3$ W (0.25 mJ/pulse, 100 ns pulses) focused onto a spot of ~ 200 μm in diameter were required to desorb H_2O from an ice film at 140 K [26]. A power of $\sim 1.5 \times 10^6$ W will be required to match this energy density ($\sim 6 \times 10^{10}$ W/m^2) over an area of ~ 25 mm^2 (5

mm × 5 mm), which is a suitable area for conducting the proposed experiments, and this implies ~15 mJ/pulse for a 10 ns pulse. This is less than 2 % of the maximum energy per pulse (~800 mJ/pulse, 10 ns pulses) for the 1.064 μm Nd:YAG radiation that will be used to generate the second D₂ Stokes line in the proposed experiments. Thus, it is likely that this energy requirement can be met. Because water adsorbed on surfaces effectively absorbs radiation, precautions may have to be taken to protect the optical components of the Raman shifter.

However, in the event that 15 mJ/pulse is not attained, a beam with a significantly less energy per pulse than this value can be focused tightly (*e.g.*, to a diameter ~200 μm) onto the surface, and then this beam can be translated across the film using mirrors on a piezoelectric translator. It is also plausible that this power requirement is specific to the experimental configuration used. For example, the desorption rate might have been too low to detect at power densities less than $\sim 6 \times 10^{10} \text{ W/m}^2$, and so desorption, in these situations, is low as opposed to non-existent. In addition, the proximity of a surface to the entrance of the mass spectrometer is a factor in the detection of species desorbing from the surface, and the distance separating the surface and mass spectrometer during the aforementioned Er:YAG laser experiments [26] was not specified. Hence, these issues of how much power can be generated and whether or not this power is enough must, most likely, be determined empirically.

The laser light can be introduced into the chamber through an ultraviolet grade sapphire view port positioned at one of the ports on the middle tier. The FTIR set-up

will be located on the top tier, and so the sample will have to be moved between tiers for IR experiments. However, a mass spectrometer can be placed on the middle tier to obviate the need to move between tiers for TPD experiments. To create domains of crystalline ice within an ASW film, a wire mesh can be mounted on a separate manipulator, and the ASW film can be moved behind it prior to laser radiation.

The experiments involving isolated regions of ASW on MgO(100) require a little more care with respect to the placement of the mesh. It is anticipated that the specific experimental set-up used to undertake these experiments will be an arrangement primarily based on the knowledge accrued from the experiments before it.

Experiments, with a $\sim 50 \mu\text{m} \times 50 \mu\text{m}$ mesh, have already been performed to ensure that IR spectroscopy can be carried out without moving the mesh from in front of the ASW film. The open areas of the mesh allow enough light to reach the detector, and diffraction is not an issue.

6.6 Summary

The increased interest in amorphous materials is focusing attention on the fundamental physics of such systems. In particular, amorphous ice has garnered special attention because of its applicability as a model for liquid water [9], its existence as a major component of interstellar ices [31], and its debated physical properties. In addition, it has been a model system on which to explore the physics of amorphous materials.

This chapter has outlined a strategy to modify the currently explored amorphous and crystalline ice systems to create a novel system that will provide new insights into the properties of amorphous materials. Specifically, it is about introducing spatial heterogeneities into an ASW film in a controlled fashion and probing the morphological changes and molecular transport in this amorphous material. The experiments proposed, although specific to amorphous ice, are designed to address questions germane to all amorphous systems.

6.3 Chapter 6 References

- [1] S. R. Elliot, *Physics of Amorphous Materials*, 2 ed., Longman Scientific and Technical: Essex, 1990.
- [2] R. Zallen, *The Physics of Amorphous Solids*, John Wiley and Sons, Inc.: New York, 1983.
- [3] C. A. Angell, *Science*, 267, 1924, (1995).
- [4] V. M. Fokin, E. D. Zanotto, N. S. Yuritsyn and J. W. P. Schmelzer, *Journal of Non-Crystalline Solids*, 352, 2681, (2006).
- [5] G. Frenzer and W. F. Maier, *Annual Review of Materials Research*, 36, 281, (2006).
- [6] M. Wyart, *Annales De Physique*, 30, 1, (2005).
- [7] F. H. Stillinger, *Science*, 267, 1935, (1995).
- [8] P. G. Debenedetti and F. H. Stillinger, *Nature*, 410, 259, (2001).
- [9] C. A. Angell, *Annual Review of Physical Chemistry*, 55, 559, (2004).
- [10] C. A. Angell, *Annual Review of Physical Chemistry*, 34, 593, (1983).
- [11] G. P. Johari, A. Hallbrucker and E. Mayer, *Nature*, 330, 552, (1987).
- [12] C. Manca, C. Martin and P. Roubin, *Chemical Physics*, 300, 53, (2004).
- [13] C. Martin, C. Manca and P. Roubin, *Surface Science*, 502, 275, (2002).
- [14] G. A. Kimmel, K. P. Stevenson, Z. Dohnalek, R. S. Smith and B. D. Kay, *J. Chem. Phys.*, 114, 5284, (2001).
- [15] D. Laufer, E. Kochavi and A. Barnun, *Physical Review B*, 36, 9219, (1987).
- [16] B. Rowland and J. P. Devlin, *Journal of Chemical Physics*, 94, 812, (1991).
- [17] B. Rowland, M. Fisher and J. P. Devlin, *Journal of Chemical Physics*, 95, 1378, (1991).
- [18] V. Buch, J. Sadlej, N. Aytemiz-Uras and J. P. Devlin, *J. Phys. Chem. A*, 106, 9374, (2002).

- [19] S. M. McClure, D. J. Safarik, T. M. Truskett and C. B. Mullins, *Journal of Physical Chemistry B*, *110*, 11033, (2006).
- [20] S. M. McClure, E. T. Barlow, M. C. Akin, D. J. Safarik, T. M. Truskett and C. B. Mullins, *Journal of Physical Chemistry B*, *110*, 17987, (2006).
- [21] R. S. Smith, C. Huang, E. K. L. Wong and B. D. Kay, *Physical Review Letters*, *79*, 909, (1997).
- [22] K. P. Stevenson, G. A. Kimmel, Z. Dohnalek, R. S. Smith and B. D. Kay, *Science*, *283*, 1505, (1999).
- [23] Z. Dohnalek, G. A. Kimmel, R. L. Ciolli, K. P. Stevenson, R. S. Smith and B. D. Kay, *Journal of Chemical Physics*, *112*, 5932, (2000).
- [24] C. Spinella, S. Lombardo and F. Priolo, *Journal of Applied Physics*, *84*, 5383, (1998).
- [25] G. Kumi, S. Malyk, S. Hawkins, H. Reisler and C. Wittig, *Journal of Physical Chemistry A*, *110*, 2097, (2006).
- [26] F. E. Livingston, J. A. Smith and S. M. George, *Analytical Chemistry*, *72*, 5590, (2000).
- [27] F. E. Livingston and S. M. George, *Journal of Physical Chemistry A*, *105*, 5155, (2001).
- [28] A. Krasnopoler and S. M. George, *Journal of Physical Chemistry B*, *102*, 788, (1998).
- [29] S. Hawkins, G. Kumi, S. Malyk, H. Reisler and C. Wittig, *Chemical Physics Letters*, *404*, 19, (2005).
- [30] N. S. Foster, J. E. Amonette, T. Autrey and J. T. Ho, *Sensors and Actuators B-Chemical*, *77*, 620, (2001).
- [31] E. Mayer and R. Pletzer, *Nature*, *319*, 298, (1986).

Bibliography

- [1] L. J. Allamandola, S. A. Sandford and G. J. Valero, *Icarus*, 76, 225, (1988).
- [2] A. Allouche, P. Verlaque and J. Pourcin, *Journal of Physical Chemistry B*, 102, 89, (1998).
- [3] P. U. Andersson, M. B. Nagard, G. Witt and J. B. C. Pettersson, *Journal of Physical Chemistry A*, 108, 4627, (2004).
- [4] P. U. Andersson, M. B. Nagard, G. Witt and J. B. C. Pettersson, *Journal of Physical Chemistry A*, 108, 4627, (2004).
- [5] C. A. Angell, *Annual Review of Physical Chemistry*, 34, 593, (1983).
- [6] C. A. Angell, *Science*, 267, 1924, (1995).
- [7] C. A. Angell, *Annual Review of Physical Chemistry*, 55, 559, (2004).
- [8] G. B. Arfken and H. J. Weber, *Mathematical Methods for Physicists*, Academic Press: San Deigo, 1995.
- [9] P. Atkins and R. Freidman, *Molecular Quantum Mechanics*, Oxford University Press: Oxford, 1998.
- [10] P. Ayotte, R. S. Smith, K. P. Stevenson, Z. Dohnalek, G. A. Kimmel and B. D. Kay, *Journal of Geophysical Research-Planets*, 106, 33387, (2001).
- [11] P. Ayotte, R. S. Smith, K. P. Stevenson, Z. Dohnalek, G. A. Kimmel and B. D. Kay, *Journal of Geophysical Research*, 106, 33837, (2001).
- [12] S. Bahr, A. Borodin, O. Hoff, V. Kempter, A. Allouche, F. Borget and T. Chiavassao, *Journal of Physical Chemistry B*, 110, 8649, (2006).
- [13] A. Bar-Nun, J. Dror, E. Kochavi and D. Laufer, *Physical Review B*, 35, 2427, (1987).
- [14] R. A. Baragiola, In *Water in Confining Geometries*, V. Buch and J. P. Devlin, Eds.; Springer, Berlin, 2003.
- [15] A. Barnun, G. Herman, D. Laufer and M. L. Rappaport, *Icarus*, 63, 317, (1985).

- [16] A. Barnun, J. Dror, E. Kochavi, D. Laufer, D. Kovetz and T. Owen, *Origins of Life and Evolution of the Biosphere*, 16, 220, (1986).
- [17] A. Barnun, J. Dror, E. Kochavi and D. Laufer, *Physical Review B*, 35, 2427, (1987).
- [18] O. Berg and G. E. Ewing, *Surface Science*, 220, 207, (1989).
- [19] B. S. Berland, D. E. Brown, M. A. Tolbert and S. M. George, *Geophysical Research Letters*, 22, 3493, (1995).
- [20] M. P. Bernstein, J. P. Dworkin, S. A. Sandford, G. W. Cooper and L. J. Allamandola, *Nature*, 416, 401, (2002).
- [21] J. E. Bertie, L. D. Calvert and E. Whalley, *Journal of Chemical Physics*, 38, 840, (1963).
- [22] C. F. Bohren and D. R. Huffman, *Absorption and Scattering of Light by Small Particles*, John Wiley & Sons, Inc.: New York, 1998.
- [23] F. Borget, T. Chiavassa, A. Allouche and J. P. Aycard, *Journal of Physical Chemistry B*, 105, 449, (2001).
- [24] V. Buch, L. Delzeit, C. Blackledge and J. P. Devlin, *Journal of Physical Chemistry*, 100, 3732, (1996).
- [25] V. Buch, J. Sadlej, N. Aytemiz-Uras and J. P. Devlin, *Journal of Physical Chemistry A*, 106, 9374, (2002).
- [26] V. Buch and J. P. Devlin, In *Water in Confining Geometries*, V. Buch and J. P. Devlin, Eds.; Springer, Berlin, 2003.
- [27] E. F. Burton and W. F. Oliver, *Proceedings Royal Society*, A153, 166, (1935).
- [28] C. M. Chan, R. Aris and W. H. Weinberg, *Surface Science*, 1, 360, (1978).
- [29] H. Chang, H. H. Richardson and G. E. Ewing, *Journal of Chemical Physics*, 89, 7561, (1988).
- [30] L. Chu and L. T. Chu, *Journal of Physical Chemistry A*, 103, 691, (1999).
- [31] M. P. Collings, J. W. Dever, H. J. Fraser and M. R. S. McCoustra, *Astrophysics and Space Science*, 285, 633, (2003).

- [32] M. P. Collings, M. A. Anderson, R. Chen, J. W. Dever, S. Viti, D. A. Williams and M. R. S. McCoustra, *Monthly Notices of the Royal Astronomical Society*, 354, 1133, (2004).
- [33] P. G. Debenedetti and F. H. Stillinger, *Nature*, 410, 259, (2001).
- [34] J. P. Devlin, *Journal of Physical Chemistry*, 96, 6185, (1992).
- [35] Z. Dohnalek, G. A. Kimmel, R. L. Ciolli, K. P. Stevenson, R. S. Smith and B. D. Kay, *Journal of Chemical Physics*, 112, 5932, (2000).
- [36] J. Dubochet and A. W. McDowell, *Journal of Microscopy-Oxford*, 124, RP3, (1981).
- [37] S. R. Elliot, *Physics of Amorphous Materials*, 2 ed., Longman Scientific and Technical: Essex, 1990.
- [38] G. Faraudo and D. E. Weibel, *Progress in Reaction Kinetics and Mechanism*, 26, 179, (2001).
- [39] D. Ferry, A. Glebov, V. Senz, J. Suzzane, J. P. Toennies and H. Weiss, *Journal of Chemical Physics*, 105, 1697, (1996).
- [40] F. Fleyfel and J. P. Devlin, *Journal of Physical Chemistry*, 95, 3811, (1991).
- [41] V. M. Fokin, E. D. Zanotto, N. S. Yuritsyn and J. W. P. Schmelzer, *Journal of Non-Crystalline Solids*, 352, 2681, (2006).
- [42] K. L. Foster, M. A. Tolbert and S. M. George, *Journal of Physical Chemistry A*, 101, 4979, (1997).
- [43] N. S. Foster, J. E. Amonette, T. Autrey and J. T. Ho, *Sensors and Actuators B-Chemical*, 77, 620, (2001).
- [44] F. Franks, *Polywater*, MIT press: Cambridge, 1981.
- [45] F. Franks, In *Water: A comprehensive treatise*, F. Franks, Ed.; Plenum Press, New York, 1982, Vol. 7.
- [46] G. Frenzer and W. F. Maier, *Annual Review of Materials Research*, 36, 281, (2006).
- [47] J. A. Ghormley, *Journal of Chemical Physics*, 46, 1321, (1967).

- [48] A. Givan, A. Loewenschuss and C. J. Nielson, *Journal of Physical Chemistry B*, *101*, 8696, (1997).
- [49] J. D. Graham and J. T. Roberts, *Journal of Physical Chemistry*, *98*, 5974, (1994).
- [50] J. D. Graham, J. T. Roberts, L. A. Brown and V. Vaida, *Journal of Physical Chemistry*, *100*, 3115, (1996).
- [51] P. Griffiths and J. A. De Haseth, *Fourier Transform Infrared Spectrometry*, John Wiley and Sons, Inc.: New York, 1986.
- [52] A. Hallbrucker, E. Mayer and G. P. Johari, *Journal of Physical Chemistry*, *93*, 4986, (1989).
- [53] Y. P. Handa, O. Mishima and E. Whalley, *Journal of Chemical Physics*, *84*, 2766, (1986).
- [54] S. Haq, J. Harnett and A. Hodgson, *Journal of Physical Chemistry B*, *106*, 3950, (2002).
- [55] S. A. Hawkins: *Fourier transform infrared spectroscopy and temperature programmed desorption of water thin films on the MgO (100) surface*, Ph. D. Thesis, Department of Chemistry, University of Southern California, Los Angeles, 2004.
- [56] S. Hawkins, G. Kumi, S. Malyk, H. Reisler and C. Wittig, *Chemical Physics Letters*, *404*, 19, (2004).
- [57] S. Hawkins, G. Kumi, S. Malyk, H. Reisler and C. Wittig, *Chemical Physics Letters*, *404*, 19, (2005).
- [58] J. Heidberg, B. Redlich and D. Wetter, *Berichte Bunsenges Physical Chemistry*, *99*, 1333, (1995).
- [59] J. Heidberg and B. Redlich, *Surface Science*, *368*, 140, (1996).
- [60] G. Herzberg, *Infrared and Raman Spectra*, Van Nostrand Reinhold Company, Inc: New York, 1945.
- [61] P. V. Hobbs, *Ice Physics*, Claderon Press: Oxford, 1974.
- [62] L. K. Hodgson: *Photodissociation, molecule-surface collision-induced dissociation and direct adsorbate photolysis of nitroso molecules*, Ph. D. Thesis, Department of Chemistry, University of Southern California, Los Angeles, 1993.

- [63] M. J. Hollas, *High Resolution Spectroscopy*, John Wiley & Sons, Inc.: Chichester, 1998.
- [64] A. B. Horn, J. R. Sodeau, T. B. Roddis and N. A. Williams, *Journal of Physical Chemistry A*, *102*, 6107, (1998).
- [65] R. L. Hudson and B. Donn, *Icarus*, *94*, 326, (1991).
- [66] T. Huthwelker, M. Ammann and T. Peter, *Chemical Reviews*, *106*, 1375, (2006).
- [67] J. F. James, *A student's guide to Fourier transforms*, Cambridge University Press: Cambridge, 1998.
- [68] P. Jenniskens and D. F. Blake, *Science*, *265*, 753, (1994).
- [69] P. Jenniskens, S. F. Banham, D. F. Blake and M. R. S. McCoustra, *Journal of Chemical Physics*, *107*, 1232, (1997).
- [70] G. P. Johari, A. Hallbrucker and E. Mayer, *Nature*, *330*, 552, (1987).
- [71] A. M. Jong and J. W. Niemantsverdriet, *Vacuum*, *41*, 232, (1990).
- [72] G. A. Kimmel, K. P. Stevenson, Z. Dohnalek, R. S. Smith and B. D. Kay, *Journal of Chemical Physics*, *114*, 5284, (2001).
- [73] D. A. King, *Surface Science*, *47*, 384, (1975).
- [74] A. Krasnopoler and S. M. George, *Journal of Physical Chemistry B*, *102*, 788, (1998).
- [75] G. J. Kroes and D. C. Clary, *Journal of Physical Chemistry*, *96*, 7079, (1992).
- [76] G. Kumi, S. Malyk, S. Hawkins, H. Reisler and C. Wittig, *Journal of Physical Chemistry A*, *110*, 2097, (2006).
- [77] B. Kusse and E. Westwig, *Mathematical Physics*, John Wiley and Sons, Inc.: New York, 1998.
- [78] D. Laufer, E. Kochavi and A. Barnun, *Physical Review B*, *36*, 9219, (1987).
- [79] F. E. Livingston, J. A. Smith and S. M. George, *Analytical Chemistry*, *72*, 5590, (2000).

- [80] F. E. Livingston and S. M. George, *Journal of Physical Chemistry A*, *105*, 5155, (2001).
- [81] C. Manca and A. Allouche, *Journal of Chemical Physics*, *114*, 4226, (2001).
- [82] C. Manca, C. Martin and P. Roubin, *Chemical Physics Letters*, *364*, 220, (2002).
- [83] C. Manca, C. Martin and P. Roubin, *Chemical Physics*, *300*, 53, (2004).
- [84] C. Manca, C. Martin and P. Roubin, *Chemical Physics*, *300*, 53, (2004).
- [85] Y. A. Mantz, F. M. Geiger, L. T. Molina, M. J. Molina and B. L. Trout, *Chemical Physics Letters*, *348*, 285, (2001).
- [86] C. Martin, C. Manca and P. Roubin, *Surface Science*, *502*, 275, (2002).
- [87] C. Martin, C. Manca and P. Roubin, *Surface Science*, *502-503*, 275, (2002).
- [88] M. Matsumoto, S. Saito and I. Ohmine, *Nature*, *416*, 409–413, (2002).
- [89] E. Mayer and R. Pletzer, *Nature*, *319*, 298, (1986).
- [90] S. M. McClure, E. T. Barlow, M. C. Akin, D. J. Safarik, T. M. Truskett and C. B. Mullins, *Journal of Physical Chemistry B*, *110*, 17987, (2006).
- [91] S. M. McClure, D. J. Safarik, T. M. Truskett and C. B. Mullins, *Journal of Physical Chemistry B*, *110*, 11033, (2006).
- [92] L. Mertz, *Astronomical Journal*, *70*, 685, (1965).
- [93] O. Mishima, L. D. Calvert and E. Whalley, *Nature*, *310*, 393, (1984).
- [94] O. Mishima, L. D. Calvert and E. Whalley, *Nature*, *314*, 76, (1985).
- [95] O. Mishima and H. E. Stanley, *Nature*, *396*, 329, (1998).
- [96] S. Mitlin and K. T. Leung, *Canadian Journal of Chemistry-Revue Canadienne De Chimie*, *82*, 978, (2004).
- [97] A. H. Narten, C. G. Venkatesh and S. A. Rice, *Journal of Chemical Physics*, *64*, 1106, (1976).

- [98] D. Nordlund, H. Ogasawara, P. Wernet, M. Nyberg, M. Odelius, L. G. M. Pettersson and A. Nilsson, *Chemical Physics Letters*, 395, 161, (2004).
- [99] R. H. Norton and R. Beer, *Journal of the Optical Society of America*, 66, 259, (1976).
- [100] G. Natesco and A. Bar-Nun, *Icarus*, 148, 456, (2000).
- [101] M. A. Ovchinnikov and C. A. Wight, *Journal of Chemical Physics*, 99, 3374, (1993).
- [102] M. E. Palumbo, *Journal of Physical Chemistry A*, 101, 4298, (1997).
- [103] M. E. Palumbo, *Journal of Physical Chemistry A*, 101, 4298, (1997).
- [104] R. Pletzer and E. Meyer, *Journal of Chemical Physics*, 90, 5207, (1989).
- [105] P. A. Redhead, *Vacuum*, 12, 203, (1962).
- [106] B. Roland and J. P. Devlin, *Journal of Chemical Physics*, 94, 812, (1991).
- [107] T. L. Roush, *Journal of Geophysical Research-Planets*, 106, 33315, (2001).
- [108] B. Rowland, M. Fisher and J. P. Devlin, *Journal of Chemical Physics*, 95, 1378, (1991).
- [109] B. Rowland and J. P. Devlin, *Journal of Chemical Physics*, 94, 812, (1991).
- [110] J. Sadlej, B. Rowland, J. P. Devlin and V. Buch, *Journal of Chemical Physics*, 102, 4804, (1995).
- [111] S. A. Sandford and L. J. Allamandola, *Icarus*, 76, 201, (1988).
- [112] S. A. Sandford and L. J. Allamandola, *Astrophysical Journal*, 355, 357, (1990).
- [113] S. A. Sandford and L. J. Allamandola, *Journal of Astrophysics*, 355, 357, (1990).
- [114] M. G. Sceats and S. A. Rice, In *Water: A comprehensive treatise*, F. Franks, Ed.; Plenum Press, New York, 1982, Vol. 7.
- [115] J. E. Schaff and J. T. Roberts, *Journal of Physical Chemistry*, 98, 6900, (1994).

- [116] J. E. Schaff and J. T. Roberts, *Journal of Physical Chemistry*, *100*, 14151, (1996).
- [117] J. E. Schaff and J. T. Roberts, *Langmuir*, *14*, 1478, (1998).
- [118] B. Schmitt, J. Ocampo and J. Klinger, *Journal De Physique*, *48*, 519, (1987).
- [119] H. Schober, M. M. Koza, A. Tolle, C. Masciovecchio, F. Sette and F. Fujara, *Physical Review Letters*, *85*, 4100, (2000).
- [120] L. Schriver-Mazzuoli, A. Schriver and A. Hallou, *Journal of Molecular Structure*, *554*, 289, (2000).
- [121] Sheikh, II and P. D. Townsend, *Journal of Physics E-Scientific Instruments*, *6*, 1170, (1973).
- [122] S. C. Silva and J. P. Devlin, *Journal of Chemical Physics*, *98*, 10847, (1994).
- [123] D. A. Skoog and J. L. Leary, *Principles of Instrumental Analysis*, Harcourt Brace College Publishers: Fort Worth, 1992.
- [124] B. C. Smith, *Fourier Transform Infrared Spectroscopy*, CRC Press: Boca Raton, 1996.
- [125] R. S. Smith, C. Huang, E. K. L. Wong and B. D. Kay, *Surface Science*, *367*, L13, (1996).
- [126] R. S. Smith, C. Huang and B. D. Kay, *Journal of Physical Chemistry B*, *101*, 6123, (1997).
- [127] R. S. Smith, C. Huang, E. K. L. Wong and B. D. Kay, *Physical Review Letters*, *79*, 909, (1997).
- [128] R. S. Smith and B. D. Kay, *Surface Review Letters*, *4*, 781, (1997).
- [129] R. S. Smith and B. D. Kay, *Nature*, *398*, 788, (1999).
- [130] R. S. Smith, Z. Dohnalek, G. A. Kimmel, K. P. Stevenson and B. D. Kay, *Chemical Physics*, *258*, 291, (2000).
- [131] G. D. Smith and R. A. Palmer, In *Handbook of Vibrational Spectroscopy*, J. M. Chalmers and P. R. Griffiths, Eds.; John Wiley and Sons, Inc., New York, 2002, Vol. 1.

- [132] R. S. Smith, Z. Dohnalek, G. A. Kimmel, G. Teeter, P. Ayotte, J. L. Daschbach and B. D. Kay, In *Water in Confining Geometries*, V. Buch and J. P. Devlin, Eds.; Springer, Berlin, 2003.
- [133] G. A. Somorjai, *Introduction to Surface Chemistry and Catalysis*, John Wiley and Sons, Inc: New York, 1994.
- [134] C. Spinella, S. Lombardo and F. Priolo, *Journal of Applied Physics*, *84*, 5383, (1998).
- [135] K. P. Stevenson, G. A. Kimmel, Z. Dohnalek, R. S. Smith and B. D. Kay, *Science*, *283*, 1505, (1999).
- [136] F. H. Stillinger, *Science*, *267*, 1935, (1995).
- [137] W. S. Struve, *Fundamentals of Molecular Spectroscopy*, John Wiley and Sons, Inc.: New York, 1989.
- [138] M. M. Suchan: *Molecules-surface interactions in HCl/MgO and Water/MgO Systems*, Ph. D. Thesis, Department of Chemistry, University of Southern California, Los Angeles, 2001.
- [139] M. Svanberg, J. B. C. Pettersson and K. Bolton, *Journal of Physical Chemistry A*, *104*, 5787, (2000).
- [140] T. Takoaka, M. Inamura, S. Yanagimachi, I. Kusunoki and T. Komeda, *Journal of Chemical Physics*, *121*, 1 September 2004, (2004).
- [141] C. A. Tulk, C. J. Benmore, J. Urquidi, D. D. Klug, J. Neufeind, B. Tomberli and P. A. Egelstaff, *Science*, *297*, 1320, (2002).
- [142] J. C. Tully, *Surface Science*, *299/300*, 667, (1994).
- [143] N. Uras, M. Rahman and J. P. Devlin, *Journal of Physical Chemistry B*, *102*, 9375, (1998).
- [144] Z. Y. Wang and S. K. Zhou, *Progress in Chemistry*, *16*, 49, (2004).
- [145] M. Wyart, *Annales De Physique*, *30*, 1, (2005).
- [146] H. Yamada and W. B. Person, *Journal of Chemical Physics*, *41*, 2478, (1964).

[147] J. Yates, J. T., *Experimental Innovations in Surface Science*, AIP Press Springer-Verlag: New York, 1998.

[148] X. J. Yu and H. S. Kwok, *Journal of Applied Physics*, 93, 4407, (2003).

[149] R. Zallen, *The Physics of Amorphous Solids*, John Wiley and Sons, Inc.: New York, 1983.

[150] Y. Zubavichus, M. Zharnikov, Y. J. Yang, O. Fuchs, E. Umbach, C. Heske and M. Grunze, *Langmuir*, 22, 7241, (2006).